Global confinement properties of Tokamak plasmas in global, flux-driven, gyrokinetic simulations

Elisabetta Caschera

Aix*Marseille université
Initiative d'excellence

cea irfm

THÈSE DE DOCTORAT
Université d'Aix-Marseille

École doctorale : Physique et sciences de la matière
Spécialité : **Énergie, Rayonnement et Plasma**

Global confinement properties in global, flux-driven, gyrokinetic simulations

Présentée par :
Elisabetta CASCHERA

Thèse soutenue publiquement le 21 Novembre 2019 devant le jury composé par :

Pascale HENNEQUIN	Rapporteur	Directrice de recherche	CNRS
Laurent VILLARD	Rapporteur	Professeur	EPFL-SPC
Susan LEERINK	Examinateur	Chercheuse	Aalto Univ.
Eric SERRE	Examinateur	Directeur de recherche	CNRS
Eric SONNENDRÜCKER	Examinateur	Professeur	IPP Garching
Guilhem DIF-PRADALIER	Codirecteur de thèse	Chercheur	CEA
Philippe GHENDRIH	Directeur de thèse	Directeur de recherche	CEA

Laboratoire d'accueil :
Institut de Recherche sur la Fusion par confinement Magnétique
CEA, IRFM, F-13108 Saint-Paul-lez-Durance, France
Novembre 2016 - Novembre 2019

Abstract

Understanding and predicting the performance of a fusion reactor in terms of confinement is a major milestone to make fusion energy available. The intrinsic non-linear physics at play makes analytical descriptions challenging: predictions for the design of future reactors such as ITER are thus based on a combination of extrapolations of empirical scaling laws, analytic work and numerical simulations. The latter are gaining a central role in supporting theoretical work and interpretation of experimental data. We investigate here global confinement properties of turbulent heat transport in a Tokamak with first-principles global and flux-driven gyrokinetic simulations with the GYSELA code.

A scaling law for the energy confinement time has been extracted from a database of close to statistical steady-state GYSELA turbulent transport simulations, at constant values of internal energy. A power law scaling has been extracted from scans in three dimensionless parameters: the aspect ratio, the plasma size and the plasma collisionality. We discuss the physics meaning of the resulting exponents, the choice of a power law as basis function for the linear regression analysis as well as the proximity to existing scaling laws in the literature. As a test of robustness, this scaling law has been successfully used to predict new equilibrium states for the GYSELA simulations.

WE have been able to show that boundary conditions could have a significant impact on the confined core plasma. We introduced a toroidally-symmetric penalized heat sink at the radial outer boundary of GYSELA that mimics in shape an actual limiter and a first wall. This heat sink is implemented as an infinite restoring force towards a cold distribution function and allows to reproduce transport properties of the Scrape-Off Layer (SOL) region with adiabatic electrons, including in particular the parallel heat flux to the sink localized by the limiter. We discuss the dynamics of the plasma reorganization in the presence of the limiter and wall. In the SOL, the average radial electric potential is penalized to be proportional to the electron temperature profile, as would be prescribed by zero electric current constraint at the wall. A reversal of radial electric field at the core-SOL interface is generated in GYSELA limiter simulations when the SOL-averaged potential is added by penalizing the quasi-neutrality equation. This effect is sufficient to trigger the formation of a weak transport barrier at the core-SOL interface. This barrier formation appears to be mostly governed by core polarization mechanisms and is observed even when artificially varying the SOL electric potential. Based on the importance of the edge boundary condition to global confinement, we have correlated the quality of confinement with the shape of the flux-surface averaged electrostatic potential. Preliminary results of an automated data-driven analysis appear to support a weak correlation between confinement and the depth of the potential.

The new SOL boundary combined with the plasma drifts leads to rich dynamics and reorganization of heat, particle and momentum fluxes in the SOL and at the core-SOL interface. We discuss poloidal asymmetries of SOL density or the development of a Kelvin Helmholtz-like instability due to an enhanced poloidal velocity shear. The latter appears in the vicinity of the reversed radial electric field at the core-SOL interface. This instability might contribute to the local production of turbulence in the SOL and edge plasma. Finally we report on the complex interplay between core, edge and SOL turbulence in the presence of a limiter and discuss its key role for subcritical turbulence spreading. This latter mechanism is found to be important to recover experimentally-relevant turbulence fluctuations in the pedestal-edge region.

Résumé

La compréhension du confinement du plasma dans les réacteurs à fusion est l'une des étapes importantes pour que l'énergie de fusion devienne une réalité demain. La conception de futurs réacteurs tels qu'ITER est basée sur l'extrapolation de lois d'échelle empiriques. Dans ce travail de thèse nous étudions les propriétés globales du confinement du plasma dans un Tokamak avec l'aide de simulations numériques avancées utilisant le code GYSELA développé au CEA et basées sur une approche dite gyrocinétique globale et forcée par un flux.

Une loi d'échelle pour le temps de confinement de l'énergie a été extraite d'une base de données de simulations du transport turbulent réalisées avec le code GYSELA, et caractérisées par un état d'équilibre statistique, à énergie interne fixée. Une échelle en loi de puissance émerge en fonction de trois paramètres sans dimension : le rapport d'aspect, la taille normalisée du plasma au rayon de Larmor ionique et la collisionnalité du plasma. Une discussion quant à la signification physique des exposants trouvés ainsi que du choix d'une loi de puissance comme fonction de base pour l'analyse de régression linéaire est présentée. Dans ce cadre, une proximité remarquable est trouvée avec les lois d'échelle existantes dans la littérature. Comme test de robustesse, cette loi d'échelle a été utilisée avec succès pour prévoir de nouveaux états d'équilibre pour les calculs.

En parallèle, nous montrons que les conditions aux limites pouvaient avoir un impact significatif sur le plasma contenu dans le noyau confiné. Nous avons introduit un puits thermique, symétrique toroïdalement, en tant que nouvelle condition aux limites par une méthode de pénalisation. Dans le volume du limiteur, asymétrique poloïdalement, et de la paroi, la fonction de distribution subie une force de rappel vers une fonction de distribution froide. Cette technique permet de simuler les propriétés de transport dans la Scrape-Off Layer (SOL), essentiellement bidimensionnelle, avec des électrons adiabatiques. Dans la SOL, le potentiel électrique radial moyen est pénalisé pour être proportionnel au profil de température des électrons, déterminé par les conditions aux limites parallèles de l'interaction plasma-paroi. Un champ électrique radial inversé à l'interface cœur-SOL est alors généré. Cet effet est suffisant pour déclencher la formation d'une barrière de transport faible à l'interface cœur-SOL.

Sur la base de l'importance des conditions aux limites de bord pour le confinement global, nous avons en outre essayé de corréler la qualité du confinement avec la forme radiale du potentiel électrostatique moyenné sur les surfaces de flux. Négatif dans le cœur du plasma, nos résultats préliminaires basés sur une analyse automatique des données indiquent que le confinement s'améliore lorsque le puits potentiel est plus profond, ou inversement.

La région du limiteur combinée aux dérives dans le plasma crée une nouvelle dynamique à l'interface cœur-SOL, cruciale pour le confinement magnétique, caractérisée par des réorganisations du flux de chaleur, de particules et de quantité de mouvement dans cette région. Nous discutons l'importance des asymétries poloïdales de la densité de SOL ainsi que du développement d'une instabilité de type Kelvin Helmholtz proche de la séparatrice due à un cisaillement de vitesse poloïdal accru en partie lié à l'inversion du champ électrique radial à l'interface cœur-SOL. Cette dernière peut contribuer à la production locale de fluctuations de turbulence dans la SOL ainsi que dans le plasma de bord. Nous rapportons également l'interaction complexe entre les turbulences de cœur, de bord et de SOL en présence d'un limiteur et discutons de son rôle clé dans la propagation

spatiale sous-critique de la turbulence. Ce dernier mécanisme s'avère important pour être capable de décrire par le calcul les niveaux expérimentaux de fluctuations de turbulence dans les régions du piédestal et du bord du plasma.

Acknowledgments

First of all I would like to thank all the jury members for accepting to read my manuscript: the referees Pascale Hennequin and Laurent Villard, then Susan Leerink, Eric Sonnendrücker and Eric Serre. I have really appreciated your comments and questions at the moment of the defense, I thank your all for making me feel at ease.

My thesis work has been directed by the excellent and dynamic duo of Philippe Ghendrih and Guilhem Dif-Pradalier. During these three years I had the chance, and the honor, to work side by side with both of them meeting their original way of thinking. Thank you for your patience in teaching me all I know in plasma turbulence, and for your unfailing support during the key moments of the PhD.

If I had to summarize my thesis in one sentence I would say that I let GYSELA speak. This has been possible also thanks to the kind availability of the GYSELA team. I sincerely thank Virginie Grandgirard, Guillaume Latu, Chantal Passeron for helping me taking care of all the hitch while compiling, running, repatriating and analyzing. My thanks to Xavier Garbet and Yanick Sarazin for your precious comments and suggestions, for the 'bonjour' moments in the morning and for the chocolate at 5pm. The greatness of the code reflects the goodness of the team (and vice-versa).

The IRFM institut is place of inspiring scientific discussions, I would like to thank Laure Vermare and Patrick Tamain for they interest in my work and for enriching it by making me think from the different experimental and fluid prospectives. I thank all the Groupe Theorie and Simulations, lead by Remi Dumont, for the nice and chatting work environment they have established. Moreover I thank the IRFM institute for allowing me to present my work in many conferences during these years.

All the students I have met during my PhD years have left me a good memory, I will here name the closest. Of the formers: Claudia Norscini, I had way to understand that my PhD existed thanks to her intuition, Peter Donnel, who crucially, patiently and constantly helped me in learning both french and physics. With Anastasia I have shared her office, enjoying all the girly chats and tea moments. It was a real pleasure to share in all the instants my PhD time with Guillaume, without a doubt I would do it again. Thanks to Serafina, who is accompanying my steps since a long time, and to Myriam, her elegance and determination are of example to all women in plasma physics. I thank Raffaele for sharing with me his scientific doubts, the youngest Camille, Julio, Samuele, Mathieu, Elias, Manuel, Robin and all the others: good luck guys! I would also thank Jorge, Didier and Laurent for the rock'n'roll evenings.

My thanks also goes to the large Italian community in the institute, whose natural role is to welcome and support. Grazie a Gloria, Gerardo, Maurizio, Guido, Alberto, Davide, Giorgio, Giacomo, Giacomo, Valeria, and last but not least Virginia, and all the others.

During these years in France I had the chance to live for a little while in Marseille, where I have left a piece of my heart. In exchange I will always bring with me the sincere

friendship of Marianna, Juan & A. and Eunok, who formed my multicultural Marseilles family. Thank you!

For sure, I would not be the person I am and I would not have achieved this PhD without the support of my family of origin. Thank to mamma Cristina, papà Giovanni, Daniele & Sara, Francesca and the young Irene, for all your encouragements during the endless video-chats. Vi voglio tanto bene.

Finally, I thank Alejandro for living every day by my side.

Contents

Introduction

In order to achieve favorable conditions for nuclear fusion reactions, the matter needs to reaches very high temperatures, hotter than the sun, and consequently to be in the plasma state. The presence of very high gradients between the core of the plasma and the external environment makes the plasma an unstable system, prone to turbulence. The confinement of such high energy densities is one of the major technological challenges of the last century. Understanding and predicting plasma magnetic confinement is to date one of the missing steps to ease making fusion energy available on earth.

In the plasma, the motion of charged particles interacts with the electromagnetic field and the evolution of the system is essentially non-linear. The collective behavior of the plasma can generate forms of non-local transport, which can influence the plasma confinement. In this framework, numerical simulations provide a fundamental support to the analytical work and to the interpretation of experimental measurements.

The Tokamak configuration is used to confine and heat the plasma up to fusion condition. The plasma is confined by means of a strong magnetic field enclosed in a toroidal volume. At the plasma periphery, namely the Scrape-Off Layer, the magnetic field lines impact the solid wall and the plasma-wall interaction influences the transport regime. Conversely in the plasma bulk the magnetic field lines close within the plasma volume, preventing any contact between the hot plasma and the wall. The two regions are fundamentally different regarding the transport properties and are usually modeled separately.

This dissertation presents a study of the properties of plasma magnetic confinement in the Tokamak configuration. The work is based on the analysis and interpretation of global gyrokinetic numerical simulations of the plasma evolution. We focus on two main aspects: on the one hand, the scaling of confinement properties with the plasma parameters, on the other hand, the effect of the plasma periphery on transport properties. In Chapter 1 are presented the basic concepts of magnetic confinement, the state of the art open issues and the motivations behind this work. Chapter 2 is focused on the analysis of the numerical tool that have been used. In Chapter 3 we analyze the scaling properties of plasma confinement: the numerical simulations allow us recovering a scaling law of the energy confinement time for the plasma system as well as a comparison between global and local scaling properties. Chapter 4 is dedicated to describing the implementation of a new boundary condition which mimics the physics of the plasma periphery in the numerical tool. In Chapter 5, the development of a global structure in the electric potential is presented, comparing plasma core and periphery. In Chapter 6 is described the effect of the new more realistic boundary on the equilibrium plasma by the analysis of the simulation results. Finally, Chapter 7 is dedicated to describing the interplay of turbulent transport at the interface between the two regions of core and periphery. In Chapter 8 conclusions of the study are drawn.

Chapter 1

Open issues for fusion energy

1.1 The magnetic confinement and the Tokamak

The concept of magnetic confinement uses a strong magnetic field to confine the plasma. It takes advantage of the Lorentz force between the charge particles and the magnetic field, such that the particles are caught in a circular motion around the magnetic field lines.

1.1.1 Charged particles and the electromagnetic field

Single particle motion in a magnetic field

The motion of a single non relativistic particle immersed in a magnetic field $\mathbf{B}$, when neglecting other forces, is described by the Newton's law

$$m\dot{\mathbf{v}} = q\mathbf{v} \times \mathbf{B} \tag{1.1}$$

where m, q are the particle mass and charge and $\mathbf{v}, \dot{\mathbf{v}}$ the particle velocity and acceleration. One can distinguish two symmetries for the particle motion: $m\dot{\mathbf{v}} \cdot \mathbf{b} = 0$ in the direction *parallel* $\parallel$ to the magnetic field $\mathbf{b} = \mathbf{B}/B$, the motion is free from the magnetic force $q\mathbf{v} \times \mathbf{B}$, and the symmetry $m\mathbf{v} \cdot \dot{\mathbf{v}} = 0$ that leads to the property that the Lorentz force produces no work. The kinetic energy $mv^2/2$ is consequently constant and so is the parallel motion. The induced perpendicular motion is therefore a circular motion around the magnetic field line, i.e. the *gyro-motion* or *Larmor motion*. Characteristics of this perpendicular motion are the *Larmor frequency* $\Omega = qB/m$ and the *Larmor radius* $\rho = \Omega^{-1}v_\perp$. The center of the circular trajectory is called *guiding center*.

For a hydrogen plasma at thermal energy $T \sim 10KeV$ we can consider $v_\perp \sim v_{th} = 10^6 m/s$ (v_{th} is the thermal velocity of the particles $mv_{th}^2/2 = T/2$). This velocity is way higher than ordinary velocities in mechanical systems, although it remains lower than the speed of light, so that relativistic effects can be neglected. It corresponds to a Larmor frequency $\Omega \sim 10^8 s^{-1}$ and radius $\rho \sim 10^{-2}m$.[1]

[1]The quantities derived here are relative to the Hydrogen ions ($m_i = 1.6 \cdot 10^{-27}Kg, q_i = 1.6 \cdot 10^{-19}C$) in a magnetic field of typically $B = 1T$

Electromagnetic drifts

In presence of a force which acts constantly in a direction perpendicular to the magnetic field during its gyro-motion, the particle is alternately accelerated, when the velocity is aligned to the force, and decelerated, when the particle velocity and the force are in opposite directions. This leads to a periodic modification of the Larmor radius so that after one turn, the circular orbit does not reconnect onto itself. The guiding center hence shifts along the third direction, both perpendicular to the magnetic field and to the force.

Of particular interest is the resulting drift velocity in presence of a perpendicular electric field. The electric drift velocity is defined as

$$v_{E\times B} = \frac{E \times B}{B^2} \tag{1.2}$$

It does not depend on the nature of the particles and therefore acts on the whole plasma. Besides, if the electric field exhibits some particular symmetries, the $E \times B$ velocity gives rise to long range flows in the plasma.

Regarding the plasma confinement, a relevant role is taken also by the ∇B-drift. In a simple system where only the magnetic field acts and the magnetic field varies spatially, the length of the Larmor radius is as well modified during the gyro-motion. The resulting drift velocity

$$v_{\nabla B} = \frac{K_\perp}{qB}\frac{B \times \nabla B}{B^2} \tag{1.3}$$

depends on the particle charge. Particles of opposite charge drift in opposite directions, creating charge separation in the system. Also, the drift velocity is directly proportional to the perpendicular kinetic energy $K_\perp$, making particles at higher energy drifting faster.

The plasma: collective behavior

The plasma is a thermal ensemble of positive *(ions)*, and negative *(electrons)* charged particles. In general, the kinetic energy T of each particle is much higher than the potential energy between the particle and its closest neighbor. The motion of each particle interacts with the surrounding electromagnetic field. However, from a macroscopic point of view, the plasma system can be considered electrically neutral. The charged particles organize their motion in such a way to screen each other's electrostatic potential. The distance at which the electrostatic potential of a test particle due to its nearest neighbor balances its kinetic energy is called Debye length $\lambda_D = \frac{e^2}{4\pi\epsilon_0 T}$. At a distance of a Debye length from the test particle, its electrostatic potential decreases in magnitude of $1/e$, e being the Napier's constant. For a plasma at $T = 10KeV$ the Debye length is of the order of $10^{-4}m$, smaller than the typical ion Larmor radius by two orders of magnitude. At spatial scales larger than the Debye length the plasma is considered *quasi-neutral*.

For a plasma at the typical temperature of $T = 10KeV$, the distance of closest approach between two charges (Landau scale) $\lambda_L = q^2/4\pi\epsilon_0 T < 10^{-9}m$ is much smaller than the mean distance between two particles (Loschmidt scale) $\lambda_l = \sqrt[3]{n} > 10^{-7}m$. The probability of two particles to undergo a collision event is very low. The low collisionality characterizing plasmas makes difficult, or in some cases inappropriate, the definition of a thermodynamical equilibrium for the system.

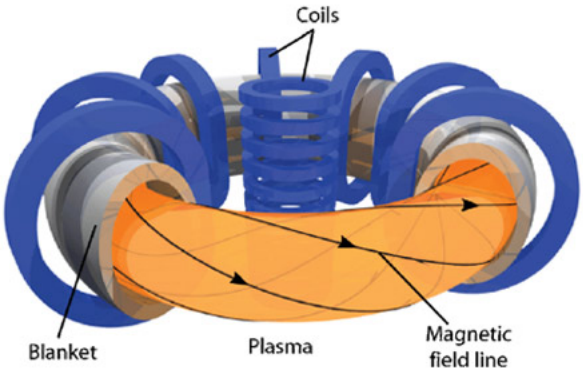

Figure 1.1: Schematic view of the Tokamak magnetic configuration

1.1.2 Toroidal flux surfaces and helical field lines: the Tokamak

By catching the particles in the gyro-orbit, the Lorentz force bounds their perpendicular motion. The simplest approach to confine also the parallel free streaming is to close the magnetic field line in a ring. In the Tokamak configuration, the plasma is confined in a toroidal volume. A strong toroidal magnetic field, generated by a series of poloidal coils, governs the confinement of the charged particles along the toroidal direction. However, according to the ampere equation $2\pi R B_T = \mu_0 I_p$ [2] the toroidal magnetic field B_T inversely depends on the distance from the central symmetry axis R and therefore it is not uniform. The drift velocity generated by the radial variation of B is vertical and can reach values of the order of $10^3 m/s$. A plasma volume of $10m$ typical size would disappear in $10^{-2}s$. A toroidal magnetic field is not sufficient to ensure particle confinement. In a Tokamak, the plasma drift governed by the vertical motion is prevented by adding a poloidal magnetic field. A toroidal current generating the poloidal field is induced in the plasma by means of a central solenoid. The resulting field lines are of helical shape and generate nested toroidal flux surfaces. A schematic view of this machine is shown in figure 1.1.

One can already define some dimensionless parameters characteristic of this configuration:

- The aspect ratio A is a purely geometric parameter. By definition is the ratio between the major R_0 and minor a radius[3] of the torus $A = R_0/a$ and it is > 1. From an engineering point of view, a less compact machine with high aspect ratio provides wider room to the central solenoid and it is easier to design. The influence of this parameter on the transport regime and on plasma confinement is very difficult to investigate experimentally, since changing the aspect ratio means building a different machine. ITER will have an aspect ratio of $A = 3.2$ at maximum. A machine with bigger aspect ratio is WEST, $A = 6$.

- The parameter $\rho_* = \rho_i/a$ is the ion Larmor radius normalized to the plasma characteristic length. Its inverse a/ρ_i is a measure of the number of radial steps necessary for a particle to escape the system and gives a rough mere initial idea of the confinement level. It is indeed expected to be the main parameter determining the energy

[2] Here I_p is the current flowing in the poloidal coils and μ_0 the vacuum magnetic permittivity

[3] The major radius R_0 is defined as the distance between the symmetry axis of the torus and the center of the poloidal section, the minor radius a is the radius of the poloidal section

confinement time [1]. Reducing the plasma size parameter would lead to a better confinement. A smaller ρ_* can be achieved either by increasing the magnetic field amplitude or by increasing the machine size. Expected values in ITER are of the order of 10^{-3}.

- The plasma collisionality $\nu_* = L_\parallel / L_{coll}$ is a measure of the collisionality level in the plasma. It is defined as the ratio between the parallel connection length $L_\parallel$, i.e. the length to travel of π degrees in the poloidal direction along the helical magnetic field line, and the typical mean free path between two collisions $L_{coll} = Log\Lambda / n\lambda_L^2$ where $\Lambda = \lambda_D / \lambda_l$ is called *plasma parameter*. The collisionality depends inversely on the plasma density and temperature $\nu_* \propto 1/nT^2$, hence increases with the radial direction.

- The safety factor q is a measure of the average pitch angle of the magnetic field lines on the flux surfaces. Basically, it represents the number of toroidal revolution performed for one poloidal revolution by the field lines. In the Tokamak $q > 1$ and it increases with the radial direction.

1.1.3 Open and closed field lines regions

The goal of a thermonuclear fusion reactor is to extract energy from the burning plasma. Accordingly, a burning plasma is an open system where energy is produced in the very core, transported all across the plasma volume and released at the plasma edge. In steady state conditions, the energy extraction from the system is both useful and essential for the correct operation of a fusion machine: a completely insulated burning plasma would increase its internal energy content up to possibly explode. The definition of the best way to organize the energy extraction at the plasma boundary is still an argument of scientific discussion in the fusion community. Two main configurations are available for Tokamaks: in the *limiter configuration* a solid object protrudes from the wall chamber into the plasma, intercepting the external concentric flux surfaces. In the *divertor configuration* the magnetic field is shaped to create a $X - point$, where the poloidal field is null. In both cases, two regions with significant different physics at place can be identified:

- the *confined* region, where the magnetic field lines are completely immersed into the plasma. Here the transport outward the system is directed radially. This region is limited by the so called Last Close Flux Surface, or simply *separatrix*.

- the *Scrape-Off Layer (SOL)*, where the magnetic field lines hit the solid matter. There the particles moving along the field line impact on the solid matter, which acts as a real plasma sink. In the SOL, the particle and the heat transport are essentially directed both in the parallel and perpendicular to the magnetic field lines directions. Also, density and temperature are much lower in the SOL with respect to the core, which makes the collisionality significantly higher.

Historically, the two regions have been studied separately. The increased collisionality in the SOL allows for the use of fluid approaches in this region, resulting in a remarkable reduction of the computational resources involved. Conversely the extremely low collisional core region leads to consider kinetic descriptions more appropriates, which are much more complex to handle numerically.

1.2 The big issue: how to predict and improve plasma confinement?

In a laboratory burning plasma, part of the energy that heats the system comes from the alpha particles produced in the fusion reaction P_α, although an auxiliary heating device P_{add} is required to sustain the high temperatures. This enormous thermal energy needs to stay confined inside the plasma volume typically as long as the time between two fusion reactions. The energy confinement time τ_E is defined as the ratio between the internal energy content and the power loss by the system $\tau_E = W/P_{loss}$. This parameter can be considered as a measure of the quality of confinement. The value of τ_E depends on the transport regime in the system and characterizes the balance between sources and outward fluxes. An accurate prediction of the transport in a Tokamak is to date a missing milestone for the success of fusion energy.

A pillar in plasma transport modeling is the Neoclassical theory [2], where transport coefficients are analytically derived within the assumption of solely collisional axisymmetric transport in a spatially non-uniform magnetic field. One can therefore derive the thermal and particle diffusion coefficients resulting from the effects of collisions on the particle trajectories. However, the transport measured in experiments exceeds the neoclassical predictions of at least one order of magnitude [3].

It is commonly recognized that the further and most important channel for heat loss is plasma turbulence. The extreme conditions of the plasma system make it out of thermodynamic equilibrium. The high gradients of density and temperature drive turbulent transport, which release the plasma energy. Experimental observations have characterized the turbulence features: the eddies are generally elongated on the field line such that the parallel wavelength is much smaller than the perpendicular one. Also, the relative amplitude of the fluctuations is rather small, varying between 1% and 10% and increasing with the radius. The system is shown to stabilize on profiles close to marginal stability, on top of which the turbulent fluctuations transport the energy. The turbulent regime displays characteristics akin to the Self-Organized Criticality (SOC) [4, 5], for which intermittent transport events, namely *avalanches*, release outwards a significant quantity of heat flux. In magnetized plasmas, the avalanches size is normally much larger than the Larmor radius and in some cases can be comparable to the plasma size. In such a regime, a local description of the transport may loose its validity.

A rich dynamics of interplay between large scale and small scales is characteristic of the plasma turbulence. The nonlinear interaction of turbulent modes is shown to transfer energy from small scales to large scales, generating *Zonal flows* of global extension in one direction [6]. Transport in the SOL is observed to be dominated more by avalanches events [7]. Conversely in the confined region avalanches and zonal flows strictly interact, possibly leading to the formation of transport barriers, local regions in which transport is reduced. A process of continuous formation and relaxation of the barriers governs the core transport [6, 8, 9].

Of major interest regarding confinement in Tokamaks, is the formation of a transport barrier at the interface between the confined and open field lines regions. There the presence of a barrier would reduce the outward flux right before being evacuated in the SOL. In such conditions the energy content in the confined region can increase and so do the confinement performance. A transition between Low confinement *(L-mode)* and High confinement regimes *(H-mode)* is observed experimentally as a threshold phenomenon on

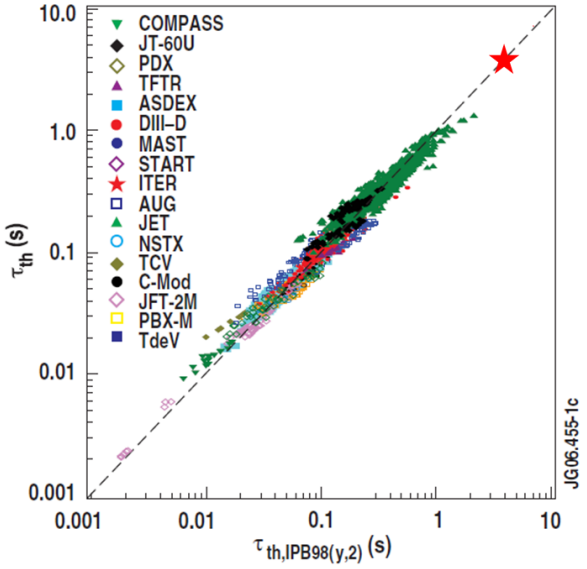

Figure 1.2: Plot of the experimentally measured energy confinement time (vertical axis) versus that predicted by the scaling law (horizontal axis). Figure taken from [11].

the external power source [10]. However, the mechanism triggering this transition is not yet fully understood. In general, a comprehensive description of turbulent transport is not yet achieved and the current predictions on confinement performance of future reactors could reveal debatable.

A strong experimental effort has been performed in the past years to relate the energy confinement time τ_E to the main plasma parameters. A scaling law has been build collecting the data of existent machines with similar geometry (Figure 1.2). By fitting the points with a power law, several scaling laws have been derived on the base of different transport regimes. We report here the H-mode energy confinement scaling currently used for standard operations. It is expressed in terms of dimensionless parameters[4] as [11]:

$$\Omega_i \tau_{th,IPB98(y,2)} \sim \rho_*^{-2.69} \beta^{-0.9} \nu_*^{0.08} M^{0.96} q^{-3.0} \epsilon^{0.73} \kappa^{3.29} R^{-0.01} \tag{1.4}$$

where β is the ratio between the plasma pressure and the magnetic pressure, M the mass ratio between plasma ions and the proton, $\epsilon = 1/A$ the inverse of the aspect ratio, κ the plasma elongation, namely the ratio between the plasma height and the plasma width (in the case the cross section of the flux surfaces is not circular). The design of the experiment ITER relies upon the extrapolation of this scaling law. Ensuring that a fusion reactor will follow such scaling properties with sufficient precision (as in aerodynamics) is a major challenge of the fusion community.

[4]It to be noted that in equation (1.4) all parameters are dimensionless but for R, the latter exemplifies the uncertainty on the various exponents since a perfect scaling law would ensure tht the exponent of R is 0.

1.3 Context of this thesis

In perspective of understanding, describing and predicting plasma transport, numerical simulations support both for the analytical derivations of transport models and the interpretation of the experimental measurements. However, the computational power necessary to simulate the plasma evolution on the complete range of spatial and temporal scales involved is not yet available. Several modeling choices should be made, of which the impact on the resulting plasma evolution is often unclear. For example, one could suppose a scale separation between the equilibrium plasma and the fluctuations and evolve only the fluctuating part of plasma profiles to study the turbulence. Else assuming a local behavior of the transport one can limit the geometrical domain in the vicinity of a field line and fix the profiles gradients. Such restrictions do not allow for (i) the back-reaction of the equilibrium plasma on turbulence and therefore (ii) variations of the plasma profiles on a global scale. A more accurate description of the plasma would involve a heat source, which builds the plasma profiles and let turbulence evolve self-consistently over the entire plasma volume. All comes with a prize: the computational cost of such simulations significantly increases so that to simulate the plasma evolution on several confinement times is still out of reach. Nevertheless, there are cases in which the two approaches give different results[12]. Turbulent transport has been shown to display hints of non-locality both in theory [13] and, more recently, in experiments as well [14]. A complete understanding of the impact of non-local transport on plasma confinement is still missing, as well as a rigorous comparison between local and global modeling.

This thesis aims to clarify some global properties of transport in Tokamak plasmas. We address the problem using first-principles gyrokinetic simulations in full toroidal geometry (Chapter 2). In particular, we allow for the self-organization of turbulent transport by the use of a heat source and the profiles are free to evolve. No separation between equilibrium and fluctuations scales has been made. We carry out the research on two different aspects:

The energy confinement time scaling: we build the first multi-parameter energy confinement time scaling based on global gyrokinetic simulations. We take advantage of close to steady state initial conditions to reduce the computing time. The simulations allow also the comparison between the global scaling of the confinement time and the local properties of turbulence. (Chapter 3)

The effect of realistic boundary conditions: we modify the radial outer boundary condition of the code to mimic the Scrape-Off Layer (Chapter 4). We show evidences of coupling between the confined and open field line regions in terms of the plasma polarization, or alternatively the radial electric field (Chapter 5). We analyze the impact of the SOL boundary on the equilibrium plasma (Chapter 6). We show that the SOL boundary affects the development of turbulence in the plasma edge and uncover additional turbulence mechanisms such as a possible Kelvin-Helmholtz instability (Chapter 7).

Chapter 2

GYSELA global and flux-driven gyrokinetic simulations

The derivation of analytical models describing the plasma evolution is often based on the assumption of scale separation between the different phenomena at place. However, the turbulent transport is a multi-scale process, involving several spatial and time scales from the Larmor motion to the global evolution of the plasma profiles. In this view, numerical simulations take a central role in supporting both theoretical analysis and the interpretation of experimental data as well as improving the understanding of turbulent transport.

In this chapter we describe the characteristics of the numerical simulation performed in this thesis with the GYSELA code. A peculiarity of this code is that it evolves the plasma over a wide range of spatial and time scales, from the ion Larmor motion to the profile evolution. Such a purpose is expensive in terms of computational resources and requires massive parallelization techniques. Similar models are found in the codes GT5D[15], ELMFIRE[16], ORB5[17], XGC1[18], which differ mostly for the numerical scheme implemented. A review on gyrokinetic simulations can be found in [19].

2.1 The interchange instability

A key mechanism underlying plasma micro-turbulence in magnetically confined plasmas is the so-called *interchange* instability. In some conditions, it is energetically favorable for two flux tubes at different pressure to exchange their place[20], which leads to an unstable process. This mechanisms is similar to the Rayleigh-Bénard instability developing in neutral fluids: the simplest picture is the one of a water layer heated from the bottom, see Figure 2.1. A temperature gradient develops in the same direction as the gravity field. When the heating flux overcome a certain threshold, the conductivity of the fluid is not sufficient to redistribute the heat towards the cold boundary and convective cells form to transport the hot fluid elements to the top colder region and vice-versa.

In the same way when the pressure gradient is directed as the gradient of the magnetic field amplitude in the plasma, convective cells are formed that release thermal energy in the outer regions. This happens in the low field side region, the external part of the torus with respect to its symmetry axis (Figure 2.1). A damping mechanism is identified in the parallel motion along the helical magnetic field, which inhibits charge separation in the system. The instability appears above a threshold in pressure gradient. As will be

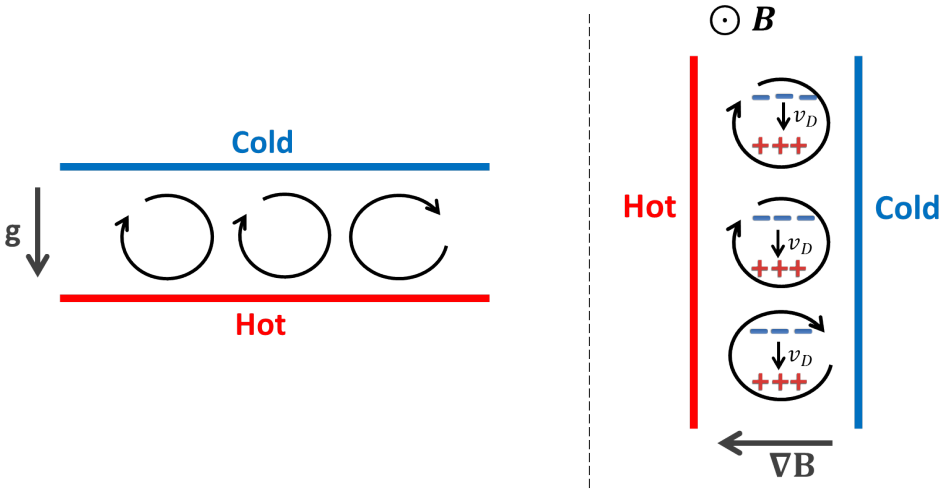

Figure 2.1: Analogy between the Rayleigh-Bénard instability (*left*) and the interchange (*right*).

described in the next section, a complete analytical expression of the threshold is not so easy to determine. Well above the threshold, the instability growth rate γ for a stratified fluid immersed in an effective gravity field g scales like:

$$\gamma \propto \sqrt{\frac{g}{L_p}} \tag{2.1a}$$

where L_p is the gradient length of the pressure stratification. The smaller the characteristic gradient length the larger the growth rate increases. Taking into account the typical normalization backing the calculation of expression 2.1a, hence frequencies by the ion Larmor frequency Ω_i, lengths by the ion Larmor radius ρ_i with $g = \rho_i/R$, one then obtains:

$$\gamma \approx \tau_{\parallel}^{-1} \sqrt{\frac{R}{L_p}} \tag{2.1b}$$

where $\tau_{\parallel} = v/R$ is a typical time for parallel transport, v being the free streaming ion velocity, typically the ion thermal velocity and parallel distances scaling like the major radius R.

2.2 Modeling plasma micro turbulence in the gyrokinetic framework

Transport in magnetized plasmas involves phenomena taking place on a large range of spatial and time scales: from the Debye length -or even less- to the system size over which the fields extend, from the fastest electron frequency to the characteristic time of the internal energy evolution, that is the energy confinement time. The essential interplay between particles and electromagnetic fields makes the system strongly nonlinear. In this Section, after describing the standard plasma modeling approaches, we analyze the gyrokinetic framework used in GYSELA.

2.2.1 Plasma modeling approaches

In the most naive approach to describe the evolution of the plasma one should retain the trajectory of each particle, coupled to the evolution of the electromagnetic fields. However, for a plasma of $\sim 10^{20}$ particles per cubic meter such brute force approach is not only out of reach but also meaningless in terms of physics. Indeed, not measurements can be confronted to this level of details, and, more fundamentally, the aim of physics is to provide the simplest and most efficient description of observations. More advanced modeling is therefore mandatory.

An alternative and widely used approach consists in a statistical description of the population of particles of the same species s using a distribution function $f_s(\mathbf{x}, \mathbf{v}, t)$ in the 6 dimensional phase space -3 dimensions for position $\mathbf{x}$ and 3 dimensions for velocity space $\mathbf{v}$). $f_s \mathrm{d}\mathbf{x}\mathrm{d}\mathbf{v}$ then stands for the number of particles in the phase space volume $\mathrm{d}\mathbf{x}\mathrm{d}\mathbf{v}$ at a given time. The distribution function f_s is defined for each species in the plasma, namely the various ions species with positive charge and the electrons of negative charge. The evolution equation for f_s is the Boltzmann equation, which in the case of purely collisionless plasma is called *Vlasov* equation and reads:

$$\frac{Df_s}{Dt} = 0 \tag{2.2}$$

where D/Dt is the total time derivative in phase space. Let $X = (\boldsymbol{x}, \boldsymbol{v})$ be the phase space coordinate, $\boldsymbol{x}$ being the position in 3D space and $\boldsymbol{v}$ the velocity also in 3D. The use of the velocity is suitable for classical, hence non-relativistic, particles.The particle trajectories when only governed by the Lorentz force, hence electromagnetic fields, can be expressed in the Hamiltonian formalism according to the Hamiltonian H and the phase space motion equations for the conjugate variables $\boldsymbol{x}$ and $\boldsymbol{p} = m\boldsymbol{v}$:

$$\dot{\boldsymbol{x}} = \frac{1}{m}\frac{\boldsymbol{\partial}}{\partial \boldsymbol{v}} H = \Big[H, \boldsymbol{x}\Big]_{p,x} \tag{2.3a}$$

$$\dot{\boldsymbol{v}} = -\frac{1}{m}\frac{\boldsymbol{\partial}}{\partial \boldsymbol{x}} H = \Big[H, \boldsymbol{v}\Big]_{p,x} \tag{2.3b}$$

and therefore:

$$\dot{X} = \Big[H, X\Big]_{p,x} \tag{2.3c}$$

We have introduced here the Poisson brackets $\big[f, g\big]_{x,p}$ defined by:

$$\Big[f, g\Big]_{p,x} = \frac{\boldsymbol{\partial} f}{\partial \boldsymbol{p}} \frac{\boldsymbol{\partial} g}{\partial \boldsymbol{x}} - \frac{\boldsymbol{\partial} f}{\partial \boldsymbol{x}} \frac{\boldsymbol{\partial} g}{\partial \boldsymbol{p}} \tag{2.4}$$

In such a framework one can then write:

$$\frac{Df_s(X,t)}{Dt} = \frac{\partial f_s}{\partial t} + \dot{X}\frac{\partial}{\partial X} f_s = \frac{\partial f_s}{\partial t} + \Big[H, X\Big]_{p,x} \frac{\partial}{\partial X} f_s = 0 \tag{2.5a}$$

This yields the Hamiltonian form of the phase space conservation expression of the distribution function f_s:

$$\frac{\partial f_s}{\partial t} + \Big[H, f_s\Big]_{p,x} = 0 \tag{2.5b}$$

This equation expresses that particles are neither created nor destroyed. The evolution equations for each species s are coupled to Maxwell equations to self-consistently compute the electromagnetic field. The resulting system of equations is closed and includes phenomena over a wide range of spatial and time scales. The numerical resolution of the complete $6D$ system is quite challenging. The gyrokinetic framework described in the next Section represents an alternative to the $6D$ kinetic model, since the reduction to 5 dimensions allows for numerical simulations on time scales relevant for plasma confinement.

A further reduction of the model is performed when projecting the distribution function on the position space $(\mathbf{x}, t)$, removing the dependency on velocity coordinate. One can define quantities such as the density n_s, particle flux $\mathbf{\Gamma}_s$, total pressure tensor $\mathbf{\Pi}_s$ and the energy flux $\mathbf{Q}_s$ as the moments of the distribution function with respect to a polynomial base of velocity functions:

$$n_s = \int f_s d\mathbf{v} \quad ; \quad \mathbf{\Gamma}_s = \int f_s \mathbf{v} d\mathbf{v}$$
$$\mathbf{\Pi}_s = \int f_s (\mathbf{v} \otimes \mathbf{v}) d\mathbf{v} \quad ; \quad \mathbf{Q}_s = \int f_s \left(\frac{m|\mathbf{v}|^2}{2} \mathbf{v} \right) d\mathbf{v}$$

These moments undergo a hierarchy of equations, the *fluid* equations. The complete information on the evolution of the system in the velocity space is retained when considering an infinite number of moments. The relevance of the fluid model stands in the truncation process. Defining the appropriate level of truncation for the magnetized plasma and quantifying the importance of phenomena in the velocity space, such as plasma-wave interaction, for the evolution of the system is still a matter of active research. In practice, high collisionality regimes favor the achievement of Boltzmann equilibrium in velocity space, mitigating the kinetic effects. However this limit, usually called the fluid limit is not readily fulfilled in conditions of high thermal energy and low density and definitely not in the plasma core region.

2.2.2 The gyrokinetic reduction

The gyrokinetic theory has been developed as a reduced model, with respect to the fully kinetic model, for strongly magnetized plasmas. The latter are characterized by a strong anisotropy between perpendicular and parallel directions with respect to the magnetic field, hence free parallel motion at typically the thermal velocity and slow perpendicular drifts as well as high Larmor gyration frequency compared to the longer transport time scales. The main idea behind the gyrokinetic reduction is to eliminate the fastest time scales of the particle cyclotron motion. This can be achieved by averaging as well as more advanced scale separation. The resulting system is then reduced to 4 dimensions and one motion invariant. The standard reference on the gyrokinetic framework is the Brizard-Hahm derivation [21]. We describe hereafter the main features of the theory.

The gyrokinetic framework is derived on the basis of an expansion according to a small parameter that characterizes the strength of the magnetic field. For convenience, the usual approach assumes a single ordering parameter such that:

$$\frac{\omega}{\Omega_i} \sim \frac{k_\parallel}{k_\perp} \sim \frac{\delta n_i}{n_0} \sim \frac{\delta B}{B_0} \sim \frac{\rho_i}{L} \ll 1 \tag{2.6}$$

The subscript i stands for the main ion species in the plasma. The typical fluctuation frequency ω is much smaller than the gyro-frequency Ω_i, the parallel wavelength $k_\parallel$ much smaller than the perpendicular one $k_\perp$, the density fluctuations δn_i are much smaller than the mean density profile n_0, the fluctuations of the magnetic field δB are much smaller than the mean field B_0 and the Larmor radius ρ_i much smaller than the typical gradient length L. Experimental observations are shown to support this ordering in particular regarding micro-turbulence in the core plasma.

The gyrokinetic equation is derived from the Vlasov equation 2.2 in the $6D$ phase space $(\mathbf{x}, \mathbf{v})$. The change of coordinates from particle phase space to guiding-center phase space where the three dimensional vector $\mathbf{x}_{gc} = \mathbf{x} - \boldsymbol{\rho}$ represents the guiding-center position. This new position depends on space $\mathbf{x}$ and transverse velocity through the Larmor radius $\boldsymbol{\rho}$. In velocity cylindrical coordinate one can then split the velocity into a component parallel to the magnetic field and a perpendicular component, typically the magnetic moment $\mu = mv_\perp^2/2B$ and α is the gyration angle around the magnetic field line. A series of transformations allows one to remove the dependence on α, while retaining the information on the fields variation at the Larmor scale and to express the perturbed fields with a further change of coordinates to the gyro-centers $(\mathbf{x}_{GC}, v_{\parallel_{GC}}, \mu, \alpha)$. Note that, in these transformations, the *gyro-average* operator $\mathcal{J}(f)$ is used to make the change in position and in coordinates. In Fourier space, the gyro-average operation leads to the multiplication by the order 0 Bessel function $\mathcal{J}_0$ of argument $\mathbf{k}_\perp \cdot \boldsymbol{\rho}$ [22]

$$\widehat{f_{GC}} = \widehat{J}(f) = \mathcal{J}_0(\mathbf{k}_\perp \cdot \boldsymbol{\rho})\widehat{f}(\mathbf{k})$$

where $\mathbf{k}$ is the wave vector, $\mathbf{k}_\perp$ its projection in the perpendicular direction to the magnetic field and the hat notation refers to the quantities in Fourier space. In the resulting system, the magnetic moment is a conserved quantity, therefore the dimensionality of the problem is reduced to 4 dimensions (three in the real space and the parallel velocity) plus the adiabatic invariant μ. The gyro-centers, of which the position and parallel velocity are evolved in the gyrokinetic equation, correspond not simply to the centers of the Larmor gyration orbits but to the current rings resulting from the gyro-motion. The latter have finite extension is space and are magnetized and can be polarized. The gyrokinetic Vlasov equation in Lagrangian form then reads:

$$\frac{\partial f_{GC}}{\partial t} + \frac{d\mathbf{x}_{GC}}{dt}\frac{\partial f_{GC}}{\partial \mathbf{x}_{GC}} + \frac{dv_{\parallel_{GC}}}{dt}\frac{\partial f_{GC}}{\partial v_{\parallel_{GC}}} = 0 \tag{2.7}$$

The electromagnetic field and quasi-neutrality equation

The system is closed by coupling the gyrokinetic equation 2.7 to the Maxwell equation for the electric field $\mathbf{E}$ and magnetic field $\mathbf{B}$. One can define the electromagnetic potentials $\phi, \mathbf{A}$ such as:

$$\mathbf{B} = \boldsymbol{\nabla} \times \mathbf{A} \tag{2.8a}$$
$$\mathbf{E} = -\boldsymbol{\nabla}\phi - \partial_t \mathbf{A} \tag{2.8b}$$

Using the Lorentz gauge $1/c^2\partial_t\phi + \nabla \cdot \mathbf{A}$ with $c^2\epsilon_0\mu_0 = 1$, c being the speed of light, ϵ_0, μ_0 the electric and magnetic vacuum permittivity, one can rewrite the Maxwell equations

as:

$$\left(\frac{1}{c^2}\partial_t^2 - \nabla^2\right)\phi = \frac{1}{\epsilon_0}\sum_{species} n_s q_s \tag{2.9a}$$

$$\left(\frac{1}{c^2}\partial_t^2 - \nabla^2\right)\mathbf{A} = \mu_0 \sum_{species} \mathbf{j}_s \tag{2.9b}$$

Here the species density $n_s = \int f_s d\mathbf{v}$ and current $\mathbf{j}_s = q_s \int f_s \mathbf{v} d\mathbf{v}$ are the particle charge and electric current density that depart from that of the gyro-centers by finite Larmor radius corrections. These equations can be rewritten in dimensionless units to evidence the control parameters of the system. We chose a reference time t_*, a reference length l_*, a reference electric potential $\phi_* = T_{e0}/e$, with T_{e0} the reference electron temperature and e the unit charge, n_0 the reference plasma density, the reference vector potential $A_* = l_* B_0$, B_0 being the magnetic field amplitude at the magnetic axis, $j_* = p_0/l_* B_0$ with p_0 the reference plasma pressure. The choice of normalization for the electric potential and current is wall suited for plasmas since $e\phi/T_e$ characterizes the electron adiabatic response stemming from the electron momentum balance, and j_* is set according to the total plasma momentum balance in the transverse direction. Equations 2.9a and 2.9b then take the form:

$$\left(\mathcal{A}\partial_t^2 - \nabla^2\right)\phi = \mathcal{B}\sum_{species} n_s z_s \tag{2.10a}$$

$$\left(\mathcal{A}\partial_t^2 - \nabla^2\right)\mathbf{A} = \mathcal{C}\sum_{species} \mathbf{j}_s \tag{2.10b}$$

where now all the quantities are dimensionless and the control parameters are:

$$\mathcal{A} = \frac{l_*^2}{c^2 t_*^2} \quad ; \quad \mathcal{B} = \frac{n_0 e^2}{\epsilon_0 T_{e0}} l_*^2 = \frac{l_*^2}{\lambda_D^2} \quad ; \quad \mathcal{C} = \frac{\mu_0 p_0}{B_0^2} = \beta$$

The following asymptotic limits on these control parameters are relevant for fusion plasmas:

- Setting $\mathcal{A} \to 0$, one assumes the phenomena of interest to have characteristic velocities much slower than the speed of light $l_*/t_* \ll c$. This is the *electrostatic* asymptotic limit. In this limit, the time evolution of the electromagnetic field in the Maxwell equations 2.9 can be ignored.

- Setting $\mathcal{B} \to +\infty$ one assumes that the spatial scales of variation of the electric potential ϕ are much bigger than the Debye length λ_D. This is the *quasi-neutral* limit $\sum_{species} n_s q_s = 0$. At spatial scales larger than the Debye length, the charge density of the plasma system is null.

- Setting $\mathcal{C} \to 0$ one assumes that the characteristic plasma pressure p_0 is much smaller than the magnetic pressure $B^2/2\mu_0$. This limit is reasonable for magnetized plasmas, since magneto-hydro-dynamics stability sets an upper limit to β in the range of a few percent. Regarding the magnetic field amplitude, the main contribution will therefore be the external magnetic field, varying on the scale of the confinement device. One therefore considers the magnetic field amplitude to vary on large spatial scales compared to the Larmor radius $\rho|\nabla B/B| \ll 1$.

In this analysis, we have assumed that the scale l_* characterizes the large scale variation of the magnetic field as well as the transverse variation scale of the density or pressure fields, typically $\ell_* \approx a$ where a is the plasma minor radius. Furthermore, we have assumed the characteristic time t_* to be l_*/v where v is a characteristic ion velocity, ρ being the associated ion Larmor radius. The specific dimensionless plasma parameter $\rho_* = \rho/a$ appears in this analysis. These three asymptotic limits are not independent since the relation $c^2\epsilon_0\mu_0 = 1$ enforces:

$$\frac{\mathcal{AB}}{\mathcal{C}}\rho_*^2 = 1 \tag{2.11}$$

This constraint is important when recovering the charge conservation equation from the Lorentz gauge. In the following we shall assume that the three limits hold so that in particular equation 2.10a is reduced to the quasi-neutrality limit, which can be rewritten when separating the electron and ion contributions as:

$$en_e = \sum_{ions} n_i q_i \tag{2.12}$$

While the gyrokinetic equation is solved for the distribution function of gyro-centers f_{GC_s}, and therefore it is evolved in the gyro-centers phase space, in the quasi-neutrality equation the charge density $n_s = \int f_s d\mathbf{v}$ for each species s is the actual particle density, in the position-velocity phase space. This feature is governed by the fact that the Maxwell equations relate the electromagnetic fields to the fluid projection of the distribution function, namely the density, the zero-moment, and the particle flux, the first moment. Once the distribution functions are computed in the gyrokinetic framework, a pullback transformation from the gyro-centers to the particle phase space $f_{GC_s} \to f_s$ is necessary to compute the fields. The relation between the distribution function in the two reference systems is the following [23, 24]:

$$f_s = f_{GC_s} + \frac{e}{B}\partial_\mu \overline{f}_{GC_s}\big(\phi - \phi_{GC}\big) \tag{2.13}$$

where $\phi_{GC} = \mathcal{J}\phi$ is the gyro-averaged electric potential and $\overline{f}_{GC}$ is an equilibrium distribution of gyro-centers for each species s. The latter is a linearized version of this relationship since the equilibrium distribution function that is introduced at this step is that of the unperturbed state with $\phi = 0$. Furthermore, relation 2.13 is written at the particle location, so that a further transformation is required to determine the particle density at the gyro-center location where the electromagnetic fields are applied. When integrating $\mathcal{J}f_s$ over the velocity space, one then obtains the required particle density n_s. Given Equation 2.13 this expression combines the density associated to the distribution $\mathcal{J}f_{GC_s}$ and therefore determined by the gyro-center distribution function solution of the gyrokinetic equation f_{GC_s}, together with a polarization contribution n_{pol_s}.

$$n_{pol_s} = \int d^3v\ \mathcal{J}\Big(\frac{e}{B}\partial_\mu \overline{f}_{GC_s}\big(\phi - \mathcal{J}\phi\big)\Big) \tag{2.14}$$

The polarization term derives from the mismatch between particle and gyro-center reference systems, which governs a shift of the order of the Larmor radius. However, the gyro-phase independent contribution is a term of order two in the Larmor radius. When the electron density variation is found equal to zero, this term becomes important since

it is the only one that can balance the variation of the ion gyro-center density in the quasi-neutrality equation. For example, if the perpendicular velocity of a particle is not constant along the Larmor orbit, the particle will spend more time on a specific arc of the orbit than on the other. When averaging the cyclotron motion, these differences disappear. However, the fields are modified by these small scales effects: the polarization term accounts for the electric field response driven on the Larmor scale and proportional to the applied electric field. A further approximation of the polarization term can be derived in the large wave length limit $k_\perp \rho_s \ll 1$, with $k_\perp$ the perpendicular component of the wave vector $\mathbf{k}$, and reads:

$$n_{pol_s} = \boldsymbol{\nabla} \cdot \left(\frac{n_{eq_s} m_s}{q_s B^2} \boldsymbol{\nabla}_\perp \phi \right) \tag{2.15}$$

The latter term is small with respect to the gyro-center density, of the order $\rho_{*_s}^2$ and is therefore a second order correction to the electric potential. In this expression the density n_{eq_s} is the the particle density associated to the reference distribution $\overline{f}_{GC_s}$, and provided the difference with respect to the actual gyro-center distribution function is of order ρ_* is a consistent lowest order approximation to determine n_{pol_s}. The latter term will be shown to only play a leading role when considering the flux surface averaged electric potential profile taking the form of a kind of radial inertia in the build-up of the zonal structures. As such, one finds that the shearing rate of the zonal flows is typically proportional to this term. It can then be argued that given the importance of this physics, accurate expressions are crucial. However, these would not be consistent with the chosen ordering and expansion at lowest order in ρ_*. Stepping beyond the present form, especially without introducing symmetry breaking and only improving the accuracy, would require an alternative gyrokinetic framework, including as reference condition an arbitrary profile of the flux-surface averaged electric potential. Finally, it is very likely that the departure from the adiabatic electron approximation has a stronger impact on the zonal flow shearing rate as well as on the profile of the flux-surface averaged electric potential.

The adiabatic electrons limit

When addressing the physics of ion heat transport one refers to the ion scales both in space and in time. The asymptotic limit on the electron-to-ion mass ratio $m_e/m_i \to 0$ then governs a scale separation so that at lowest order one can assume the electrons to be at mechanical equilibrium, not only along the field line and also, by extension, on a flux surface. In the isothermal limit such that $\nabla_\parallel T_e \sim 0$, the electron density is then approximated by:

$$n_e = \langle n \rangle_{e0} \exp\Big(\frac{e\big(\phi - \langle \phi \rangle_0\big)}{T_e} \Big) \tag{2.16}$$

where $\langle n \rangle_{e0}$ and $\langle \phi \rangle_0$ correspond to the flux-surface averaged electron density and potential. Assuming small fluctuations of the electric potential one can linearize the exponential in equation 2.16 then yields:

$$n_e = \langle n \rangle_{e0} \left[1 + \frac{e\big(\phi - \langle \phi \rangle_0\big)}{T_e} \right] \tag{2.17}$$

The latter expression known as the adiabatic electron response is obtained using two approximations, the infinite mass ratio, and the extension of the adiabatic electron response to the flux surface, assuming, implicitly here, large $E \times B$ poloidal convection. It can be

noted that the mass ratio asymptotic limit deals in fact with the square root of the mass ratio $\sqrt{m_e/m_D} \approx 1/60 \gg \rho_*$. Stepping to kinetic electrons can therefore have a considerable impact on the zonal flow magnitude and one can expect this symmetry breaking, namely the variation of $\langle n \rangle_e$, to be more significant than addressing the non-linearity of the polarization term.

Equations of motion

The gyrokinetic framework is embedded in the Hamiltonian formalism so that the gyrokinetic equation, like the kinetic equation 2.5a, directly involves the equations of motion. These are shown to depend on the vector $\boldsymbol{B}_s^*$ which for species s defines the Jacobian $B_{\parallel s}^*$ of the coordinate transformation.

$$\boldsymbol{B}_s^* = \boldsymbol{B} + \frac{m_s v_\parallel}{q_s} \boldsymbol{\nabla} \times \left(\frac{\boldsymbol{B}}{B} \right) \tag{2.18a}$$

$$B_{\parallel s}^* = \boldsymbol{b} \cdot \boldsymbol{B}_s^* = \frac{\boldsymbol{B} \cdot \boldsymbol{B}_s^*}{B} = B + \frac{m_s v_\parallel}{q_s} \, \boldsymbol{b} \cdot \left(\boldsymbol{\nabla} \times \boldsymbol{b} \right) \tag{2.18b}$$

The unit vector $\boldsymbol{b}$ is defined as $\boldsymbol{B}/B$. For simplicity the subscripts GC are not recalled from now on for the guiding center parallel velocity and position. The motion equations are then:

$$B_{\parallel s}^* \frac{d\mathbf{x}}{dt} = v_\parallel \mathbf{B}_s^* + \frac{1}{q_s B} \mathbf{B} \times \boldsymbol{\nabla} \Xi_s \tag{2.19a}$$

$$B_{\parallel s}^* \frac{dv_\parallel}{dt} = -\mathbf{B}_s^* \cdot \boldsymbol{\nabla} \Xi_s \tag{2.19b}$$

$$B_{\parallel s}^* \frac{d\mu}{dt} = 0 \tag{2.19c}$$

The potential Ξ_s is defined by:

$$\Xi_s = q_s \mathcal{J} \phi + \mu_s B \tag{2.20}$$

Given this expression one ten obtains the following equations for the guiding center motion.

$$B_{\parallel s}^* \frac{d\mathbf{x}}{dt} = B \Big(v_\parallel \mathbf{b} + \boldsymbol{v}_J + \boldsymbol{v}_D + \boldsymbol{v}_E \Big) \tag{2.21a}$$

$$B_{\parallel s}^* \frac{dv_\parallel}{dt} = -q_s \nabla_\parallel \mathcal{J} \phi - \mu_s \nabla_\parallel B + m_s v_\parallel \boldsymbol{v}_E \cdot \boldsymbol{\nabla} B - \frac{B}{v_\parallel} \boldsymbol{v}_J \cdot \boldsymbol{\nabla} \Xi \tag{2.21b}$$

where:

$$B \boldsymbol{v}_E = \frac{1}{B} \mathbf{B} \times \boldsymbol{\nabla} \mathcal{J} \phi \tag{2.22a}$$

$$B \boldsymbol{v}_D = \frac{m_s v_\parallel^2 + \mu_s B}{q_s B^2} \boldsymbol{B} \times \boldsymbol{\nabla} B \tag{2.22b}$$

$$B \boldsymbol{v}_J = \frac{m_s v_\parallel^2}{q_s B} \boldsymbol{\nabla} \times \boldsymbol{B} \tag{2.22c}$$

Since $\overline{\phi}$ is a gyro-phase averaged quantity, it depends on the Larmor radius and consequently both on velocity and species. The three drift velocities defined above are therefore

kinetic and species dependent. In the following, unlike what we consider in the asymptotic limit for the Maxwell-Ampère equation 2.9b, hence $\beta \to 0$ ($\mathcal{C} \to 0$), we cannot assume $\boldsymbol{\nabla} \times \boldsymbol{B} = \mathbf{0}$ because the chosen equilibrium is sustained by large plasma currents and assumes a non vanishing β. One must therefore split the assumption on the magnetic field into an equilibrium contribution that yields a drift velocity $\boldsymbol{v}_J$ that must be taken accounted for and magnetic fluctuations that are not taken into account in the present version.

2.2.3 Equations in GYSELA

We summarize hereafter the equations solved by the GYSELA code. For the simulations performed in this thesis we consider a single ion species with adiabatic electrons. The code solves the following gyrokinetic equation for the main ion species:

$$\partial_t F_i + \frac{1}{B^*_\parallel} \nabla_z \Big(B^*_\parallel \dot{\mathbf{z}} F_i \Big) = \mathcal{C} + S_{Heat} - S_{ink} \tag{2.23a}$$

Here $\mathbf{z} = (\mathbf{x}, v_\parallel)$ is the 4-D phase space coordinate of the gyrokinetic framework. Taking into account the conservation of phase space volume, namely $\nabla_z (B^*_\parallel \dot{\mathbf{z}}) = 0$, one can write the alternative form of the gyrokinetic equation:

$$\partial_t F_i + \dot{\mathbf{x}} \boldsymbol{\nabla}_x F_i + \dot{v}_\parallel \partial_{v_\parallel} F_i = \mathcal{C} + S_{Heat} - S_{ink} \tag{2.23b}$$

In this equation, F_i is the distribution of gyro-centers and therefore all coordinates that appear in the equation are gyro-center coordinates. the equations of motions are given by Equation 2.22. On the right hand side are the terms driving the physics that are not part of the Vlasov equation of the left hand side: the collision operator $\mathcal{C}$, the heat source S_{Heat} and sink S_{ink}. The two latter are necessary in flux-driven simulations, see Section 2.3.1. Although fusion plasmas are weakly collisional, adding a description of the Coulomb collisions between particles is important to smooth out the distribution function in velocity space and avoid generating sub-scale velocity structures [25]. From the physics point of view, synergy between turbulent and neoclassical transport can also be expected and investigated [26, 27, 28, 29]. An important contribution of collisions is found in the regulation of the self-generated zonal flows [6]. Also, the neoclassical transport can reveal dominant in certain conditions of reduced turbulence, such as in presence of a transport barrier.

The quasi-neutrality equation in the GYSELA system reads:

$$-\nabla \cdot \left(\frac{n_{eq_e} m_i}{q_i B^2} \nabla_\perp \phi \right) + \frac{n_{eq_e} e}{T_e} \big(\phi - \langle \phi \rangle_{FS} \big) = e \int 2\pi \frac{B^*_\parallel}{m_i} d\mu dv_\parallel \; \mathcal{J} \cdot \big(F_i - F_{e,eq} \big) \tag{2.24}$$

where the function of the electric potential is separated from the terms depending only on the distribution function of ion gyro-centers. $2\pi B^*_\parallel / m_i$ corresponds to the Jacobian of the gyro-center transformation in the velocity space. The first term on the left hand side is the ion polarization density. In the code a further approximation is made when ignoring the variations of the magnetic field, B is replaced by B_0. The second term is the linearized electron density. In the GYSELA system of coordinates, see section 2.3.2, the flux surface averaged potential is computed as:

$$\langle \phi \rangle_{FS} = \frac{\int \phi \mathcal{J}_x d\theta d\varphi}{\int \mathcal{J}_x d\theta d\varphi} \tag{2.25}$$

where $\mathcal{J}_x = 1/(\boldsymbol{B}\cdot\boldsymbol{\nabla}\theta)$ is the Jacobian in the real space. With the chosen magnetic equilibrium, it is found proportional to rR where r the radial coordinate and R the distance from the magnetic axis, θ and φ are the poloidal and toroidal angles respectively. In the adiabatic electron framework, the electron density n_{eq_e} is not evolved and it is taken as reference density for the equilibrium n_{e_0}. The quasi-neutrality equation ensures the charge balance for the system. Since the electron density profile is fixed, this model cannot generate perpendicular particle transport. It is to be noted that the slightest inaccuracy in the charge balance, for example due to numerical errors, translates into a spurious electric potential via the quasi-neutrality equation 2.24.

2.2.4 Linear analysis

We outline hereafter the linear analysis of the gyrokinetic Vlasov quasi-neutral system. The main goal of the linear approach is to find a general expression of the growth rate of the instability. Several approximation will be made so that the calculation can be performed analytically. The proposed derivation is useful to determine the key physics at play. As a side product of the derivation of the dispersion relation we obtain the expression of the linearized electron distribution function in the adiabatic limit.

We consider an electrostatic plasma composed by a single ion species and adiabatic electrons. Allowing for the simplification $\boldsymbol{v}_j = \mathit{boldsymbol}0$, the gyrokinetic Vlasov equation for either species s reads:

$$\left(\partial_t + \big(v_\parallel \mathbf{b} + \mathbf{v}_E + \mathbf{v}_D\big)\cdot\nabla + \Big(- \frac{q_s}{m_s}\nabla_\parallel \mathcal{J}\phi - \frac{\mu_s}{m_s}\nabla_\parallel B + \frac{v_\parallel}{B}\mathbf{v}_E\cdot\nabla B\Big)\partial_{v_\parallel}\right) F_s = 0 \quad (2.26)$$

For the sake of simplicity, we neglect in this Section the two force terms $\mu_s\nabla_\parallel B/m_s$ and $(v_\parallel/B)\mathbf{v}_E\cdot\nabla B$ so that the Vlasov operator $\mathcal{L}$ takes the form:

$$\mathcal{L}F_s = \left(\partial_t + v_\parallel\nabla_\parallel + \mathbf{v}_E\cdot\nabla + \mathbf{v}_D\cdot\nabla - \frac{q_s}{m_s}\nabla_\parallel\mathcal{J}\phi\ \partial_{v_\parallel}\right)F_s = 0 \quad (2.27)$$

The operator $\nabla_\parallel$ stands for the gradient in the parallel direction. We linearize the system by perturbing the gyro-centers distribution functions and the electric potential as:

$$F_s = \overline{F}_s + \widetilde{F}_s \qquad ; \qquad \phi = \overline{\phi} + \widetilde{\phi}$$

For simplicity we consider that there exists an equilibrium for the different gyro-center distribution functions $\overline{F}_s$ such that the corresponding electric potential is null $\overline{\phi} = 0$. The linearized gyrokinetic equation then reads:

$$\overline{\mathcal{L}}\ \widetilde{F}_s + \widetilde{\mathcal{L}}\ \overline{F}_s = 0 \quad (2.28a)$$

$$\overline{\mathcal{L}} = \partial_t + v_\parallel\nabla_\parallel + \mathbf{v}_D\cdot\boldsymbol{\nabla} \quad (2.28b)$$

$$\widetilde{\mathcal{L}} = \widetilde{\mathbf{v}}_E\cdot\boldsymbol{\nabla} - \frac{q_s}{m_s}\nabla_\parallel\mathcal{J}\widetilde{\phi}\ \partial_{v_\parallel} \quad (2.28c)$$

and $\widetilde{\mathbf{v}}_E = (\mathbf{B}\times\boldsymbol{\nabla}\widetilde{\phi})/B^2$. We project the perturbations $\widetilde{F}_s$, $\widetilde{\phi}$ on the Fourier modes for each effective angle:

$$\widetilde{g} = \sum_{\omega,\mathbf{k}} \widehat{g}\ e^{-i(\omega t - \mathbf{k}\cdot\mathbf{x})}$$

We then define the following frequency operators $\omega_\parallel$, ω_D, ω_*.

$$\omega_\parallel = v_\parallel k_\parallel \tag{2.29a}$$

$$\omega_D = \mathbf{v}_D \cdot \mathbf{k} \tag{2.29b}$$

$$k_\parallel \widehat{\mathcal{J}\phi} \partial_{v_\parallel} \overline{F} = i\overline{F} k_\parallel (T_s/m_s) \partial_{v_\parallel} \left(\mathrm{Log}\overline{F}_s\right) \frac{q_s \, \widehat{\mathcal{J}\phi}}{T_s} = i\overline{F} \, \overline{\omega}_\parallel \frac{q_s \, \widehat{\mathcal{J}\phi}}{T_s} \tag{2.29c}$$

$$\widehat{\mathbf{v}}_E \cdot \nabla \overline{F} = i\omega_* \, \overline{F} \, \frac{q_s \, \widehat{\mathcal{J}\phi}}{T_s} \tag{2.29d}$$

Here $k_\parallel$ is the parallel projection of the wave vector $\mathbf{k}$. The linearized gyrokinetic then allows one to express the perturbation of the distribution function as proportional to the electric potential.

$$\frac{\widehat{F}_s}{\overline{F}_s} = \left(\frac{\omega_* - \overline{\omega}_\parallel}{\omega - \omega_\parallel - \omega_D} \right) \, \frac{q_s \, \widehat{\mathcal{J}\phi}}{T_s} \tag{2.30}$$

This compact expression must be understood as the effect of the inverse operator of $\omega - \omega_\parallel - \omega_D$ on the electric potential perturbation. The simplifications that have be made above in the force term modify both the numerator, change in the frequency $\overline{\omega}_\parallel$ and adding a frequency related to the parallel bounce effect in the resonant operator $(\omega - \omega_\parallel - \omega_D)^{-1}$.

Let us first analyze the case of fast electrons such that $v_\parallel$ is much larger that the drift velocities, $\overline{\omega}_\parallel \gg \omega_*$ and $\omega_\parallel \gg (\omega - \omega_D)$. Furthermore, for the electrons we set $\mathcal{J} = 1$. The assumption of adiabatic electrons implies therefore that the parallel electron motion is faster than any other motion in the system. Furthermore, assuming a Maxwellian electron distribution function in the parallel velocity so that $\partial_{v_\parallel}\left(\mathrm{Log}\overline{F}_e\right) = m_e v_\parallel / T_e$. Equation 2.30 then yields for the electrons:

$$\frac{\widehat{F}_e}{\overline{F}_e} \approx \frac{\overline{\omega}_\parallel}{\omega_\parallel} \, \frac{e\widehat{\phi}}{T_e} \approx \frac{e\widehat{\phi}}{T_e} \tag{2.31}$$

which corresponds to the adiabatic electron response. Because of the large electron mobility, on the ion time scales, the electron distribution function perfectly adapts to the fluctuations of the electric potential. In this analysis, one has excluded the case $k_\parallel = 0$ since this would yield both $\omega_\parallel = 0$ and $\overline{\omega}_\parallel = 0$, in contradiction with the assumption used to obtain equation 2.31. It can be shown that the case $k_\parallel = 0$ discussed here can lead to $\omega_* = 0$ so that in this particular case $\widehat{F}_e = 0$. The calculation associated to this case leads in fact to the result: $\left\langle \widetilde{F}_e \right\rangle_{FS} = 0$ so that the proper way to take this result into account is to assume:

$$\widetilde{F}_e = \overline{F}_e \, \frac{e\Big(\widetilde{\phi} - \langle\phi\rangle_{FS}\Big)}{T_e} \tag{2.32}$$

where the notation $\langle\cdot\rangle_{FS}$ stands for the flux surface average.

We now derive the dispersion relation for the linearized system. Setting the operator $\mathcal{J} = 1$ also for the ions, then the the quasi-neutrality equation in Fourier space reads:

$$\int \widehat{F}_e d\mathbf{v} = \int \widehat{F}_i d\mathbf{v} \tag{2.33}$$

Substituting Equations 2.30 for the ions and the solution 2.31 for the electrons into 2.33, we obtain the dispersion relation:

$$\left[\frac{T_i}{T_e}n_{0_e} + \int d^3v\ \overline{F}_i\ \left(\frac{\omega_* - \overline{\omega}_\parallel}{\omega - \omega_\parallel - \omega_D}\right)\right]\widehat{\phi} = \mathcal{D}_\omega\big(\widehat{\phi}\ \big) = 0 \tag{2.34}$$

It is important here to keep in mind that the denominator in this expression is the inverse of an operator acting on ϕ. Non vanishing modes are therefore the solutions of this dispersion relation, hence they belong to the Kernel of the operator $\mathcal{D}_\omega$. For imaginary solutions $\omega = i\gamma$ and $\gamma > 0$, the system is unstable. One can reduce the domain of interest for the frequencies by assuming a certain ordering of the terms in the denominator. For the ions, one assumes the limit $\omega \gg \omega_\parallel \gg \omega_D$ so that one can expand the fraction, thus approximating the inversion of the operator. A derivation of the linear growth rate for the Ion Temperature Gradient (ITG) instability can be found in [30] as a threshold on the value $\eta = \nabla_r \mathrm{Log}(T_i)/\nabla_r \mathrm{Log}(n_i)$. As a first approximation one can assume the system to be unstable for $\eta > 2$, therefore:

$$\eta = \frac{\nabla_r \mathrm{Log}(T_i)}{\nabla_r \mathrm{Log}(n_i)} = \frac{L_{n_i}}{L_{T_i}} \qquad ; \qquad \frac{R}{L_{T_i}} \geq 2\frac{R}{L_{n_i}} \tag{2.35}$$

One should also mention a study of the ITG threshold with linear gyrokinetic simulations [31], which yields the following fitting expression for the threshold on the ion temperature gradient scale:

$$\frac{R}{L_{T_i}} \geq max\Big\{\left(1 + \frac{T_i}{T_e}\right)\left(1.33 + 1.91\frac{s}{q}\right); 0.8\frac{R}{L_{n_i}}\Big\} \tag{2.36}$$

where R is the major radius, L_{T_i}, L_{n_i} the characteristic gradient lengths of the profiles for the ion temperature and ion density respectively, $s = r\nabla_r log(q)$ the magnetic shear, and q is the safety factor.

2.3 Towards thought experiments: global and flux-driven simulations

A specific aspect of the GYSELA code is that it evolves the entire distribution function without separating the equilibrium scales from the fluctuation scales, as done for example in the linear analysis. This approach is called *full-f* and involves spatial scales from the ion Larmor motion to the plasma size, time scales from the integration time step, comparable to the period of the Larmor rotation up to the evolution time scales of the global equilibrium. In terms of physics, this allows for back reaction of the turbulent fluctuations on the equilibrium scales and vice-versa. Therefore large scales flows such as the zonal flows, quasi-steady poloidally and toroidally symmetric flows, are self-generated in the evolution of the system [26, 32]. These flows play a crucial role in the regulation of turbulent transport [33]. Modeling the self-evolution of the zonal flows is important both for understanding the turbulent transport mechanisms and for predicting the confinement. More generally, one can expect that the transport self-organization, exemplified above by the importance of the zonal flow evolution and properties, will introduce intermediate scales between that of the micro-turbulence drive and the global scales that govern fusion performance. The relevance of these intermediate scales, their statistical properties, can only be addressed properly in such global, full-f and flux driven, settings.

2.3.1 An open system covering all relevant scales

In the full-f framework, the equilibrium plasma is not prescribed and can evolve during the simulation. This fact has three main consequences:

(i) from the physics point of view, the system can relax its energy content towards a stable state. A heat source must be added (S_{Heat} when aiming at sustaining plasmas characterized by high fusion performance, typically by increasing the plasma pressure. In GYSELA, the heat source in equation 2.23)[32] builds the plasma profiles and sustains the gradients above the linear threshold, consequently driving turbulent transport. The outer boundary condition of the code acts as a heat sink S_{ink}. The heat transport in the system is a balance between these two terms. This approach is called *flux-driven* regime and reproduces the characteristic of the plasma which is an open system, where the heat is transported from the very core all across the plasma and it is released at the first wall. In GYSELA, the heat source is located in the core region and does not evolve in time [32]. Consequently the heat flux extracted in the heat sink should not be prescribed *a priori* but should result from the transport regime. The heat sink only extracts the heat that reaches the boundary. A self-consistent heat sink that captures our understanding of the physical mechanisms that occur in actual boundary layers in magnetic confinement devices is described in Chapter 4.

(ii) Although the GYSELA model does not allow for scale separation between equilibrium and fluctuating fields, a considerable difference between the evolution scales of these two actually exists. One can consider that the time evolution of the background profiles takes place on scales of the order of the confinement time $\tau_E \sim 4 - 6s$, while the typical time of turbulence, identified by the instability growth rate, Equation 2.1b, which is of the order of $\tau_{\|} \sim 10^{-4}s$. Achieving the steady state for the equilibrium field is at most 4 orders of magnitude longer than for turbulent fluctuations. This fact brings substantial issues on numerical simulations. For example, when running long simulations any systematic error builds-up so that the simulation can gradually be less and less accurate. Since numerical schemes are based on approximations, numerical errors are inevitable and one must then either show that there are no systematic errors, or that the errors drive the simulation away from the initial trajectory away from the exact one, but close to a trajectory that is relevant but for a setting that cannot be distinguished from that of the exact one. Another issue is that of resources since the build-up of the plasma gradients from flat profiles up to statistically steady state is in most cases too long to be performed. Typical runs with GYSELA correspond to a physical time of the order of $0.1\tau_E$. This means that an initial state, more or less close to the equilibrium, has to be chosen. For such short time interval compared to the confinement time, the evaluation of the equilibrium state is an issue. A technique to establish if a simulation is close to the equilibrium state is presented in Chapter 3.

(iii) A third consequence of a full-f code concerns the initialization. As we have discussed in the previous point, an initial state for the simulation has to be chosen[34, 35, 36]. This state is very likely not an equilibrium state for the turbulent regime. An initial phase of reorganization of the distribution function therefore develops before the linear growth of the turbulent modes. In most global simulations, the choice of the initial distribution functions generates Geodesic Acoustic Modes (GAM) [37], global toroidally symmetric modes oscillating at a given frequency that spatially propagate from the center to the plasma edge. However, for a particular case, it has been shown that the steady state turbulent regime in the GYSELA simulation did not depend on the choice of a

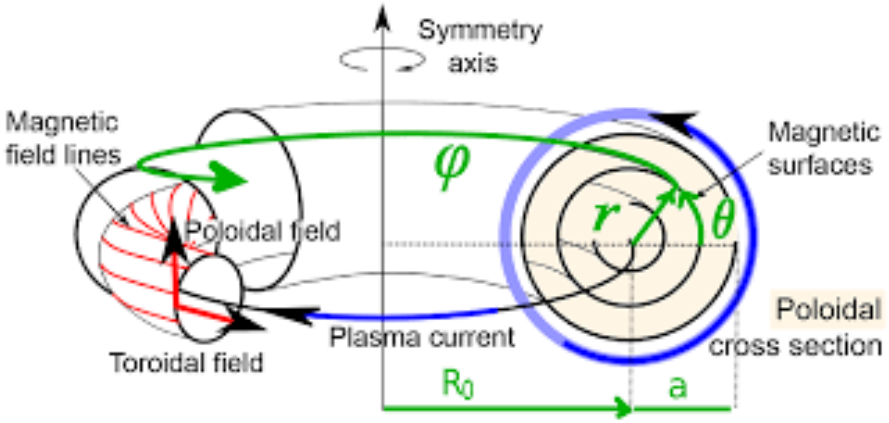

Figure 2.2: Geometrical system of coordinates for a magnetic configuration of circular and concentric flux surfaces.

particular initial state [38]. In other words, that a single region was explored in the steady state regime, and that such a region appeared to be a basin of attraction for different initial conditions. Such a result can be expected when a single state exists but can be questionable in the vicinity of a bifurcation.

2.3.2 Full-toroidal geometry

Consistently with such a global model, the numerical domain of the code extends over the whole toroidal volume of the plasma [39]. The magnetic configuration is simplified to toroidal concentric flux surfaces of circular cross section, similar to the Tore Supra configuration. It is to be noted however that regarding Tore Supra experiments, the magnetic surfaces were circular but mot of the time not concentric. Such a specific case would require zero Shafranov shift, hence a large poloidal beta value, up to four times that achieved in routine operation. A trade-off between different possibilities has led to a conservative choice of coordinate system, namely that corresponding to standard geometric toroidal coordinates (r, θ, φ), respectively the radial direction and the geometrical poloidal and toroidal angles (Figure 2.2). This choice will be adopted for the rest of the manuscript. The magnetic field is expressed as:

$$\mathbf{B} = B_\theta \mathbf{e}_\theta + B_\varphi \mathbf{e}_\varphi \tag{2.37}$$

Here $\mathbf{e}_\theta = r\nabla\theta, \mathbf{e}_\varphi = R\nabla\varphi$ are the unit vectors on the poloidal and toroidal directions respectively. Assuming axisymmetry, the toroidal magnetic field is given by the Ampere law $B_\varphi = B_0 R_0/R$ where B_0 is evaluated at the magnetic axis and $R = R_0 + r cos(\theta)$. The poloidal field can be expressed through the definition of the local field lines pinch, which in this specific choice of coordinates reads

$$\left.\frac{d\varphi}{d\theta}\right|_{field\ line} = \frac{\mathbf{B}\cdot\boldsymbol{\nabla}\varphi}{\mathbf{B}\cdot\boldsymbol{\nabla}\theta} = \frac{B_\varphi r}{B_\theta R} = \frac{\overline{q}(r)}{1+\epsilon cos(\theta)} \tag{2.38}$$

where $\overline{q}(r)$ is a chosen radial function, generally monotonically increasing with radius and $\epsilon = r/R$. The poloidal magnetic field is then given by $B_\theta = B_\varphi r/\overline{q}(r)R_0$ and has the same poloidal dependence on a magnetic surface $r = constant$ as the toroidal field B_φ.

The safety factor, defined as the average field line pitch, is then:

$$q = \frac{1}{2\pi}\int_0^{2\pi} \frac{\mathbf{B}\cdot\boldsymbol{\nabla}\varphi}{\mathbf{B}\cdot\boldsymbol{\nabla}\theta}d\theta = \frac{\overline{q}(r)}{\sqrt{1-\epsilon^2}} \tag{2.39}$$

With this particular choice of the magnetic equilibrium, the dependence of the parallel connection length on θ can be analyzed by considering that $ds/d\theta = B/(\mathbf{B}\cdot\boldsymbol{\nabla}\theta) \approx \overline{q}R_0$ and does not depend on θ. The connection length is the same from bottom to top both via long field and via high field side of the poloidal section.

$$l_{\parallel} = \int_{-\pi/2}^{\pi/2} R\frac{\mathbf{B}\cdot\nabla\varphi}{\mathbf{B}\cdot\nabla\theta}d\theta = \int_{-\pi/2}^{\pi/2} R_0\big(1+\epsilon cos(\theta)\big)\frac{\overline{q}(r)}{1+\epsilon cos(\theta)}d\theta = \pi R_0\overline{q}(r) \tag{2.40}$$

We note that a different choice of the poloidal angle can be made to define a different system of coordinates, for which the pitch angle Equation 2.38 only depends on the radial coordinate. These different systems of angle coordinates θ^*, φ^* that satisfy $d\varphi^*/d\theta^* = q(r)$ are called *flux coordinates* and are widely used in analytical derivations. The difference between these systems is detailed in Appendix A.

Chapter 3

Global versus local confinement properties

The energy confinement time τ_E is a key parameter that summarizes the performance of a fusion reactor. By definition it expresses the typical time of confinement of the energy inside the plasma volume. For a statistical steady state, it is determined by the ratio between the internal energy and the power source in the system. Basically it defines the quality of the energy confinement and is comparable to the thermal resistivity to evaluate the insulation property of a given medium. In fusion plasmas, it is determined by the self organization of the energy transport between the heat source, an external heating mechanism or fusion reactions mostly localized in the plasma core, and the heat flux at the boundary of the system, namely the power loss[1]. The energy confinement time is by definition a global parameter of the system. Given the high non-linearity of the physics at play, only crude analytical models are available, which are not reliable enough predict with the required accuracy the energy confinement time of future and essentially bigger machines. The design of new devices such as ITER and DEMO is based upon the extrapolation of experimental scaling laws, where the energy confinement time is expressed as a power law of the main plasma control parameters[1][11]. At present, the reference scaling for high confinement regime is the following

$$\Omega_i \tau_{th,IPB98(y,2)} \sim \rho_*^{-2.69} \beta^{-0.9} \nu_*^{0.08} M^{0.96} q^{-3.0} A^{-0.73} \kappa^{3.29} R^{-0.01} \tag{3.1}$$

where ρ_* is an plasma effective size parameter, β the ratio between the plasma pressure and the magnetic pressure, ν_* the normalized plasma collisionality, M the mass ratio between plasma ions and the proton, q the safety factor, $/A$ the aspect ratio, κ the plasma elongation, namely the ratio between the minor radius and the plasma height. The above scaling law addresses the confinement of a set of devices with comparable geometry and operating in an improved confinement mode, the so-called H-mode. Such scaling laws are still matter of research and new dependencies are proposed [40]. Note that $\Omega_i \tau$ is dimensionless so that the right hand side of equation (3.1) is also expected to be dimensionless. Since all the control parameters in (3.1) are normalized but for the last term $R^{-0.01}$, one must assume that the dependence on major radius R must be R^0 so that the exponent -0.01 is therefore indicative of the characteristic error on the exponents of the scaling law.

[1] when core radiative losses are significant, these must be subtracted from the heating power

The idea of building a scaling law for the energy confinement time is based on the assumption of similarity between plasma states characterized by the same set of normalized control parameters, as also considered for neutral fluids turbulence described by Navier-Stokes equations [41, 42].

In this chapter we address this issue with GYSELA simulations. We define a reduced model for the energy confinement time in gyrokinetic and flux-driven simulations and we recover a scaling law of the energy confinement time in function of the plasma parameters. We also compare the transport properties between the global scale of the confinement device and the local characteristic scale of turbulence.

3.1 From 5-D to 0-D: the reduced model for the confinement time

The energy confinement time is understood as a characteristic time of variation of the internal energy in the plasma system. In practice, confinement cannot be perfect and the plasma must be regarded as an open system which tends to thermodynamic equilibrium with its environment, hence without forcing is turned off, the internal energy content W would decay away. The external drive that sustains the internal energy is the heating source P_{heat}. This heat flux is transported through out the plasma volume and is released at the boundary as the outgoing power flux P_{loss}. In the GYSELA code the mechanism generating the core plasma heating is not specified. It is devised to transfer bulk particles of the distribution function to suprathermal velocities, conserving the number of particles and momentum. The source has a prescribed radial profile with poloidal and toroidal symmetry. By construction the heat source does not fluctuate, it is thus constant in time.

The energy confinement time is defined as a coarse grained quantity over the whole toroidal plasma volume, that is the ratio between the total energy W stored in the system divided by the rate at which this energy is lost. This definition is appropriate when considering a quasi steady-state.

$$\langle P_{loss} \rangle \equiv \frac{\langle W \rangle}{\overline{\tau}_E} \tag{3.2a}$$

The internal energy balance equation is then $\langle P_{loss} \rangle = P_{heat}$ so that:

$$\frac{\langle W \rangle}{\overline{\tau}_E} = P_{heat} \tag{3.2b}$$

For such steady state conditions, the energy confinement time $\overline{\tau}_E$ is therefore a global coarse grained quantity relating the stored energy $\langle W \rangle$ to the available heating power P_{heat}. It is only relevant because this quantity was found to exhibit a scaling law with so called engineer parameters characterizing the operating point of the tokamak. In a regime of thermonuclear burn, the heating power can be related to the fusion power coupled to the plasma, typically proportional to W^2 and to the amplification factor $Q = P_{fus}/P_{add}$ where P_{fus} is the energy released by the fusion reactions and P_{add} is the external heating power. It is then possible to relate the design of the tokamak, hence the engineering parameters, to a target amplification factor Q.

When addressing the problem from a physics point of view, one considers in fact a reduced model, namely the energy balance equation for the plasma contained in the

toroidal volume up to radius $r \leq a$. The ion internal energy W of the system is extracted from GYSELA simulations as the volume integral of the flux surface averaged kinetic internal energy density, the latter corresponding here to 3/2 of the scalar pressure p, $W(r,t) = \int_0^r \langle \frac{3}{2} p \rangle_{FS}(r^*,t) r dr^*$ where the notation $\langle . \rangle_{FS}$ stands for the flux surface average. The internal energy function W is defined to be positive and increases therefore radially. One can think of the system as the ensemble of consecutive sections of increasing volume, one for each radial location following a reservoir model. For each of them, one can define the energy balance equation.

$$\partial_t W(r,t) + P_{loss}(r,t) = P_{heat}(r) \tag{3.3a}$$

Following the step leading to the definition of $\overline{\tau}_E$, one identifies the loss term $P_{loss}(r,t)$ to $W(r,t)/t_E(r,t)$ so that:

$$\partial_t \, W(r,t) + \frac{W(r,t)}{t_E(r,t)} = P_{heat}(r) \tag{3.3b}$$

One can then extract the characteristic time $t_E(r,t)$ from GYSELA results by inverting equation (3.3b) so that:

$$t_E(r,t) = \frac{W(r,t)}{P_{heat}(r) - \partial_t W(r,t)} = \frac{W(r,t)}{P_{loss}(r,t)} \tag{3.4a}$$

It is to be noted that the definition does not ensure that $t_E > 0$. After the first stage of coarse graining via the flux surface average, and considering close to equilibrium systems one can expect both $P_{heat}(r) > \partial_t W(r,t)$ and $P_{loss}(r,t) > 0$. However, in the very core region where $P_{heat}(r)$ can be small, transient heating by the outer plasma can occur, then leading to negative values of t_E. Conversely, towards the outer layer, where $P_{loss} > 0$ since there is no outer heat source, one expects $t_E > 0$. The time t_E expresses the instantaneous value of the energy confinement time that can be computed at each radial location.

In the data base of simulations used for this analysis, the source amplitude, hence P_{heat} is adjusted by a trial and error procedure to ensure that the chosen profiles initial profiles exhibit a small, close to zero, variation. When such a condition is fulfilled, the internal energy weakly departs from the initial internal energy $W_0 = W(t=0)$. Since:

$$t_E(r,t) = \frac{W(r,t)/P_{heat}(r)}{1 - \partial_t W(r,t)/P_{heat}(r)} \tag{3.4b}$$

the time average of the latter expression then yields:

$$\langle t_E(r,t) \rangle = \frac{\langle W(r,t) \rangle}{P_{heat}(r)} + \left\langle \frac{W(r,t)}{P_{heat}(r)} \Big(\frac{\partial_t W(r,t)/P_{heat}(r)}{1 - \partial_t W(r,t)/P_{heat}(r)} \Big) \right\rangle \tag{3.5a}$$

For a weak variation of the internal energy over the simulation time $\partial_t W/P_{heat} \ll 1$ and given that $\overline{\tau}_E(r) = \langle W(r,t) \rangle / P_{heat}(r)$, one obtains therefore:

$$\overline{\tau}_E(r) \approx \langle t_E(r,t) \rangle \tag{3.5b}$$

Given this result one can then define the energy confinement time as $\tau_E(r) = \langle t_E(r,t) \rangle$. Its evolution is determined by the turbulent state, which governs the variation of the

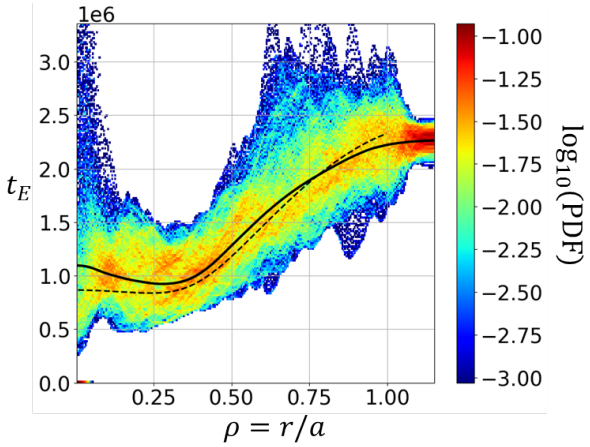

Figure 3.1: Example of the energy confinement time resulting from GYSELA simulations. Colors: Probability distribution function of $t_E(r,t)$ in time at each radial position. Solid line: the time average of t_E over a time interval of $2{\cdot}10^5\Omega_i^{-1}$, approximately $0.1t_E$. Dashed line: confinement time resulting from a diffusive model with constant diffusion coefficient.

internal energy $\partial_t W$. On figure 3.1 the probability distribution function (PDF) of $t_E(r,t)$ is shown at each radial location. The statistics is generated by variation in time for a close to steady sate simulation. At most radial positions, for example at $\rho = 0.34$ and $\rho = 0.56$, the probability distribution can be fitted by a Gaussian function. However, the PDF at other positions such as $\rho = 0.67$ exhibit a long right tail corresponding to transient events of enhanced confinement. In the neighborhood of these radial positions we have observed a quasi-stationary $E \times B$ shear layer, which is believed to increase the confinement by shearing the radially elongated turbulent structures. The time average of t_E defines the coarse grained energy confinement time at each radial position $\tau_E(r) = \langle t_E(r,t)\rangle_t$. The time interval considered for this average is typically to $2 \cdot 10^5\Omega_i^{-1}$, approximately $0.1\ \tau_E(r=a)$. Furthermore, we define the error on this measure as the standard deviation of the probability distribution for t_E at each radial location.

The radial behavior of the average t_E can be interpreted as follows: at small r, the confinement time weakly decreases. When considering the PDF, for $\rho = r/a \leq 0.25$ one can observe that the PDF tends to broaden as $r \to 0$. In particular, a heavy tale develops towards the large values of t_E. This would be indicative of a weak transport barrier. It is also observed that is this region the departure from the initial temperature profile is the largest, with a peaking of the profile typically for $\rho = r/a \leq 0.1$. However, the associated change in internal energy is of the order of 10^{-3}. The impact of this region remains small on the overall confinement. Ensuring the energy balance in the presence of such a barrier would require changing the source profile to reduce the source for $\rho \leq 0.1$.

After reaching a minimum where the source locally balances the losses around $r/a = 0.3$, the confinement time increases with radius, as expected from the radial build-up of the internal energy at near constant power loss. An important feature that appears in the PDF of t_E, figure 3.1, is that the distribution is relatively narrow and consequently the standard deviation is small.

The coarse graining process has been applied here on the expression of t_E, equation (3.5b). However, if would be more relevant to consider the average of the energy balance

equation, allowing for a separation between slow transients and fluctuations induced by the turbulent transport.

$$\partial_t \langle W(r,t)\rangle + \left\langle \frac{W(r,t)}{t_E(r,t)} \right\rangle = P_{heat}(r) \tag{3.6a}$$

Given the definition of $\overline{\tau}_E$, equation(3.2a), one then finds:

$$\left\langle \frac{W(r,t)}{t_E(r,t)} \right\rangle \equiv \frac{\langle W(r,t)\rangle}{\overline{\tau}_E(r,t)} \tag{3.6b}$$

and consequently:

$$\partial_t \langle W(r,t)\rangle + \frac{\langle W(r,t)\rangle}{\overline{\tau}_E(r,t)} = P_{heat}(r) \tag{3.6c}$$

Consistently with its definition $\overline{\tau}_E$ is the characteristic evolution time of the coarse grained internal energy. However its connection with t_E is not simply an average as made explicit in equation (3.6b) where one considers the average of $1/t_E$ weighed by the internal energy. Let us introduce the fluctuations of the internal energy, $W = \langle W\rangle + \widetilde{W}$ and of t_E, $t_E = \tau_E + \delta t_E$ such that $\langle \widetilde{W}\rangle = 0$ and $\langle \delta t_E\rangle = 0$, hence:

$$\left\langle \frac{\langle W\rangle + \widetilde{W}}{\tau_E + \delta t_E} \right\rangle = \frac{\langle W\rangle}{\overline{\tau}_E} \tag{3.7a}$$

One then obtains the following relationship between the two definitions of the confinement time:

$$\frac{\tau_E}{\overline{\tau}_E} = \left\langle \frac{1 + \widetilde{W}/\langle W\rangle}{1 + \delta t_E/\tau_E} \right\rangle \approx 1 + \frac{\left\langle \widetilde{W}^2 \right\rangle}{\langle W\rangle^2} + \frac{\langle \delta t_E^2\rangle}{\tau_E^2} - \frac{\left\langle \widetilde{W}\delta t_E \right\rangle}{\langle W\rangle \tau_E} \tag{3.7b}$$

The difference depends on second order correlations. When these are negligible one recovers $\tau_E = \overline{\tau}_E$. If this is not the case, the appropriate definition to be used to define τ_E, ensuring $\tau_E = \overline{\tau}_E$, is then:

$$\frac{1}{\tau_E(r,t)} \equiv \frac{1}{\langle W(r,t)\rangle} \left\langle \frac{W(r,t)}{t_E(r,t)} \right\rangle \tag{3.8a}$$

So that whenever $\widetilde{W} \ll \langle W\rangle$:

$$\frac{1}{\tau_E(r,t)} \approx \left\langle \frac{1}{t_E(r,t)} \right\rangle \tag{3.8b}$$

The two latter expressions underline the fact that when fluctuations are significant, the relevant quantity is $1/t_E$ rather than t_E.

Before analyzing the scaling properties of τ_E, it is interesting to compare the achieved radial profile of τ_E to that determined by a simple diffusive transport model in cylindrical geometry with constant diffusion across the radius, dashed line on Figure 3.1. For this model, we consider a steady state transport equation of the kind:

$$\nabla \cdot q = S \tag{3.9}$$

where on the left hand side is the divergence of the heat flux q and on the right hand side the radial heat source S. We assume the heat flux to satisfy the diffusion equation $q = -D\partial_r\mathcal{E}$ with $\mathcal{E}$ the density of internal energy. The volume integral of $\mathcal{E}$, of the heat flux q and of the heat source S correspond respectively to the internal energy W, the total power loss P_{loss} and the total heating power added P_{heat} of the 1D diffusive system. Using the transport equation (3.9) and the expression of the diffusive heat flux $q = -D\partial_r\mathcal{E}$, these latter quantities can be derived from the radial shape of the source S only.

However, considering the definition of the energy confinement time $\tau_D = W/P_{loss}$, the simple 1D diffusive model with a constant D then yields:

$$D\ \tau_D(r) = -\frac{W(r)}{r\partial_r(\frac{1}{r}\partial_r W(r))} \tag{3.10}$$

Since the chosen simulation set-up is such that $W(r,t) \sim W_0(r)$, namely such that the departure from the initial internal energy profile is small, the right hand side of equation (3.10) is determined by the chosen initial condition. Let us now define $\bar{D}(r)$ obtained by comparing the radial profile of τ_D and that of τ_E, here approximated by $\langle t_E \rangle$ as shown on figure 3.1:

$$\bar{D}(r) = \frac{D\tau_D(r)}{\tau_E(r)} = -\frac{1}{\tau_E(r)}\frac{W(r)}{r\partial_r(\frac{1}{r}\partial_r W(r))} \tag{3.11}$$

The dashed line on figure 3.1 is the curve $D\tau_D(r)$ which does not depart significantly from that of $\tau_E(r)$. As a consequence, the coefficient $\bar{D}$ is fairly constant over the whole radial domain, with variations of the order of few percents between $0.2 < r/a < 0.8$. It thus appears that the internal energy profile chosen as initial condition and sustained during the turbulent transport phase of the simulation is close to be consistent with a constant diffusion process. One issue is then to evaluate what is the impact of the observed departure on the actual internal energy profile. Should this effect be small, the remaining issue is how can a local ballistic heat transport, as observed in the simulations, translate into a global homogeneous diffusive like behavior when coarse grained. Both these issues are important, but require for a proper discussion to investigate a departure from the chosen profiles, hence exploring the phase portrait when varying parameters such as the density profile and the shape of the source term. This requires considerable simulation resources both in computing time and analysis of the results. Without an a priori understanding of the way to explore this parameter space, such a task was too challenging for the present research effort.

The energy confinement time in the experimental sense is computed considering the entire plasma volume up to the last close flux surface, identified here in the position $r/a = 1$. In the following we will refer to τ_E as the time average value $\langle t_E \rangle$ computed at the radial location $r/a = 1$. The error ϵ on this measure is taken as the standard deviation of the probability distribution in time at the same location. Given the normalization of the code, the physical quantity we compute is already the dimensionless confinement time normalized to the ion cyclotron frequency $\Omega_i\tau_E$. When extracting a single value of the confinement time, the transport given by the 5-D gyrokinetic simulations is reduced to a fully coarse grained 0-D model.

3.2 Similarity of the steady states

Following the standard procedure used to address the empirical scaling laws for the confinement time, we express the energy confinement time as a power law of three dimensionless parameters: the aspect ratio $A = R_0/a$, the plasma effective size expressed by the parameter $\rho_* = \rho_i/a$ and the plasma collisionality ν_*.

$$\Omega_i \tau_E = C A^{\alpha_A} \rho_*^{\alpha_\rho} \nu_*^{\alpha_\nu} \tag{3.12}$$

We compare simulations in which only one parameter is varied, all the others are kept constant. To achieve the steady state condition, the source amplitude is changed to compensate for the change in turbulent transport governed by the change in the control parameter. An ideal situation is achieved when two difference but quite close values of the source amplitude lead either to a slowly decreasing, respectively slowly increasing, internal energy. One can then consider that a lower and upper bound of the energy confinement time can be estimated from the data. As the data base is built-up, it is used to guide the choice of the source amplitude, this feed-back procedure replacing the initial trial and error steps. In particular, we perform the scan at constant internal energy value with respect to the normalized radius $\rho = r/a$. All the simulations discussed in the following converge towards the same steady state plasma pressure profile, close to the initial profile. The latter is thus maintained for the whole duration of the simulation, approximately one tenth of the energy confinement time. This condition is equivalent to having a constant ratio between the internal energy and the integral of the source profile. To clarify this point lest us use equation (3.4a) in steady state conditions.

$$t_E(\rho, t) = \frac{W(\rho, t)}{P_{heat}(\rho)} = \frac{\int d\mathcal{V} \ \langle p(r,t) \rangle_{F.S.}}{S_0 \int d\mathcal{V} \ \langle s(\rho) \rangle_{F.S.}} \tag{3.13a}$$

Here the source profile is chosen such that $S(\rho) = S_0 s(\rho)$ where $s(\rho)$ is given. Provided $\langle p(r,t) \rangle_{F.S.} \approx p(\rho, t = 0)$. For the particular choice of the geometry, nest concentric flux surfaces, the above expression can then be changed so that:

$$\tau_E(\rho) S_0 \approx \frac{\int d\rho' \ \rho' \ p(\rho')}{\int d\rho' \ \rho' \ s(\rho')} = \mathcal{C}_E(\rho) \tag{3.13b}$$

The function $\mathcal{C}_E(\rho)$ is a prescribed function of $\rho = r/a$ that only depends on the chosen conditions of this set of simulations. When considering a single point in the analysis, namely $\rho = 1$, the product $\tau_E S_0$ is only determined by the constraint $\tau_E S_0 = C_E$, where C_E is a given scalar such that $C_E = \mathcal{C}_E(\rho = 1)$.

$$\tau_E S_0 = C_E \tag{3.14}$$

Changing the control parameters in the simulation, consequently τ_E, must therefore be balanced by a corresponding change of the source amplitude S_0 to fulfill the condition of equation (3.14).

Since the magnetic geometry is the same for all the simulations, with circular concentric magnetic surfaces, the parameters β, q, κ are fixed for all the simulations in the database. We evolve the single species of Deuterium ions with adiabatic electrons, therefore also the parameter M is the same for all simulations. The coefficient C in equation

3.12 includes the dependency on parameters that are not considered in this study.

A collection of points with errors $(1 \pm \epsilon)\Omega_i \tau_E$ and their coordinates in the parameter space (A, ρ_*, ν_*) is extracted from the simulations result as described in Section 3.1. We compute the exponents $\alpha_A, \alpha_\rho, \alpha_\nu$ and the coefficient C by standard linear regression on the logarithm of equation 3.12, which is a linear equation of the form:

$$log(\Omega_i \tau_E) = log(C) + \alpha_A log(A) + \alpha_\rho log(\rho_*) + \alpha_\nu log(\nu_*) \tag{3.15}$$

A database of ~ 40 close to steady state simulations has been collected, costing an amount of ~ 3 millions of cpu hours. Simulations are run with the same choice of initial profiles, shown in figure 3.2. This set of profiles appears to be unstable for ITG turbulence over the full radial range and lead to a turbulent regime that extends also all over the poloidal section. The source term has a hyperbolic tangent radial shape which extends typically between $0 < r/a < 0.4$. At the radial outer boundary a poloidally symmetric restoring force acts as heat sink and drives the distribution function to exponential plasma profiles, namely standard profiles in the Scrape-Off Layer, enforcing a heat sink for $r/a > 1$.

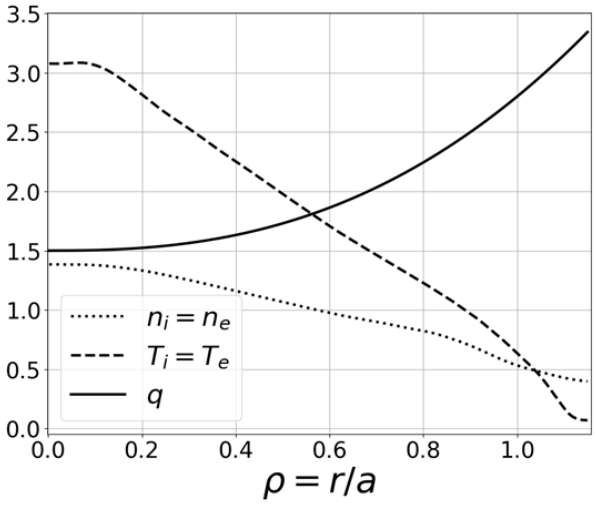

Figure 3.2: Initial profiles for the simulation dataset: in solid line is the safety factor, dotted line the density and dashed line the temperature.

3.2.1 Achieving steady state in flux driven simulations

Flux-Driven gyrokinetic global simulations use a heat source to build the plasma pressure profile and let the turbulence evolve. The statistical steady state condition is reached when all the profiles and consequently the internal energy fluctuate in the vicinity of a mean value that can be determined by time averaging on times shorter than the energy confinement time. As described in Section 2.3.1, one possible strategy to perform simulations on time scales comparable to the confinement time is to initialize the simulations directly close to the steady state. This can be obtained by tuning the initial profiles or the source term in order to match the equilibrium condition. In practice, as detailed above, only the source amplitude is changed between the simulations in the database.

One can take advantage of the scaling properties of the system to determine new equilibrium states: we scale the power source P of an already existent steady state simulation, called reference hereafter, using the power law for the energy confinement time in the parameter space as:

$$\frac{P_{new}}{P_{ref}} = \frac{(\Omega_i \tau_E)_{ref}}{(\Omega_i \tau_E)_{new}} = \frac{A_{ref}^{\alpha_A}\ \rho_{*ref}^{\alpha_\rho}\ \nu_{*ref}^{\alpha_\nu}}{A_{new}^{\alpha_A}\ \rho_{*new}^{\alpha_\rho}\ \nu_{*new}^{\alpha_\nu}} \tag{3.16}$$

here the subscript *ref* and *new* refer to the reference simulation and the new equilibrium state.

When in the new simulation the total internal energy calculated at $r/a = 1$ is found to monotonically depart from the initial value, either increasing or decreasing, a further simulation is run where the source power is corrected, slightly lowered, respectively increased, accordingly. The equilibrium condition is reached whenever the total internal energy on the system remains constant $W(r/a = 1, t) = const$, blue triangles in figure 3.3-left. The equilibrium state is also verified locally with the pressure profile (Figure 3.3). Therefore simulations are compared also by checking that the set of profiles, and in particular that of the ion temperature, only exhibits a weak departure from the initial set .

Finally we test the influence of the resolution by varying the numerical control parameter such as the time step and the number of points in $\theta-$direction. In most of the cases it tends to show that a coarse discretization leads to overestimate the value of the confinement time -turbulent transport is less effective at low resolution. The best simulation in terms of equilibrium state and numerical resolution is retained to build the scaling law.

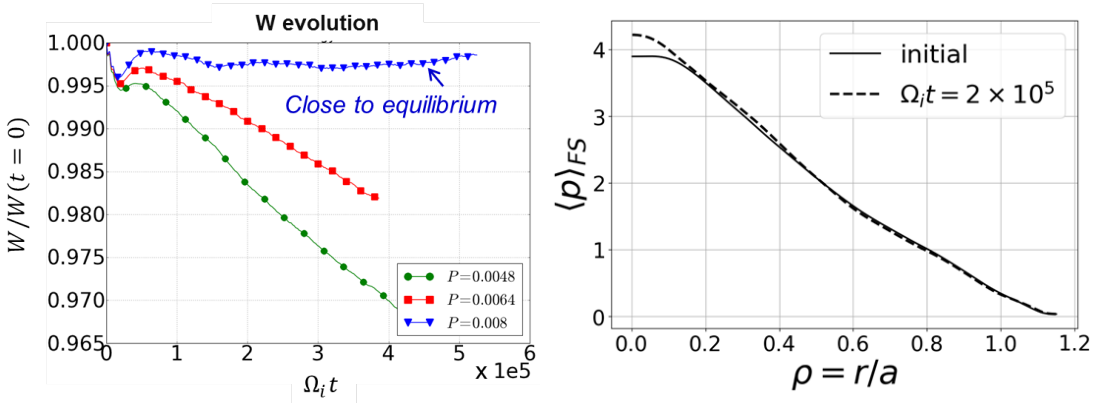

Figure 3.3: *left*− Procedure of heat source adjustment to reach steady state. *right*− The pressure profile remains constant during the entire duration of the simulation.

3.2.2 The scaling law is used to find steady states

In a first stage, the parameters are scanned one by one. We initially perform the scan on the following parameter range. For the aspect ratio, we scan the values $A = [3.2, 4.4, 6]$, which extend from the usual values of existent machines $2.5 - 3.5$ up to the high aspect ratio values for machines such as WEST with $A = 5 - 6$. The collisionality is scanned with three values $\nu_* = [0.004, 0.02, 0.1]$. The reference value of collisionality $\nu_* = 0.02$ is

used when varying the other parameters. The scan of ρ_* is performed with two different values of the aspect ratio: for $A = 4.4$ we scan $1/\rho_* = [150, 190, 250, 380]$, for $A = 6$ the three points $1/\rho_* = [190, 250, 380]$. One can notice at once that the range of values for the aspect ratio is rather reduced, less than a factor two, comparable to that for ρ_*. Conversely, the range of values for ν_* varies by a factor 25. This set of values already indicates that the most significant sensitivity of the confinement time has been obtained on A and ρ_*, with a reduced impact of ν_*.

The values of A, ν_* and ρ_* determine three of the five free normalization constants. Indeed, when the charge and mass are chosen, the gyrokinetic system solved by the GYSELA code depends the minor and major radius a and R_0, as well as on the normalization of the magnetic field B_0, of the density n_0 and temperature T_0. Setting a value for the aspect ratio A allows one to define the major radius from a. Then setting ρ_* and nu_* constrains the parameters n_0, T_0, B_0 and a. Similarity properties indicate therefore that each simulation represents a set of experiments where two engineering parameters can be varied. In this framework, one can have in mind that the collisionality is used to determine n_0 while ρ_* determines a, hence the fact that ρ_* is termed "effective" plasma size. The remaining "free" parameters are then T_0 and B_0. However, the actual similarity properties are not as stiff. Setting ρ_* enforces that $\sqrt{T_0}/(a\ B_0)$ is constant, which defines a $3D$ surface in the $4D$ parameter space, while setting ν_* yields that $n_0 a/T_0^2$ is constant, defining another $3D$ surface in the $4D$ parameter space. The intersection of these two $3D$ surfaces defines the actual $2D$ parameter space described by a given simulation.

An initial estimation of the scaling law has been made to set the value of the power source P. For the aspect ratio we have assumed $\alpha_A = 1$, which results by assuming the confinement time to be proportional to the parallel connection time $\Omega_i \tau_\parallel = qA\rho_*^{-1}$. The collisionality scaling has been assumed on the basis of the experimental results of [43] in which plasma discharges in JET and DIII-D Tokamaks are compared on the same plasma profiles. We have assumed $\alpha_\nu = -0.14$. Concerning the plasma size we have assumed a Gyro-Bohm scaling $\alpha_\rho = -3$, which is also that observed in reference [43]. The reference simulation was chosen in the GYSELA data base and corresponds to a simulation with a long run such that a steady state was reached. The above guide line was then used to generate new simulations, leading to a trial and error process, leading step by step to corrected exponents for the scaling laws. This procedure of approaching the steady state condition has been applied on these initial simulations as described in Section 3.2.1. Only the simulations closest to steady state are used to define the scaling.

A good alignment of the points $(1 \pm \epsilon)\Omega_i \tau_E$ is obtained for all the scans (figures 3.4 and 3.5). A power law of the energy confinement time has been extracted depending on each of the three parameters, one at a time (Black dots and dashed line in figures 3.4 and 3.5). When scaling one single parameter the linear regression procedure allows for an evaluation of the error on the exponents $\alpha_A, \alpha_\rho, \alpha_\nu$ and on the coefficient $log(C)$ (see Appendix B). The exponent resulting from this first scaling are:

$$\begin{aligned}
\alpha_A &= \ \ 0.67 \pm 0.26 & log(C_A) &= 13.81 \pm 0.39 \\
\alpha_\nu &= -0.13 \pm 0.05 & log(C_\nu) &= 14.36 \pm 0.19 \\
\alpha_{\rho,A=4.4} &= -2.50 \pm 0.21 & log(C_{\rho,4.4}) &= 1.86 \pm 1.09 \\
\alpha_{\rho,A=6} &= -2.81 \pm 0.36 & log(C\rho,6) &= 0.269 \pm 1.97
\end{aligned} \tag{3.17}$$

At this stage of the analysis, the values of the coefficients $log(C)$ are not of primary interest

to determine the transport scaling properties, since they include the dependence on the other parameters. They are anyhow reported in 3.17 for completeness. The resulting exponent for the aspect ratio scaling is a bit lower than the initial guess, conversely the collisionality exponent matches the initial guess. The error-bars of the two ρ_* scaling stand in the range between the so-called Bohm scaling $\alpha_\rho = -2$ and Gyro-Bohm one $\alpha_\rho = -3$.

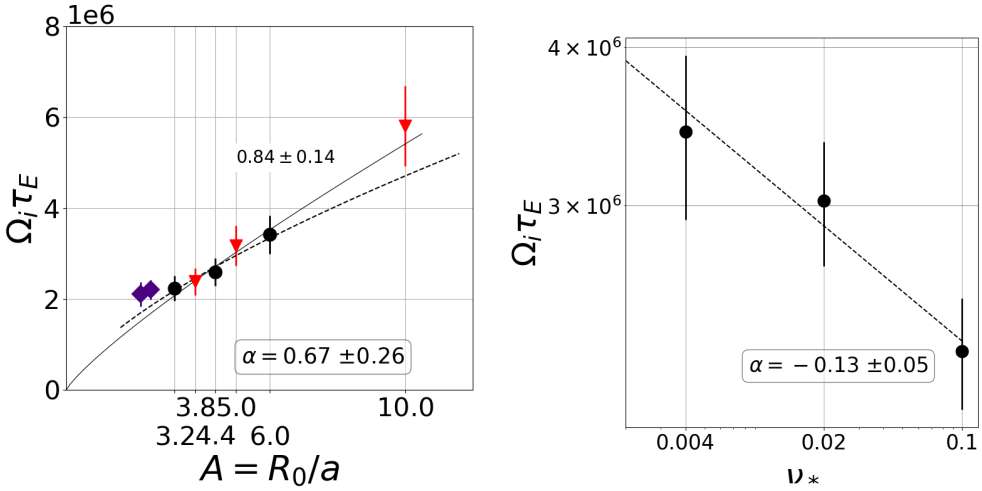

Figure 3.4: *left*− Aspect ratio scaling on linear-linear axis, the black dots and the dashed line are the result of the first scaling with exponent $\alpha_A = 0.67 \pm 0.26$ as indicated in the box, the red triangles are new steady state simulations obtained on the first scaling law. Other parameters used in the simulations are $1/\rho_* = 190$ and $\nu_* = 0.02$. The violet diamond correspond to a simulation with low aspect ratio $A = 2.2$. *right*− Collisionality scaling on double log axis, the exponent is $\alpha_\nu = -0.13 \pm 0.05$ is indicated in the box. Other simulation parameters are $A = 4.4$, $1/\rho_* = 190$

The set of exponents (3.17) can be used to run new steady state simulations. Given $1/\rho_* = 190$, $\nu_* = 0.02$ on the one hand, and $\alpha_A = 0.67$ on the other hand, the source amplitude has been scaled from the reference simulation $A = 3.2$, to cases with aspect ratio values $A = [3.8, 5, 10]$. Similarly, given $A = 6$, $\nu_* = 0.02$, and $\alpha_\rho = -2.81$ the source amplitude has been scaled starting from the reference case $1/\rho_* = 190$, to the values $1/\rho_* = [150, 310]$. The new points have been chosen in order to either interpolate the scaling, yielding a new point between the original points, or to extrapolate the scaling outside the initial parameter range. The new simulations (red triangles in figure 3.4 and figure 3.5) monotonically depart from the equilibrium state. However, the internal energy at $r/a = 1$ varies by less than one percent during the total simulation time ($2 \cdot 10^5 \Omega_i^{-1}$). We thus consider the new simulations to be close enough to equilibrium to be included in the data base used to determine the scaling laws. For both the aspect ratio and plasma size scaling, the interpolation points within the initial range are aligned with the scaling. Regarding the extrapolation cases to $A = 10$ and $1/\rho_* = 150$, the prediction of the initial (dashed line) scaling underestimate the achieved confinement time. Possible reasons will be discussed in the next Section. Adding the three new points to the aspect ratio scaling, one finds the exponent $\alpha_A = 0.84 \pm 0.14$, closer to the initial guess $\alpha_A = 1$, the error-bar overlapping with that of the previously determined α_A in the range $(0.7, 0.93)$.

The collected simulations in the data-base used to obtain the above results have also

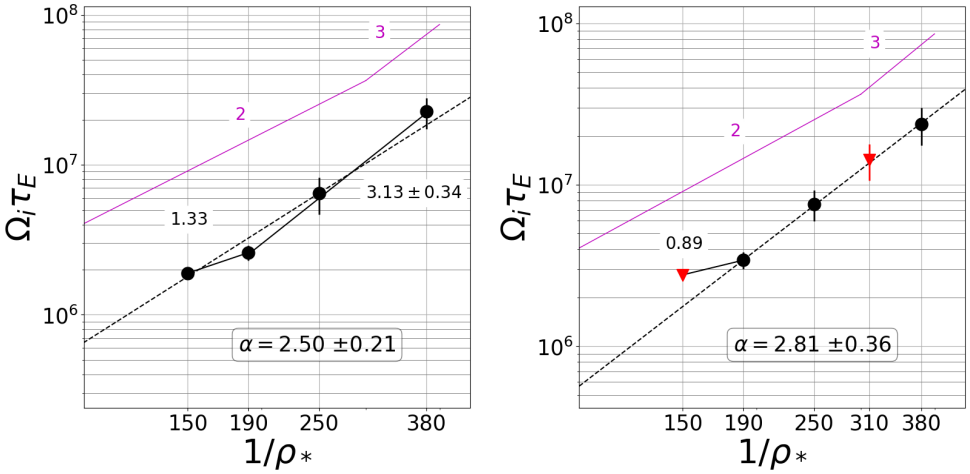

Figure 3.5: Plasma effective size scaling in double log scale for *left*− $A = 4.4$ and *right*− $A = 6$. The black dots and dashed line are the results of the first scaling law, with exponents $\alpha_\rho = 2.50 \pm 0.21$ and $\alpha_\rho = 2.81 \pm 0.36$ indicated in the boxes. The red triangle are the new steady state simulations run considering $\alpha_\rho = -2.7$. The magenta solid line indicates the slopes of the Bohm and Gyro-Bohm scaling laws. The two different slopes interpolating the points for $1/\rho_* < 190$ and for $1/\rho_* > 190$ are shown on the figures.

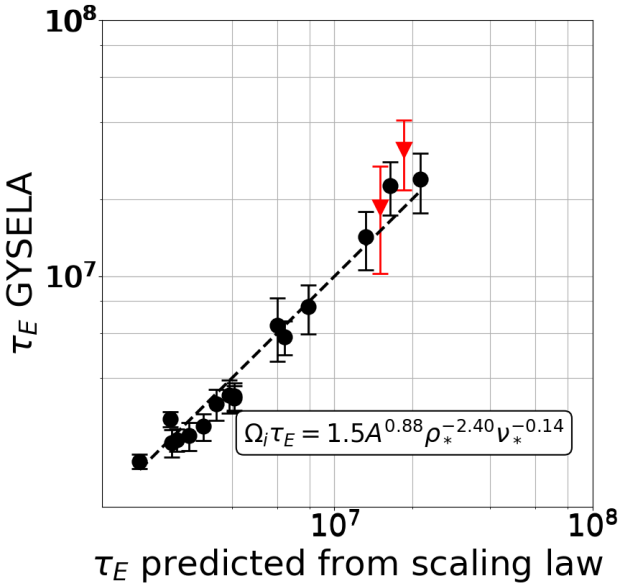

Figure 3.6: Multi-parameter scaling, black dots are all the simulations collected in all the single parameter scans, red triangles are the two new simulations for which two parameters are varied at the same time.

been analyzed in terms of a multi-parameter scaling (figure 3.6) then following a procedure comparable to that used for the empirical multi-machine scaling. The resulting exponents are within the error-bars of the single parameter scaling exponents, namely $\alpha_A = 0.88, \alpha_\rho = -2.4, \alpha_\nu = -0.14$. Using this multiple-parameter scaling, two more simulations have been run starting from the case $A = 6, 1/\rho_* = 190, \nu_* = 0.02$ and changing both A and ρ_*. The two new simulations are run on the parameters $A = 3.2$, $1/\rho_* = 450$ and $A = 5$, $1/\rho_* = 350$, they are found close to steady state and their confinement time stands therefore close to the multi-parameter scaling prediction.

3.2.3 Interpretation of the scaling law exponents

The choice of the basis function upon which the collection of points is fitted is arbitrary[11]. A power law of the form 3.12 has been chosen historically to interpret the empirical data on the confinement time. Possible motivations could be the simplicity of the function and the resemblance with scalability properties in other fields of research, such as in the fluid mechanics. In this paragraph we discuss then theoretical basis and validity of a power law as the basis function for the three dimensionless dependencies of the energy confinement time. Indeed, an implicit, but usually quite significant and important aspects when addressing physical laws, expressing the variation of a physical quantity in terms of a control parameter, is the status given to the point $(0, 0)$, the origin of the graph. In most cases, a linear dependence is considered so that the physical law is consistent with the $(0, 0)$ point. The latter can then be regarded as belonging to the physical law with no error bars. For a scaling law expressed in terms of a power law, the above remark is crucial when discussing the sign of the exponent. For example, when the effective size of the plasma is vanishing, $1/\rho_* \to 0^+$, one can expect the confinement time to be also vanishing $\tau_E \to 0^+$, the power law must then lead to $\alpha_A \rho < 0$. However, with determining the scaling law exponent in a log-log framework, the $(0, 0)$ point is sent to minus infinity, and the fact that this point is assumed to be known with no uncertainty has no impact on the result. Given the effort involved to obtain each data point and to estimate and reduce the error bars, such a flaw in the procedure can be regarded as a critical point that requires being fully addressed.

Aspect ratio dependence

A possible issue with the choice of a power law as the basis function for the plasma confinement similarity properties can readily be addressed regarding the aspect ratio parameter. By definition the aspect ratio is the ratio between the major and minor radius of the torus and is thus greater than one. A power law of the confinement time with $\alpha_A > 0$ implicitly assumes that confinement vanishes at $A = 0$. However,since $A = R_0/a > 1$, the point $A = 0$ does not exist. The origin cannot be used to constrain the scaling law. Conversely, for $\alpha_A < 0$ the point $1/A \to 0+$ must be discussed. In the GYSELA simulations, both the initial guess of the energy confinement time scaling like the parallel connection time $\Omega_i \tau_\parallel \propto qA\rho_*^{-1}$ and the obtained data are consistent with the confinement time increasing with the aspect ratio, similar to the former case $\alpha_A > 0$.

The power law function can then be considered to be an approximation of an exact similarity property that only holds in a particular range of values of the control parameter. This is clearly a weaker result than a power law fitting the full range of interest. To further address this point, we have run two cases with aspect ratio smaller than 3.2, namely

$A = 2.5$ and $A = 2.2$. Reaching the same steady state condition as described in Section 3.2.1 for the low aspect ratio cases has proven more challenging: the total internal energy does not depart monotonically from the equilibrium condition, but exhibits oscillations around the initial value. Furthermore, the confinement enhancement in the plasma center becomes large and governs a clear increase of the core temperature profile. Despite these shortfalls with respect to the chosen steady state criteria, we have reported on figure 3.4 two simulations with low aspect ratio, retaining those for which the amplitude of the internal energy oscillations remains within 1% of the initial value during the simulation time. The points lay above the scaling, suggesting a smaller value of the exponent α_A, this trend is opposite to the high aspect ratio extrapolation to $A = 10$ that supports an increase in the exponent α_A. Other simulations at low aspect ratio, also departing from steady state, appear to support an increase of the confinement time as A is reduced below 3. One may not exclude the possibility that the slope of the energy confinement time dependence on the aspect ratio could change sign, with a minimum around $A \sim 3$. To support this idea we recall that in the reference empirical scaling for H-mode discharges (Equation 3.1) the energy confinement time is found to depend on the inverse of the aspect ratio $\Omega_i \tau_E \propto A^{-0.73}$, while the more recent analysis [40] starting from a subset of the same experimental data base, indicates that the data can be consistent with a dependence of the form $\Omega_i \tau_E \propto A^{1.1}$. The database of experimental data is biased towards the small aspect ratio range typically $2 < A < 3.5$. One can thus argue, in agreement with the GYSELA data, that a change in dependence can occur around $A \approx 3$, separating a large aspect ration behavior where confinement increases with A from the low aspect ratio branch where confinement could also increases but with $1/A$. In terms of physics, increasing the aspect ratio tends to reduce the curvature and grad-B drifts, which are the generic drive for turbulence in magnetic confinement. Insight into the mechanism that could drive a reversal of the trend at small aspect ratio would help investigating this limit. It is to be underlined that for the GYSELA simulations, at given profiles of the ion pressure and of the safety factor, the magnetic shear is unchanged while the balance of plasma rotation in the poloidal and toroidal direction can be sensitive to the aspect ratio.

Collisionality dependence

Concerning collisionality, the negative dependence of the energy confinement time could be explained by two theoretical arguments. *(i)* An increased collisionality would increase the collisional transport, hence reducing confinement. *(ii)* The plasma collisionality is known to enhance the ion turbulent transport by damping the zonal flows, non-linearly generated by turbulence [26, 28]. These mechanisms are consistent with the trend observed in the GYSELA simulations and supporting the asymptotic behavior $\tau_E \to 0+$ for $1/\nu_* \to 0+$. Conversely, the plasma collisionality is also known to prevent the formation of turbulent modes generated by the trapped electrons (TEM) because of electron collisional detrapping [44]. This physics is not included in the GYSELA model used for the present simulations since all electrons are assumed to exhibit an adiabatic response. However, based of these considerations, one cannot theoretically exclude that at large collisionality some form of turbulent stabilization occurs driving a non monotonic behavior. This physics is usually considered to be the explanation for the so-called Alcator scaling, a regime such that the confinement time increases with plasma density, hence as ν_* increases, consequently with $\alpha_\nu > 0$. The monotonic behavior reported for the ν_* scaling with GYSELA could be specific of the low collisionality regime, with possibly a reversal

of the trend at high collisionality, when Trapped Electron Modes can be stabilized by collisionality, prior to the large collisionality regime where collisional transport prevails and the above argument leading to $\alpha_\nu < 0$ should hold.

Plasma effective size dependence

The most relevant dependence of the energy confinement time resulting from the GYSELA scaling corresponds as expected to the plasma effective size parameter ρ_* with a power close to 3. A simple model to describe the confinement time is to consider a homogeneous transport model. We shall consider here two cases: a diffusive model with diffusion coefficient D and a ballistic model with transport coefficient V. We then assume that these transport coefficients are determined by a local step for the ion radial transport λ_c and a local time scale τ_c so that $D = \lambda_c^2/\tau_c$ and $V = \lambda_c/\tau_c$. The confinement time is then the global characteristic time of heat transport on the scale a, the minor radius, given the transport process governed by the local properties. Hence for the two proposed mechanisms:

$$\Omega_i \tau_E^D = \Omega_i \frac{a^2}{D} = \frac{a^2}{\lambda_c^2} \Omega_i \tau_c \tag{3.18a}$$

$$\Omega_i \tau_E^V = \Omega_i \frac{a}{V} = \frac{a}{\lambda_c} \Omega_i \tau_c \tag{3.18b}$$

In the experimental observation of turbulence as well as in the simulation work one has found that the ion Larmor radius ρ_i is a key scale. To take this information into account we thus introduce $\lambda_c = \rho_i F_\lambda$. A common expression for the confinement time can then be written:

$$\Omega_i \tau_E = \frac{1}{\rho_*^n F_\lambda^n} \Omega_i \tau_c \tag{3.19a}$$

with $n = 2$ for diffusive transport and $n = 1$ for ballistic transport. Regarding the characteristic time, we have introduced two typical times, the parallel connection time $\tau_\parallel \propto q\ A\ a/v_{th}$ and the interchange growth rate γ, for a case well above the threshold, such that $1/\gamma \propto \sqrt{A}\ a/v_{th}$. One can then consider a dependence of τ_c of the form $\Omega_i \tau_c = q\ A^m\ F_\tau/\rho_*$, with $m = 1$, respectively $m = 1/2$ when considering that the local mechanism is governed by the parallel time scale or the interchange growth rate. The scaling law for the energy confinement time can then be written as:

$$\Omega_i \tau_E = \frac{1}{\rho_*^{n+1}} \frac{q A^m F_\tau}{F_\lambda^n} \tag{3.19b}$$

Assuming that the two dimensionless functions F_λ and F_τ exhibit no dependence on ρ_*, one then finds that $\alpha_\rho = -(n+1)$. The so-called gyro-Bohm regime $\alpha_\rho = -3$ would then correspond to diffusive transport, while the Bohm transport regime $\alpha_\rho = -2$ would correspond to ballistic transport. Comparing expression (3.19b) to the proposed scaling (3.17), one finds that the global behavior suggest that the relevant time scale stands between the interchange and the parallel characteristic times, while the length scale points towards a transport process between ballistic and diffusive, also referred to as super-diffusive in the literature. A means to introduce such strange transport behavior is to allow the exponent n in the expression (3.19b) to take arbitrary values between 1 and

2 reflecting transport processes that behave between Levi flights, our ballistic transport limit, and diffusion. The alternative is to assume that the characteristic transport scale also depends on the global scale a, hence $F_\lambda \propto \rho_*^{\eta-1}$, leading to an increase with ρ_i for $\eta > 0$ as well as an increase with a for $\eta < 1$, which is unfavorable regarding confinement performance, conversely a decrease with a for $\eta > 1$, which is favorable for confinement performance. Let us now define $\lambda_* = \lambda/a$, so that $\lambda_* \propto \rho_*^\eta F_\lambda$ so that the generalized expression of the confinement time is of the form:

$$\Omega_i \tau_E = \frac{1}{\rho_*^{n\eta+1}} \frac{q A^m F_\tau}{F_\lambda^n} \tag{3.20a}$$

The power law dependence is therefore such that:

$$\alpha_\rho = -\big(n\eta + 1\big) \tag{3.20b}$$

Allowing for two free parameters, with a single constraint, only specifies the relationship

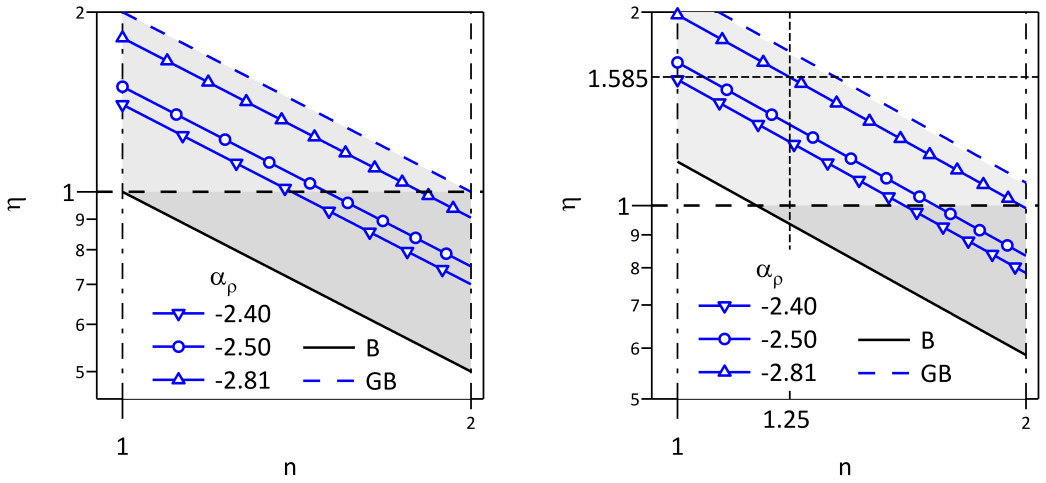

Figure 3.7: Phase portrait of the transport properties. The index n characterizes the transport law, $n = 1$ corresponds to ballistic transport and $n = 2$ to diffusion. The index η takes into account the impact of the global scale on the turbulence characteristic scale, $0 < \eta < 1$, $\eta = 1$ is the limit with no impact of the global scale. The shadowed regions corresponds scaling laws lying between Bohm (B) and gyro-Bohm (GB) scaling. For $\eta < 1$ the correlation length increases with device size, darker gray, while for $\eta > 1$ the correlation length decreases with device size, lighter gray. *Left* Lines of constant scaling law exponent α_ρ are determined by the relation $n\ \eta = -1 - \alpha_\rho$. *Right* Lines of constant scaling law exponent α_ρ are determined by the relation $n\ \eta = -0.83 - \alpha_\rho$.

(3.20b) between n ans η. Given the constraint $-3 < \alpha_\rho < -2$ the exponents η and n must therefore verify $1 < n\eta < 2$. When $|\alpha_\rho| \to 3^-$, the range of possible values of n converges towards 2 while η converges towards 1. Consequently, in the gyro-Bohm limit, when one constrains $\eta < 1$, only diffusive transport with no impact of the global scale on the turbulence characteristic scale is possible ($\eta = 1$), figure 3.7 Light Hand Side. The previous discussion is based on the assumption that $\Omega_i \tau_c$ scales like ρ_*^{-1} which translates into the "1" contribution of equation (3.20b). Should $\Omega_i \tau_c$ scale differently would lead to a shift of the curve $\alpha_\rho = constant$, as on figure 3.7 Right Hand Side where $\Omega_i \tau_c \propto \rho_*^{-0.83}$

is considered. One can notice that in this case, when assuming $\eta \leq 1$, the ρ_* scaling law for $A = 6$ becomes marginal ant requires both diffusive transport, $n \to 2$, with no dependence of the turbulence characteristic scale λ on the global scale a, $\eta \to 1^-$. The weaker the dependence of $\Omega_i \tau_c$ on ρ_*, the more one can expect transport to depart from the gyro-Bohm limit. The constraint $\eta \leq 1$ that we have addressed, dark gray region in figure 3.7, narrows the parameter space. Conversely allowing for a stabilizing effect of the global scale a, $\eta \geq 1$, light gray region in figure 3.7, provides a renewed perspective to address the transport properties.

When considering a vanishing plasma volume, $a \to 0$, the confinement time should vanish $\tau_E \to 0$, hence a power law with $\alpha_\rho < 0$ is a suitable basis function to interpret the ρ_* dependence of the energy confinement time. However, in previously published results of numerical simulations [45, 46, 47] the scaling law of the effective local diffusion coefficient is observed to change slope with ρ_*. A transition from Bohm, exponent -2, to Gyro-Bohm, exponent -3, scaling is reported for $1/\rho_* > 300$. Regarding the GYSELA confinement time scaling with the plasma effective size (figure 3.5), one can question the existence of two different regimes, with a possible transition at $1/\rho_* = 190$. Indeed, one finds that the first slope from $1/\rho_* = 150$ to $1/\rho_* = 190$ is close to 1, smaller than the Bohm scaling. Conversely, for $1/\rho_* \geq 190$ a regime closer to the Gyro-Bohm behavior, is readily observed. The eventual change in behavior reported here is not as clear as in previous GYSELA simulations [47]. In particular, the possible transition does not seem to occur at the same value of ρ_*. One possible reason for this change in behavior is the fact that the present global simulations is different from the annulus geometry used in [47], this setting being closer to a flux-tube setting that is mostly used when addressing the ρ_* dependence of confinement. Further analysis and simulations are still needed to address this issue.

Multi-parameter scaling, parameter interplay and summary

When considering the multi-parameter scaling, the points appear to be better aligned according to the scaling law. This can be governed by hidden compensation effects between the departures from the power -law scaling for each control parameter. The multi-parameter scaling then appears to be rather appropriate, while the single parameter scaling gives evidence that a scaling law behavior can be misleading.

The scaling laws that have been determined prove to be effective when looking for a new steady states obtained when changing the control parameters. However, it is unclear that the power law behavior that has been recovered does hold with precision for the whole range of interest of the different control parameters. It is quite possible that scaling laws with the accuracy required for the design of reactors are out of reach because the power law form is a too crude assumption.

3.3 Similarity properties at global and micro scales: breaking the paradigm

Dependence on ρ_*

In this Section we address the comparison between global and local scaling laws for the energy confinement time. In the local point of view, the energy confinement time is given by the previously computed expression (3.20a).

We compute the local correlation functions for the time and spatial evolution of the electric potential fluctuations $\tilde{\phi}$ with the following expressions:

$$C(t_{lag}) = \frac{\langle \tilde{\phi}(t)\tilde{\phi}(t+t_{lag})\rangle_{\delta t}}{\sqrt{\langle \tilde{\phi}(t)^2\rangle_{\delta t}\langle \tilde{\phi}(t+t_{lag})^2\rangle_{\delta t}}}; \qquad C(r_{lag}) = \frac{\langle \tilde{\phi}(r,t)\tilde{\phi}(r+r_{lag},t)\rangle_{\delta t}}{\sqrt{\langle \tilde{\phi}(r,t)^2\rangle_{\delta t}\langle \tilde{\phi}(r+r_{lag},t)^2\rangle_{\delta t}}} \quad (3.21)$$

The terms in angle brackets in equation (3.21) are averaged over a time interval $\delta t = 5 \times 10^3 \Omega_i^{-1}$. $\tilde{\phi}$ corresponds to the fluctuations of the electric potential with respect to its time average over the considered time interval δt. To compute the correlation functions a poloidal cut of the electric potential fluctuations resulting from GYSELA simulations at an arbitrary toroidal location has been used. The correlation time and the radial correlation length correspond to the values r_{lag} and t_{lag} for which $C(r_{lag}) = 0.5$ and $C(t_{lag}) = 0.5$.

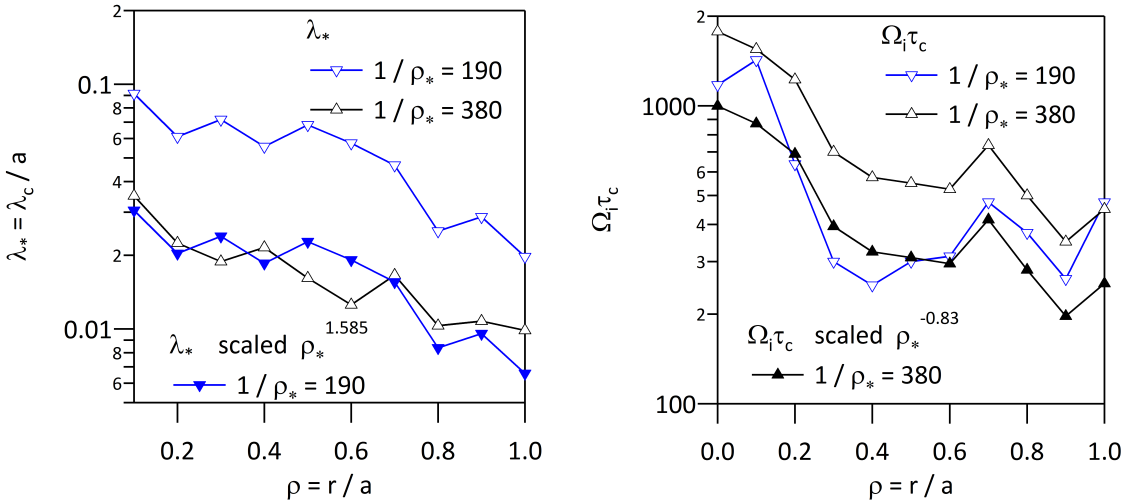

Figure 3.8: *Left*: Profile of the correlation length $\lambda_* = \lambda_c/a$ for $A = 6$ and two values of ρ_*, $\rho_* = 1/190$ blue curve head down open triangles, and $\rho_* = 1/380$ black curve head up open triangles. It is possible to match the two curves by scaling down the $\rho_* = 1/190$ data provided the correlation length is considered to scale as $\lambda_* \propto \rho_*^{1.585}$, blue curve, closed head down triangles. *Right* Correlation time $\Omega_i\tau_c$ profile for the same set of simulations. The correlation time for $\rho_* = 1/380$ (black curve head up open triangles) is scaled down to the profile for $\rho_* = 1/190$ (blue curve, head down open triangles) assuming that $\Omega_i\tau_c \propto \rho_*^{-0.83}$, black curve, head up closed triangles.

We find that the radial correlation length scales as the local ion Larmor radius but with a power 1.585 (Figure 3.8, left hand side), hence a stronger dependence than found

in [32], where $\lambda_c \propto \rho_i$ is reported. Two reasons could explain the difference, first the chosen aspect ratio, $A = 6$ here and $A \approx 3$ in [32], second the data plotted on Figure 3.8 is that at the midplane while that in [32] is averaged poloidally.

Regarding the data for the confinement time τ_c, Figure 3.8 right hand side, one finds that the profiles for the two values of ρ_* match approximately with the scaling $\Omega_i \tau_c \propto \rho_*^{-0.83}$. This is less than the expected scaling in $1/\rho_*$ and corresponds to the plot on Figure (3.7) right hand side. Regarding this plot, the scaling of the correlation length determines $\eta = 1.585$, so that given $\alpha_\rho = 2.81$, one finds that the exponent characterizing the transport "strangeness" $n = 1.25$, as indicated on Figure 3.8 right hand side. The local analysis indicates therefore that the transport is close to ballistic ($n = 1$), which is expected since avalanche transport is observed in the GYSELA simulations (as well as with other global code, ORB5, GT5D), but that the global scale a has a rather strong effect in reducing the correlation length $\eta = 1.585 > 1$, hence improving confinement performance. The unfavorable trend of ballistic transport thus seems to be balanced by the correlation length decrease with increasing plasma minor radius a, the global scale, so that transport at aspect ratio $A = 6$ exhibits a confinement time scaling close to gyro-Bohm.

We find therefore that the ρ_* dependence the present analysis yields a consistent picture between the local dependence, that of λ_* and $\Omega_i \tau_c$, and the global dependence, that of τ_E. However, it is to be underlined that the number of constraints is the same as the number of unknowns so that a match is a priori always possible. In fact the consistency holds mostly because the obtained values agree with the turbulence physics that are observed in the simulations.

Dependence on A

The aspect ratio has been found to be the second most important parameter after ρ_*. We analyze therefore the correlation length and correlation time dependence on A. A striking result on Figure 3.9 left hand side, is that the correlation time does not exhibit any dependence on aspect ratio A. Similarly, but perhaps not as clearly, on finds that the correlation length does not exhibit a marked dependence on A. An important result that emerges from this evidence is that the local turbulence properties cannot account for the dependence of the energy confinement time on the aspect ratio. This result can be understood in two ways: first, an equation of the form (3.20a) is not appropriate to describe the energy confinement time scaling and other features must be introduced in the model to bridge local and global properties. Second, it indicates that the global properties are not completely determined by the turbulent scale properties, and, therefore, that physical mechanisms at intermediate scales, the meso-scales, play a role and must be identified.

In the analysis of the dependence on the aspect ratio we have discussed this property in terms of the role of various characteristic times, the growth time well above the threshold $\Omega_i/\gamma_p \propto \rho_*/sqrtA$, or the parallel connection time $\Omega_i \tau_\parallel \propto \rho_*/A$. However, wen computing the actual growth rate, one finds that is in fact driven by a combination od these two time scales with $\gamma = \gamma_p - \sigma/\tau_\parallel$ since damping processes are found to be governed by parallel transport. Consequently one finds that Ω_i/γ is not a power law in terms of the aspect ratio, $\Omega_i/\gamma \propto \rho_*^{-1}(1/\sqrt{A} - \sigma_\parallel/A)^{-1}$. The latter equation implies that $A \geq A_\parallel$, which

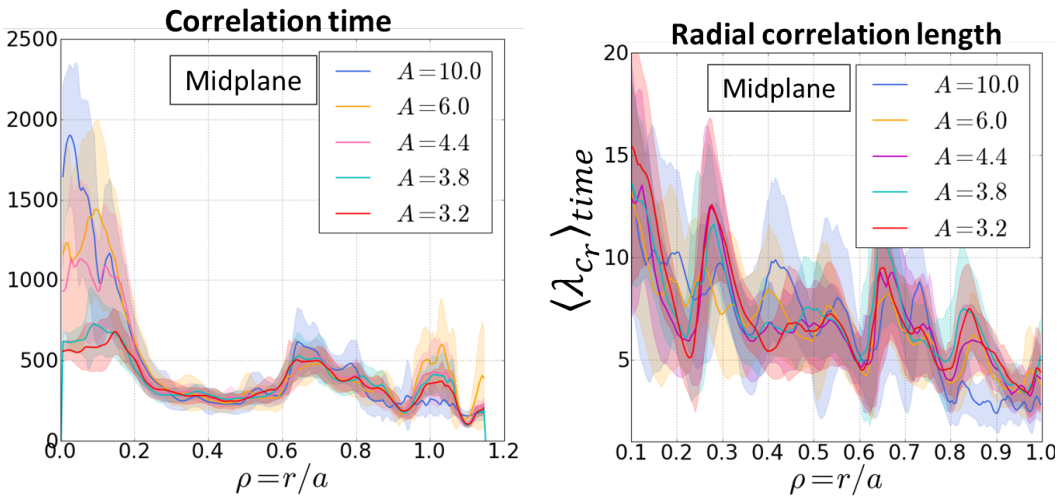

Figure 3.9: Radial profile of turbulence correlation time and length for aspect ratio and plasma size scaling. The curves are averaged in time, the standard deviation on the time evolution is in shadows, at the poloidal position $\theta = 0$. The time average is performed on a time window of $10^5\Omega_i^{-1}$. The scan in ρ_* is performed at aspect ratio $A = 6$

stems from $\gamma_p \geq \sigma/\tau_\parallel$, hence a regime with linearly unstable interchange turbulence. One thus obtains:

$$\frac{\Omega_i}{\gamma} \propto \frac{\sqrt{A}}{\rho_*} \frac{1}{1-\sqrt{A_\parallel/A}} = \frac{\sqrt{A_\parallel}}{\rho_*} \frac{A/A_\parallel}{\sqrt{A/A_\parallel}-1} \tag{3.22}$$

Assuming that $\Omega_i\tau_c \propto \Omega_i/\gamma$ one then obtains for $A \gg A_\parallel$: $\Omega_i\tau_c \propto \sqrt{A/A_\parallel}/\rho_*$, hence increases like $A^{1/2}$, while $\Omega_i\tau_c$ exhibits a minimum for $A = 4A_\parallel$. Although the actual scaling properties of such a model do not much quantitatively the scaling law for the confinement time, that qualitative behavior could give the appropriate understanding of the dependence on the aspect ratio.

3.4 Summary and discussion

A scaling law for the energy confinement time has been extracted from GYSELA global and flux-driven simulations of ion turbulent transport in the core plasma. The scaling law is recovered in function of the three parameter aspect ratio, plasma size and plasma collisionality, keeping all the other parameters constant between the simulations. The GYSELA scaling has proven efficient in predicting new equilibrium states of the numerical simulations. This result may indicate that similarity holds for the turbulent transport in the core of tokamak plasmas. The choice of a power law to interpret the dependence of the confinement time on the parameters has been questioned concerning the three parameters under investigation. The existence of the GYSELA scaling law sets the ground for comparison between different models: between local and global models, as a benchmark test between similar codes with different numerical scheme, between models accounting for the effect of different phenomena implemented such as electron turbulence, electromagnetic effects or boundary conditions.

The transport properties have been investigated in the local framework of the mixing length theory. When scaling the correlation time of turbulent fluctuations we do not

recover the same scaling as the energy confinement time with the aspect ratio and plasma size parameters. This result would suggest to question the accuracy of local models when describing the global evolution of the system through the confinement time parameter.

A further discussion pointed out by the results obtained in this chapter concerns the possibility to define a uniform transport model on the entire plasma volume. In section 3.1 it has been shown that the definition of a unique diffusion coefficient can interpret the radial shape of the fully coarse grained energy confinement time resulting from GYSELA steady state simulations. However this property is lost when reducing the coarse graining, that is when including the detailed time evolution of the system governed by turbulence. Also, the definition of a transport coefficient in terms of the correlation length and time of turbulence does not lead to a constant and uniform result over the plasma volume.

Several assumptions of the GYSELA model used in this work could limit the direct comparison with the experiments. The first concerns the adiabatic electrons limit. In our simulations only the ion temperature gradient turbulence is modeled. However it has been shown in local gyrokinetic simulations that electron driven modes could affect the transport properties [48]. However the trapped electron mode is stabilized at high collisionality so that the GYSELA scaling results anyhow appropriate at high collisionality regime.

In the electrostatic limit, hence without driving the electromagnetic effects that depends on the plasma β it is not relevant to address β scaling. Concerning this argument the experimental work of [43], comparable to our work since it compares the plasma shots with the same local profiles, finds no β dependence of the energy confinement time. This result has been confirmed by a more recent work [40]. However the discussion is not closed and the β dependence should also be addressed with GYSELA simulations. To test this dependence, a new scaling law could be build on a different value of the internal energy content by modifying the initial profiles. The main difficulty would be represented by the seek of the reference equilibrium state for the new profiles. One could begin this study by investigating the effect of a different initial pressure profile which leads to the same internal energy content. This would bring insight into the role of profile corrugations on the global transport regime.

The last limitation of this study concerns the boundary conditions. Those used here are a simplification that tends to reduce turbulence. It has been observed in experiments[10] that under some conditions, the spontaneous formation of a transport barrier at the interface between confined and open field lines region of the plasma leads to an improved confinement regime, the H-mode. Typically, the transport in H-mode discharges exhibits a gyro-Bohm like scaling with the plasma size similar to the one recovered in GYSELA for $1/\rho_* > 190$. However the simulation profiles are not characterized by a pedestal in the vicinity of $r/a = 1$ and the turbulent regime is extended all over the poloidal section. The behavior of the scaling in presence of more realistic boundary conditions remains to be tested.

Chapter 4

GYSELA with an immersed boundary limiter: the effect of a poloidally localized cold spot

The tokamak magnetic configuration aims at confining plasma in a toroidal volume. However, Some form of transfer, hence effective interaction from the plasma to the wall is both unavoidable and necessary for steady state operation. This exchange can be mediated by non-charged particles, neutrons if fusion reaction s are considered, photons or neutral atoms and molecules. However, in the present work dedicated to heat transport we address actual plasma-wall interaction. Two main configurations are mostly used to organize this interaction: limiter and axisymmetric divertor. A major challenge for such components is the heat transfer out of the plasma. In such configurations the plasma volume is usually divided into two regions: the confined core, where magnetic field lines are closed in the plasma volume and is also called "closed field lines" region and the external Scrape-Off Layer (SOL), where magnetic field lines intersect the machine wall, alternatively "open field lines" region. There, transport towards the wall can occur in the direction parallel to the magnetic field lines and the heat is transferred to the wall component in the same direction. In the SOL, therefore, parallel and transverse transport compete and confinement is strongly reduced. In this chapter we implement a simplified version of the plasma-wall interaction physics in GYSELA, introducing a limiter shaped heat sink with a dedicated penalization technique. We verify that the poloidal asymmetry of the sink induces parallel transport in the SOL region by the parallel propagation of a cold front in the phase space. Regarding the particle transport, we describe how the cold limiter acts by a mechanism akin to condensation as a particle attractor both in the parallel and perpendicular directions.

4.1 Penalized limiter geometry for the heat sink

The presence of the wall in GYSELA is modeled with an immersed boundary technique. Many Immersed Boundary Models (IBM) have already been developed mainly in computational fluid dynamics [49]. These techniques allow to simulate flows within boundaries, where the shape of the boundary does not conform with the numerical grid of the code. In general, a forcing term is localized within the immersed boundary and modifies the physics simulated in that region. The implementation of an immersed boundary with

a penalization technique has also been explored in fluid codes for plasma turbulence to model the plasma-wall interaction [50, 51, 52].

4.1.1 GYSELA limiter configuration

We apply the penalization approach in GYSELA to implement a poloidally and toroidally symmetric first wall region together with a toroidally symmetric limiter which protrudes from the wall into the plasma chamber with a finite radial and poloidal extent. It is to be underlined that the choice of axisymmetric geometries is not governed by a limitation of the penalization technique but because it is consistent with a key symmetry of the tokamak configuration. It is also to be underlined that the chosen limiter has a finite poloidal extent so that transverse fluxes onto the limiter front face participate to the boundary conditions.

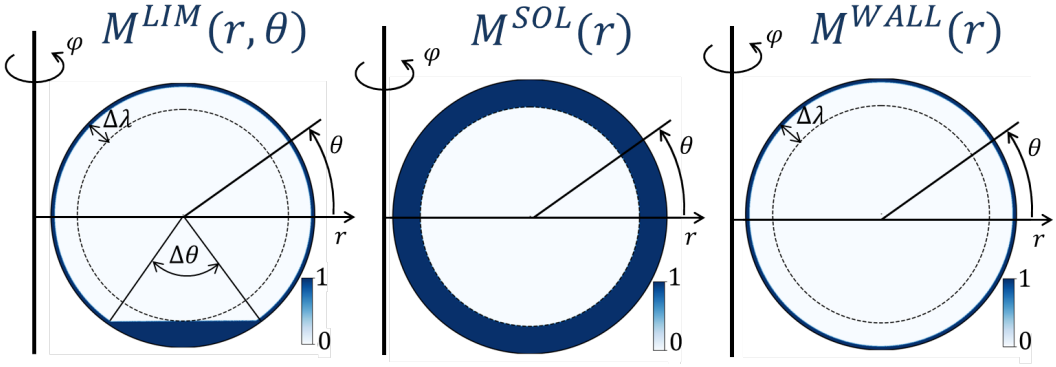

Figure 4.1: The three masks used in the penalization technique to define different regions of the numerical domain.

The different regions of the plasma chamber are defined using mask functions. These select particular regions of the numerical domain. The mask function can take values between 0, for a location outside the chosen region, and 1, for a location inside the chosen region. This technique is versatile: many different geometries of the boundary can be implemented by simply changing the shape of the mask, while the magnetic configuration remains unchanged. In the present work with GYSELA we combine three different mask functions, shown on figure 4.1. The geometrical configuration of the immersed boundary is essentially defined by the mask $M^{LIM}(r,\theta)$ in the poloidal plane, where the shape of both the first wall and the axisymmetric limiter is drawn, resembling the geometry of Tore Supra [53]. The last closed flux surface, or *separatrix*, is the magnetic surface tangent to the limiter. In this configuration, the impact angle of the magnetic field lines on the limiter and the connection length change with the radial location in the SOL, since the limiter surface is flat. This condition can easily be modified by changing the limiter shape. Also the poloidal position of the limiter and its extent are arbitrary chosen. The remaining two masks are defined only in the radial direction, $M^{SOL}(r)$ defines the whole region outside the separatrix and $M^{WALL}(r)$ the first wall region only. These three masks are combined to identify different physical regions in the numerical domain, summarized in table 4.1. From the technical point of view let us remark that the masks should only be added or subtracted when selecting the different regions in order to control this transition.

Physical regions	Combination of masks
Confined plasma	$1 - M^{SOL}$
Scrape-Off Layer plasma	$M^{SOL} - M^{LIM}$
All plasma	$1 - M^{LIM}$
Wall only	M^{WALL}
Limiter only	$M^{LIM} - M^{WALL}$

Table 4.1: Definition of the physical regions in the numerical domain of GYSELA with corresponding mask functions.

The transition between 0 to 1 of the mask functions is supposed to be as sharp as possible, while being continuous to avoid numerical issues with the discontinuity. In practice, we chose as transition function a hyperbolic tangent with finite stiffness. On Figure 4.2 are shown a radial and poloidal cut of the masks. Typically, the transition region covers $\sim 5\rho_i$ over at least 10 grid points. The smoothness of the transition region is particu-

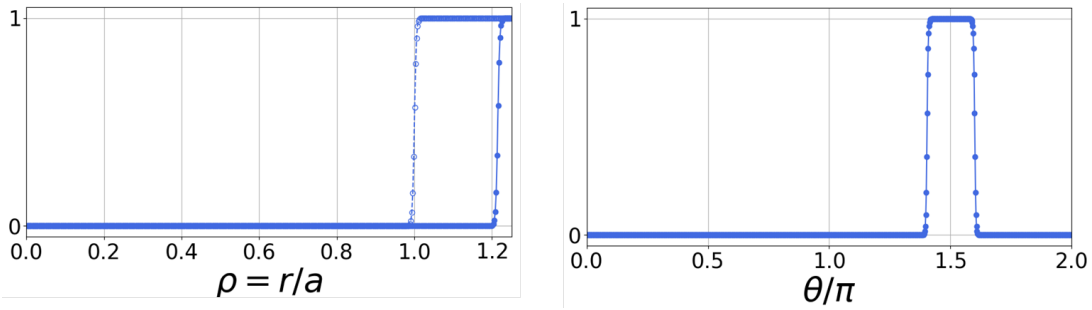

Figure 4.2: On the left the radial $M^{SOL}(r)$ with transition at $\rho = 1$, empty dots, and $M^{WALL}(r)$ with transition at $\rho = 1.2$. On the right a cut in poloidal direction of M^{LIM} at $\rho = 1.05$. The transition region from 0 to 1 spans over 10 grid points at least.

larly important with respect to the interpolation schemes that are used in the code, and the issue of oscillation generation is the vicinity of discontinuities. Such oscillations have been observed is some simulations. Cubic splines are the main interpolation scheme in GYSELA and these should not generate the so-called Runge oscillations by construction. The issue might be governed by Fourier filtering in the Poisson equation, in particular associated to the use the "aligned coordinates" option. Such filtering would then generate Gibbs oscillations, see Figure 4.3. The Gibbs oscillations depend on both on the number of points in the transition region and on the strength of the filtering. For the filtered data on Figure 4.3, the transition extends over five grid points and two thirds of the modes are filtered out to enhance the Gibbs oscillation phenomenon. The limiter boundary intersects by definition the field lines and introduce therefore a sharp gradient in the parallel direction. This aspect of the boundary is in conflict with the assumption that backs the use of aligned coordinates. From a broader perspective, at the plasma-limiter interface several assumptions that back our model are not fulfilled, quasi-neutrality, but also some aspects of the gyrokinetic ordering. A comprehensive investigation of the impact of these shortfalls will require a specific effort, most likely backed by a full f, two species, 6D kinetic code. In the present work, we only consider among these issues the signature in terms of Gibbs oscillations. Due to the chosen shape of the limiter in the GYSELA simulation that have been performed, the transition region is orthogonal to the z-direction.

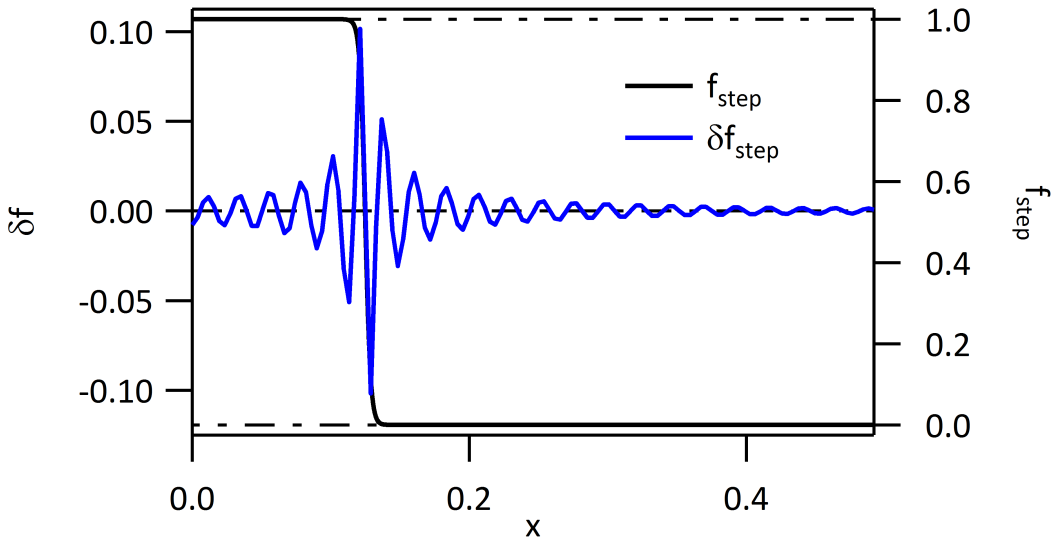

Figure 4.3: For a periodic and symmetric mask function f_{step} function of x,plain black line, right hand side axis, Fourier filtering generates the departure δf from the input function, plain blue curve and right hand side axis. These Gibbs oscillations governed by a sinus cardinal spectrum tend to propagate to the whole domain when the transition region is too narrow or the filtering too strong.

Let δN_z be the extent of the transition region in number of points, the extent in the poloidal direction is then typically $\delta N_\theta \sim N_\theta \delta N_z |\sin(\theta_L)|/(2\pi N_r)$. For $N_\theta = 2N_r$, this yields $\delta N_\theta \sim |\sin(\theta_L)|\delta N_z/\pi$. Here θ_L is the characteristic angle of the poloidal potion where the magnetic surface of interest intersects the transition layer, which depends on the chosen radius. One thus finds that $\delta N_\theta \leq \delta N_z/\pi$, hence with $\delta N_z = 10$. The transition layer will extend over at most 3 points for the resolution chosen in this example. Improving this matter requires that one increases the ratio N_θ/N_r or the ratio $\delta N_z/N_r$. To illustrate this issue we consider two simulations, one with "aligned coordinates" and strong filtering and the other with standard coordinates and reduced filtering. The latter case is illustrated on Figure 4.4, left hand side plot. The poloidal variation of the GYSELA computed electric potential at step 0, ϕ_G, hence prior to the evolution is compared to the expected shape ϕ_0 determined using the penalization constraints. Both potential are normalized and vary between zero, the constrained value in the limiter, and one in the plasma. The chosen normalized radius is $\rho = 1.05$, and $N_\theta = 512$. The poloidal angle is labeled by the poloidal index i_θ. The limiter is centered on $i\theta = 360$, and, for the chosen value of ρ is characterized by a width of 35.15 and extent of the transition region of 1.2. The maximum poloidal mode is 256 and Fourier filtering is made with a threshold at poloidal mode number 100. Gibbs oscillations with typical relative amplitude up to 5 % are observed both in the plasma and limiter regions. The same simulation has been run using the so-called "aligned-coordinate" calculation of the parallel gradient where all modes above 50 are filtered out, Figure 4.4, right hand side plot. The departure of the GYSELA solution ϕ_G from the prescribed shape ϕ_0, normalized as previously, is plotted versus the poloidal index. Only the Gibbs oscillations appear, plain black curve. These are compared to an analytical reconstruction with tanh shape and otherwise identical parameters, this leads to the plain blue curve. The shape of the solution of the Poisson

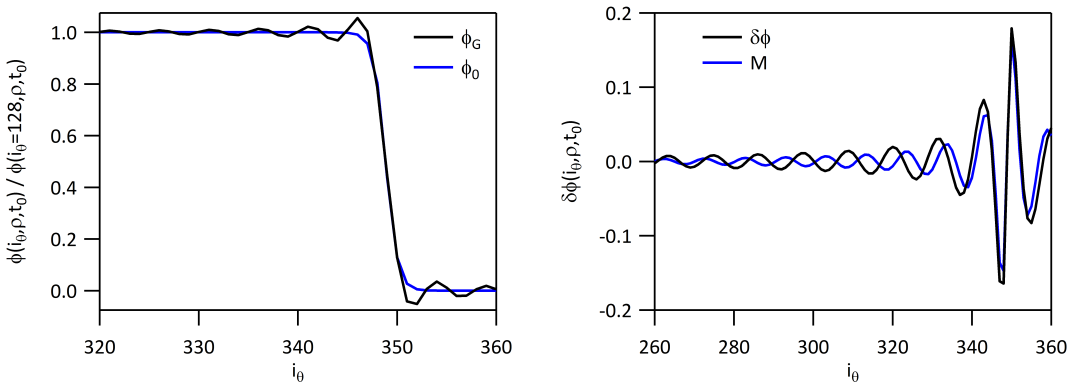

Figure 4.4: Gibbs oscillations of the electrostatic potential from the GYSELA output, here at initial time t_0. Left hand side, GYSELA determined potential ϕ_G (black curve) at the limiter compared to the shape of the mask ϕ_0 (blue curve) versus the poloidal index i_θ for the standard coordinate simulation. Right hand side, Gibbs oscillations $\delta\phi$ (black curve) for the "aligned coordinate case", compared to an analytical expression computed for the mask function M (blue curve) versus the poloidal index.

equation is thus found to quite similar to that of the mask function. One finds in this case that the Gibbs oscillation nearly reach 20 % and are therefore visible in the output data.

The existence of such a transition region can also be an issue regarding the physics that are generated since such a region is characterized by a varying amplitude of the penalization process. As a consequence, within the transition region, both the plasma and boundary physics are at play, each with varying weight. The transition region thus appears as a gray zone without straightforward interpretation. Although it is a known drawback of the penalization technique, that one aims at reducing by increasing the resolution at constant number of points in the transition region, it can be of interest when one keeps in mind that the geometry of the actual plasma facing components departs from the simplified picture one can have, by design, actual positioning in the machine, aging, as well as uncontrolled departure from the ideal magnetic equilibrium, due to ripple for instance, that can be understood as a change in the shape of the plasma facing component.

Finally, the restoring force that is applied in the penalized regions also acts to damp the fluctuations which does provides appropriate boundary conditions at the outermost radius of the simulation domain in the Wall region.

4.1.2 GYSELA heat sink

In flux-driven simulations, and in order to achieve steady state conditions, the radial outer boundary must take the role of a heat sink that on average in time will absorb the heat transported from the source region to the outer-parts of the plasma. The GYSELA heat sink is implemented with a Krook-type restoring force at the right hand side of the gyrokinetic equation, localized within the immersed boundary. For convenience, we prescribe different penalization processes in the limiter and wall volumes. However, both

restoring forces takes the same generic form:

$$-\nu M^{LIM}(r,\theta)(f-g) \tag{4.1}$$

This term is characterized by three parameters: *(i)* the restoring force strength ν determines how fast the distribution function f relaxes towards the target distribution g with respect to its time evolution. We apply an infinite restoring force $\nu \to \infty$ with the numerical technique described in Appendix C *(ii)* The mask function M^{LIM} restricts the action of the restoring force to the limiter shaped boundary region. Finally *(iii)* the target distribution g is a Maxwellian in normalized velocity space at low temperature so that the restoring force acts as a heat sink.

$$g = \frac{n_{target}}{\left(2\pi T_{WALL}\right)^{3/2}} e^{-\frac{1}{2}(v_\parallel^2+\mu B)/T_{WALL}} \tag{4.2}$$

The target Maxwellian g is characterized by two parameters: the wall thermal energy T_{WALL} and the density n_{target}. These are constrained by the model. Regarding the wall temperature, one finds that a global code like GYSELA with a single patch for the normalization of the thermal velocity must meet two requirements. Indeed the number of grid points in both the parallel direction and in the transverse direction must be chosen to ensure an accurate calculation of the density. Regarding the plasma center, with thermal energy usually larger than the normalization value, one must choose in a proper way the upper and lower bounds of the velocity mesh. Conversely, at the wall boundary, the wall thermal energy is constrained by velocity mesh: a too narrow Maxwellian would extend on too few grid points for a accurate calculation of the density. For a typical grid $(v_\parallel, \mu)$ of $(128, 32)$ points, the relative error on the velocity integration with Simpson scheme (figure 4.5) is smaller than 10^{-2} when the dimensionless thermal energy T ranges between 0.05 and 3. When considering the low temperature range, the error is inversely proportional

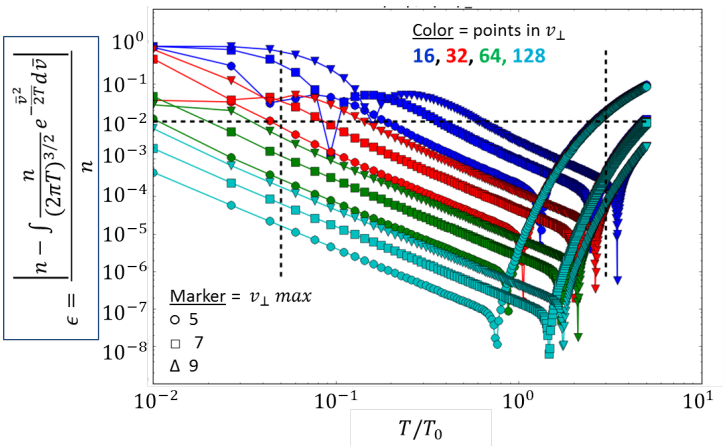

Figure 4.5: Relative error on the calculation of the velocity integral of a Maxwellian distribution with a Simpson integration scheme, in function of the temperature of the Maxwellian for different velocity grid size. In colors the error for different number of grid points, the markers indicate the maximum size of the velocity axis. The calculation is performed for a Maxwellian in the perpendicular velocity, the other direction being equivalent.

both to the number of grid points and to maximum velocity value, since for a reduced

maximum velocity the mesh step is smaller providing a more accurate description of the narrow Maxwellian distribution. Conversely for the high temperature range, reducing the maximum velocity tends to cut out part of the Maxwellian tail that contributes significantly to the velocity integral, thus increasing the error, while the number of grid points in the chosen range has little impact. In general, we set the wall temperature to be ~ 10 times smaller than that of the core plasma. It is approximately half of the temperature at the separatrix.

The constraint on the choice of the target density n_{target} is governed by particle conservation and boundary stability issues. In practice, particle transport is not impeded across the immersed boundary. When considering particle balance for the gyro center density n_{GC} one obtains:

$$\partial_t n_{GC} + \boldsymbol{div}\cdot\boldsymbol{\Gamma}_{GC} = -\nu M^{LIM}\big(n_{GC} - n_{target}\big) \tag{4.3a}$$

$$n_{GC} = \int f(\mathbf{x}_{GC}, v_\parallel, \mu, t) J_v dv_\parallel d\mu \tag{4.3b}$$

where the Jacobian J_v is defined by $J_v = 2\pi B^*_\parallel/m$ and where f is the gyro-center distribution function solution of the Vlasov equation. The gyro-center particle flux $\boldsymbol{\Gamma}_{GC}$ will be further discussed elsewhere. The important aspect is that it appears via a divergence operator $\boldsymbol{div}$, which ensures the conservation properties. Unless n_{target} is constrained to n_{GC}, the right hand side contribution will act as a source term. Consistently, in the limiter region we set at each step of the evolution process $n_{target} = n_{GC}$. This appropriate constraint does ensure however numerical stability since the density can evolve in an uncontrolled way, for instance due to numerical errors. To control such a potential runaway process, the wall initial density is chosen as target density in the wall region. Any particle influx into that region will then break particle balance and impact the electric potential in that region. The rational for this choice is (i) the density and fluxes in that region are small, thus minimizing the particle imbalance, (ii) the spurious electric fields should only distort the physics in that region, which is by definition not relevant being inside the wall immersed boundary. The trade-off presented here will be further discussed in view of the simulation results.

As for the particle conservation, one can address energy transport with the normalized second moment balance equations. The restoring force 4.1 is then shown to yield a perfect heat sink in the limit $\nu \to \infty$. Let $\mathcal{E}_{GC}$ stand for the the second moment of the gyro-center distribution, hence:

$$\mathcal{E}_{GC} = \int f(\mathbf{x}_{GC}, v_\parallel, \mu, t) J_v \Big(\tfrac{1}{2} v_\parallel^2 + \mu B\Big) dv_\parallel d\mu \tag{4.4a}$$

One can then show that the restoring force term yields:

$$-\nu M(r,\theta) \int_{-\infty}^{+\infty} (f-g) v^2 dv = -2\nu M(r,\theta)(\mathcal{E}_{GC} - \mathcal{E}_{target}) \tag{4.4b}$$

where $\mathcal{E}_{target}$ is the internal energy associated to the distribution function g, by construction of g this is purely thermal energy. In the limiter region, the densities that appear in both $\mathcal{E}_{GC}$ and $\mathcal{E}_{target}$ are the same. Defining the energy per particle as $\mathcal{T}_{GC} = \mathcal{E}_{GC}/n_{GC}$ and $T_{WALL} = \mathcal{E}_{target}/n_{GC}$, one finds that the energy loss governed by the restoring force

is proportional to $\nu(\mathcal{T}_{GC} - T_{WALL})$. Since as initial condition we have $\mathcal{T}_{GC} > T_{WALL}$ and since the system only has a volumetric energy source in the core and heat loss via the restoring force in the limiter, one readily expects that the initial inequality holds at all times. Setting $\nu \to +\infty$ then ensures that the limiter is a perfect thermal sink since it will accommodate any energy influx and remain at constant temperature.

4.2 Heat transport: the limiter induces parallel transport in the SOL

In this section we verify that the penalized heat sink described in the previous section 4.1.2 drives a transient parallel heat transport in the SOL region. In that respect, the poloidal asymmetry given to the mask is crucial since it creates the plasma layer, namely the SOL, in which the magnetic field lines close inside the cold immersed boundary. When initializing and enforcing a cold spot inside a poloidally homogeneous plasma domain we expect the propagation of a cold front along the parallel direction, which progressively cools the whole SOL towards the limiter temperature. This front can be seen as a 5D structure defining an interface propagating mostly in the parallel direction in the non-turbulent regime.

4.2.1 1-D 1-V analytical model: propagation of a cold front in phase space

The propagation of the cold front is first analyzed in a simplified linear advection model in the 1-D, 1-V phase space. We follow the motion of a single species along the magnetic field lines, identified by the coordinate x. We neglect all forces acting on the particles, except for that yielding the restoring force within the penalization region. The normalized evolution equation for the distribution function in phase space (x, v) then reads:

$$\partial_t f(x,v,t) = -v\partial_x f(x,v,t) - \nu M(x)\Big(f(x,v,t) - g(x,v)\Big) \tag{4.5}$$

The first term on the right hand side corresponds to the advection along the field line, the

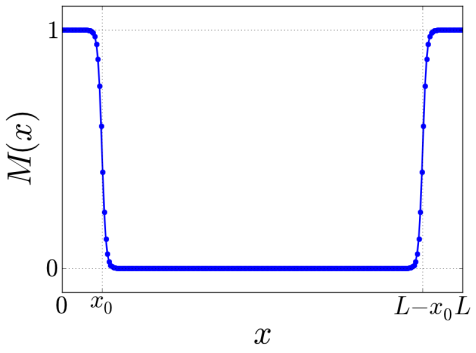

Figure 4.6: Mask function used in the simplified 1-D, 1-V model.

second to the restoring force. The periodic spatial domain is set to be $0 < x < L$ in the

parallel direction. The limiter, of width $2x_0$, is placed half at the left edge and half at the right edge of the domain in the plot of the mask function $M(x)$ on figure 4.6. The plasma region extends between $x_0 < x < L - x_0$. The target distribution function using the normalized phase space coordinates is $n(x,t)g_C(v)$ where $g_C(v) = exp(-v^2/2T_C)/\sqrt{2\pi T_C}$. The normalized thermal velocity off the cold distribution function$\sqrt{T_C}$ and $n(x,t)$ is the local density defined by the 0-moment $\int f(x,v,t)dv$. The first moment of g is equal to zero by symmetry, while the second moment is $n(x,t)\int g(v)v^2dv2\mathcal{E}_C = n(x,t)T_C$.

Let $\Gamma(x,t) = \int f(x,v,t)vdv$ be the particle flux, $\mathcal{E}(x,t) = \frac{1}{2}\int f(x,v,t)v^2dv = \frac{1}{2}\Pi$ the energy density, and $\mathcal{Q} = \frac{1}{2}\int fv^3dv$ the energy flux, then, given 4.5, the system satisfies the following equations:

$$\partial_t n(x,t) + \partial_x \Gamma(x,t) = 0 \tag{4.6a}$$
$$\partial_t \Gamma(x,t) + \partial_x \Pi(x,t) = -\nu M(x)\Gamma \tag{4.6b}$$
$$\partial_t \mathcal{E}(x,t) + \partial_x \mathcal{Q}(x,t) = -\nu M(x)(\mathcal{E} - \mathcal{E}_C) \tag{4.6c}$$

The distribution function is initialized to be hot, namely at the reference thermal velocity, $f(x,b,t=0) = g_H(v) = exp(-v^2/2)/\sqrt{2\pi}$ in the plasma region and cold $f(x,b,t=0) = g_C(v)$ in the limiter region,

$$f(x,v,t=0) = f_0(x,v) = n_H g_H(v)(1 - M(x)) + n_C g_C(v)M(x) \tag{4.7}$$

Here n_H, n_C are chosen initial densities. Starting from homogeneous density one then sets $n_H = n_C = 1$. The normalized thermal energy T_C is assumed smaller than the 1, as required for a cold spot, and set here to $T_C = 0.4$.

Advection in the phase space

Inside the plasma region, the mask is equal to zero and no force is acting on the system. The trajectory is a uniform motion at constant velocity:

$$\frac{dx}{dt} = v \qquad \frac{dv}{dt} = 0 \tag{4.8}$$

The evolution of the system is determined by the initial state $f_0(x,v)$:

$$f(x,v,t) = f_0(x - vt, v) \tag{4.9}$$

The initial f_0 is shifted in space on the distance vt. Each point of the velocity space is decoupled from the others and follows its own motion at velocity v. Let us first consider the case without the restoring force, hence the free propagation of the initial conditions. Two fronts are thus generated in phase space (x,v), one from each side of the limiter, which transport the cold distribution function from the limiter into the plasma domain as shown in figure 4.7-left. The two fronts are propagating one in the positive direction in the half-plane $v > 0$, referred in the following as v_+, and the other one in the negative direction in the half-plane $v < 0$, here v_-. The trajectory of the two fronts in phase space, hence the velocity at which the distribution function changes from $g_H(v)$ to $g_C(v)$ at a given position x and time t, is determined by the following equations:

$$v_+ = (x - x_0)/t \qquad v_- = -(L - x_0 - x)/t \tag{4.10}$$

In absence of any restoring force, the periodic boundary conditions make the fronts reappear on the other side of the spatial domain as the boundary in that direction is reached. The period T = L/v of the motion is inversely proportional to the velocity.

For a given spatial position in the plasma region, the initial hot distribution function is converted to the lower cold value as the front passes by. Since the motion is ballistic, this process occurs earlier at higher velocities. Hence, on the right (left) of the limiter, the cooling process starts at the highest positive (negative) velocity and, as time increases, it progressively propagates towards lower velocities, as shown in figure 4.7-right (dotted and dashed lines). After sufficient time for the opposite front to reach the same spatial position, also the negative (positive) velocities are affected by the cooling (figure 4.7-right dash-dotted line). Only in the middle of the box, where the distance from the limiter is the same in both the directions, is the cooling process symmetric in velocity space. At all other positions, the cooling process asymmetrically distorts the distribution function in velocity space, consequently the effect on the temperature is non linear.

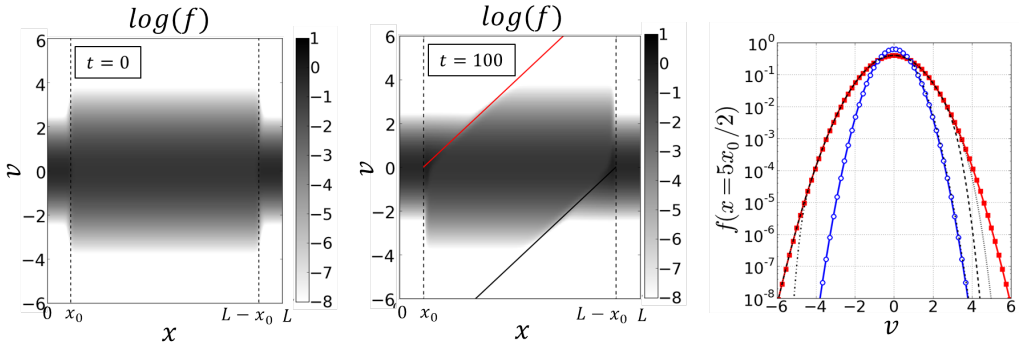

Figure 4.7: *Left*: Distribution function initialization in logarithmic scale. *Center*: Evolution of the distribution function in phase space (x, v) in logarithmic scale. The red/gray solid line is the front v_+ propagating for $v > 0$, the black solid line is the front v_- which propagates for negative velocities. *Right*: Cut of the distribution function evolution in velocity space starting from the initial hot value (squares), three consecutive times (dotted, dashed and dash-dotted line respectively) and the final cold state (circles)

Competition between advection and restoring force

Inside the limiter region defined by the mask M, the restoring force drives the distribution function towards the target value g_C (Equation 4.6). A competition between the advection term and the restoring force holds within the limiter. To ensure a static cold spot, the restoring force term has to be much larger than the advection term. In particular, the typical time of the relaxation process governed by the restoring force $1/\nu$ has to be shorter than the characteristic advection time, hence the time to propagate through the limiter of extent $2x_0$ at the thermal velocity v_{th}, here $v_{th} = 1$ for the initial hot component of the distribution function, hence

$$\frac{1}{\nu} \ll \frac{2x_0}{v_{th}} \tag{4.11}$$

When the restoring force is weak, the hot front can propagate throughout the limiter region (Figure 4.8-left), following the same dynamics as described before. However, at each passage through the limiter region the cooling process occurs - black goes gray on left

hand side Figure 4.8- being all the more efficient at low velocities. For a chosen velocity $v_1 \neq 0$ the number of passages required to experience significant cooling is then $v_1/(2\nu x_0)$ leading to the characteristic cooling time $t_c = v_1/(2\nu x_0)L/v_1$, where L/v_1 is the return time at velocity v_1. The characteristic cooling time is thus shown not to depend on the chosen velocity $\nu t_c = L/(2x_0)$. It only depends of the geometry of the system determined by the ratio $L/(2x_0)$ and on the efficiency of the cooling process determined by ν. An alternative way of implementing the penalization, which avoids the propagation of a heat front throughout the limiter, is to apply an infinite restoring force $\nu \to \infty$. In this case the restoring force is dominant with respect to the advection term inside limiter region, thus when $M \neq 0$. Setting $\nu \to \infty$ actually transforms the mask shape into a step function, with transitions at the first non zero value of $M(x)$. Inside the limiter, the advection of the heat flux is then negligible compared to the restoring term and the energy balance can be approximated by:

$$\partial_t \mathcal{E} = -\nu(\mathcal{E} - \mathcal{E}_C) \tag{4.12}$$

The analytical solution of this Equation is:

$$\mathcal{E}(t) = \mathcal{E}(t=0)e^{-\nu t} + \mathcal{E}_C(1 - e^{-\nu t}) \tag{4.13}$$

which for $\nu \to \infty$ yields $\mathcal{E}(t) = \mathcal{E}_C$. Inside the limiter region the energy density sticks to the target value $\mathcal{E}_C$ and, at constant density, the thermal energy is driven to the cold value T_C. Consequently, for a given velocity a cold front propagates out of the limiter while no hot front effectively propagates into the limiter (figure 4.8-right). When the cold front has completed one period, the whole domain has been cooled down to the limiter temperature T_C.

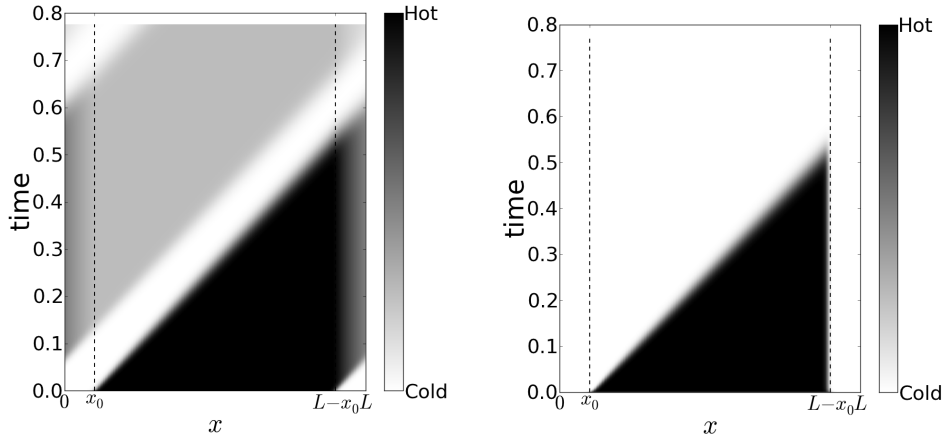

Figure 4.8: Distribution function evolution in real space for a positive velocity $v = +3$ in the case of weak (*left*) infinite (*right*) restoring force.

4.2.2 Parallel front propagation in GYSELA geometry

The numerical implementation of this penalization process in GYSELA is presented in Appendix C. The parallel propagation of the cold front in the SOL is verified in GYSELA. A GYSELA simulation is run where only parallel transport is allowed. The motion along the field lines is observed in the $\theta - direction$. The propagation of the cold front in phase

space is observed on the distribution function, along the $v_\parallel$ and poloidal axes located inside the Scrape-Off Layer, likewise the 1-D, 1-V model. The propagation velocity of the front at given $v_\parallel$ in the poloidal direction can be computed as

$$\frac{d\theta}{dt} = \frac{d\theta}{ds}\frac{ds}{dt}$$

where s is the curvilinear abscissa along the magnetic field lines. The first factor on the right hand side corresponds to the θ-projection of the field line, the second is the parallel velocity. Considering the magnetic configuration in GYSELA (Section 2), the poloidal velocity of the front displacement is constant along the field line with expression

$$\frac{d\theta}{dt} = \frac{v_\parallel}{\sqrt{A_s} q(r) R_0} \tag{4.14}$$

where A_s indicates the mass number of the ion species considered, q the safety factor that is prescribed in GYSELA and R_0 the major radius of the torus. The propagation velocity recovered in the GYSELA simulation is shown on figure 4.9 as well as the theoretical prediction 4.14. The GYSELA results match the predicted value within 1% relative error, mostly introduced when identifying the front location in the output data.

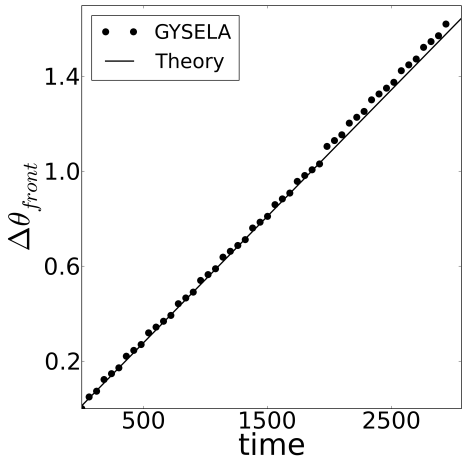

Figure 4.9: Displacement of the cold front in the poloidal direction in function of time. Dots correspond to GYSELA measurements and solid line to the theoretical prediction.

4.3 Particle condensation in the limiter

We show that the poloidally asymmetric heat sink acts as a particle attractor. Two mechanisms contribute to this phenomenon, one in the parallel and the other in the transverse direction. For both mechanisms, a key role is played by the cold temperature in the penalized boundary, which corresponds to a slower thermal velocity with respect to the typical values in the plasma.

4.3.1 Condensation via parallel transport

A phenomenon akin to condensation takes place along the parallel direction due to the propagation of the cold front in phase space. Recalling the $1-D, 1-V$ model of section

4.2.1, we can derive the analytical expression for the density evolution inside the plasma region, where only the advection term is active and is responsible for the propagation of the two fronts v_+ and v_-. This derivation does not take into account the evolution of the distribution function within the limiter region. The main interest is in the understanding of the density behavior when the heat sink drives transport in the parallel direction. This argument is completed in Appendix D, where also the evolution of the flux and temperature are derived.

The moments M_k of order k of the distribution function can be computed as the sum of three integrals in velocity space, namely:

$$M_k = \int_{-\infty}^{v_-} n_C g_C(v) v^k dv + \int_{v_-}^{v_+} n_H g_H(v) v^k dv + \int_{v_+}^{\infty} n_C g_C(v) v^k dv \tag{4.15}$$

The first integral accounts for the convection of the cold distribution function transported by the front v_-, hence it spans from $-\infty$ to v_- in velocity space; the second integral accounts for convection of the initial hot distribution function, thus between v_- and v_+ in velocity space; the last integral accounts for convection of the cold distribution function transported by the front v_+ and it is calculated from v_+ to $+\infty$ in velocity space. Here the notation $n_{H,C} g_{H,C}$ refers to the initial hot (H) and cold (C) contributions to the initial condition, see Equation 4.7. It is important to keep in mind that in this calculation the distribution function in the limiter region is assumed not to vary, hence it remains at the same initial density. In a more complete modeling, one should take into account that after a transient of the order of $2x_0/sqrtT_C$ the influx of plasma entering the limiter on one side will leave the limiter at the other boundary, which will translate into an increase of the limiter density compared to the initial value. This feature will introduce further non-linearity than discussed in the simplified framework described here.

Considering an infinite restoring force $\nu \to \infty$ one can neglect the periodicity of the propagation of the front in velocity space. Considering the motion equation for the fronts v_+ and v_- (equations 4.10), the analytical solution for the zero moment of the distribution function $k = 0$, the density is:

$$n(x,t) = n_C + \frac{n_H}{2} \mathrm{erf}\left(\frac{v}{\sqrt{2T_H}}\right)\Big|_{v_-}^{v_+} - \frac{n_C}{2} \mathrm{erf}\left(\frac{v}{\sqrt{2T_C}}\right)\Big|_{v_-}^{v_+} \tag{4.16a}$$

$$\mathrm{erf}(x) = \frac{2}{\sqrt{\pi}} \int_0^x e^{-t^2} dt \tag{4.16b}$$

Given the chosen assumptions, $n_C = n_H = 1$ and $T_H = 1$, one then obtains:

$$n(x,t) = 1 + \frac{1}{2}\left[\mathrm{erf}\left(\frac{v_+}{\sqrt{2}}\right) - \mathrm{erf}\left(\frac{v_+}{\sqrt{2T_C}}\right)\right] + \frac{1}{2}\left[\mathrm{erf}\left(\frac{|v_-|}{\sqrt{2}}\right) - \mathrm{erf}\left(\frac{|v_-|}{\sqrt{2T_C}}\right)\right] \tag{4.16c}$$

In this expression $v_+ = (x - x_0)/t$ and $|v_-| = (L - 2x_0)/t - v_+$. This expression only holds within the plasma region given that the restoring force is not taken into account. In the same way one can compute the expressions of the first moment $k = 1$, the particle flux, and second moment $k = 2$, the energy (see Appendix D). Inside the limiter region the density will also evolve, however, this evolution is not of particular interest since it is not physical. The only relevant feature of the limiter density evolution is that the total number of particles must be conserved.

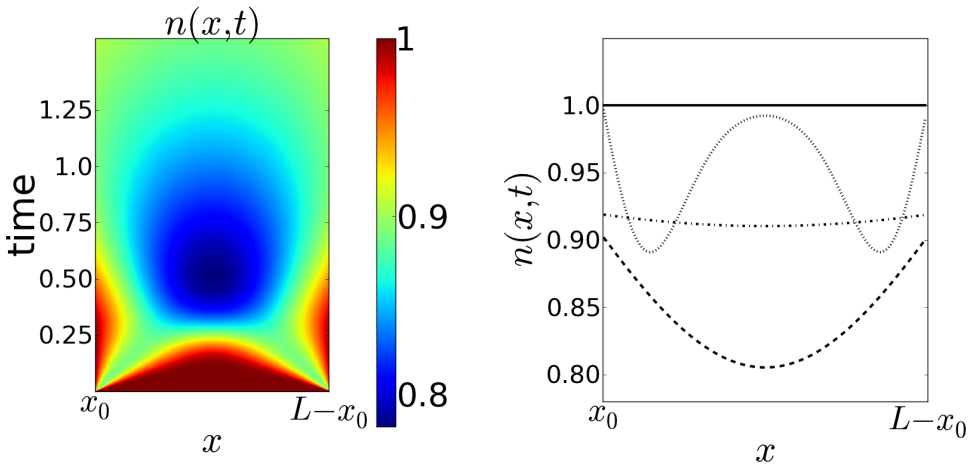

Figure 4.10: *Left*: Spatial and time evolution of the analytical density in equation 4.16a. *Right*: Cut at time $t = 0$ (solid line), $t = 0.3$ (dotted), $t = 1.5$ (dashed), $t = 4$ (dash-dotted line).

On Figure 4.10 are displayed the evolution of the density $n(x,t)$ within the plasma region $x_0 \leq x \leq L - x_0$. obtained from the analytical expression, Equation 4.16c. First, in agreement with Equation 4.16c, the density is symmetric with respect to the middle of the plasma region at $x = L/2$. These feature are recovered when considering the density evolution at $x = L/2$ where $v_+ = |v_-| = v_\pm = (L/2 - x_0)/t$ and at $x = x_0$ where $v_+ = 0$ and $|v_-| = 2v_\pm$.

$$n(L/2,t) = 1 - \left[\mathrm{erf}\left(\frac{v_\pm}{\sqrt{2T_C}}\right) - \mathrm{erf}\left(\frac{v_\pm}{\sqrt{2}}\right)\right] \tag{4.17a}$$

$$n(x_0,t) = 1 - \frac{1}{2}\left[\mathrm{erf}\left(\frac{2v_\pm}{\sqrt{2T_C}}\right) - \mathrm{erf}\left(\frac{2v_\pm}{\sqrt{2}}\right)\right] \tag{4.17b}$$

Let us consider the density evolution at $x = L/2$. In the initial phase, a fast particle flux towards the limiter governs a reduction of the density, pump-out stage. This effect starts from the regions closest to the limiter. It is delayed in the middle of the box due to the bigger distance to reach the limiter, see left hand side plot of Figure 4.10. In a second stage, the matter moving into the plasma from the limiter region restores the density towards the homogeneous value $n(x,t_\infty) = 1$, relaxation to equipartition stage, see left hand side plots of Figure 4.10 and Figure 4.11. This relaxation stage is induced by the fact that the density from the limiter region is kept constant at all times. It would occur in a problem where the limiter region is very big and behaves like a thermal and particle bath, unperturbed when put in contact with the plasma. At the limiter boundary, the balance between the fluxes appears to maintain the density for a longer time, until the transient pump-out takes place before the relaxation towards equipartition. The density trace for a value close to the limiter, red trace on left hand side plot on Figure 4.11, exhibits oscillations of pump-out and relaxation transients until the final relaxation stage. One thus finds that the specific kinetic effects at work in this evolution govern a non-linear behavior of the density although the underlying kinetic framework is linear.

The condensation associated to the local pump-out effect is clearer when considering

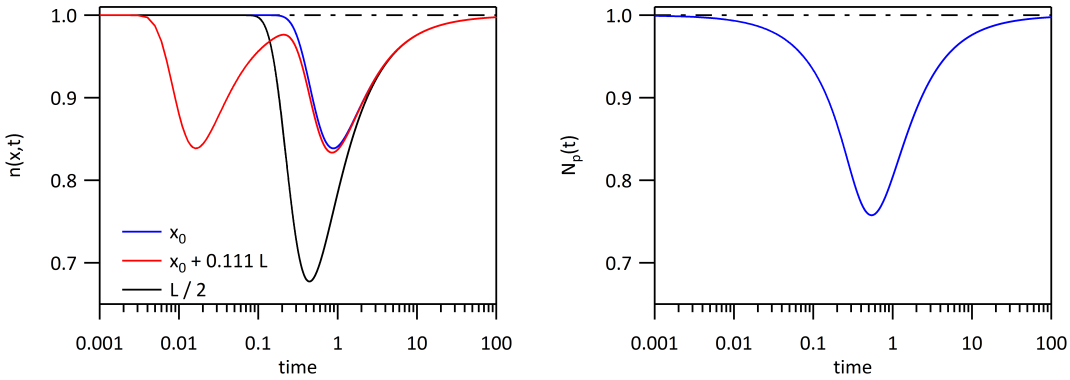

Figure 4.11: *Left*: time trace of the density at three location in the plasma region, black at the plasma center, blue at the plasma boundary, red close to the limiter boundary. *Right*: time trace of the total number of of particles in the plasma region, N_p defined by Equation 4.18.

the total number of particles in the plasma N_p defined by:

$$N_p(t) = \int_{x_0}^{L-x_0} dx\ n(x,t) \tag{4.18}$$

There because of the total particle conservation, adding the plasma and limiter particle contents, one obtains that the pump-out effect observed on N_p must be compensated by a condensation effect in the limiter, see right hand side plot of Figure 4.11. To address the relaxation stage of the evolution, let us use the fluid equations for the density and particle flux.

$$\frac{d^2 N_p(t)}{dt^2} = \partial_x \Pi(x_0, t) - \partial_x \Pi(L - x_0, t) \tag{4.19}$$

According to Equation 4.19, the relaxation is completed when the pressure gradient is constant, hence equal to zero due to the periodicity constraint. In such a framework, the pressure imbalance drives a particle and energy flux to restore homogeneous conditions on both the density and thermal energy.

4.3.2 Vertical drift vs restoring force in the transverse direction

Regarding the motion in the perpendicular direction, the accumulation of particle is caused by the interaction between the vertical ∇B and curvature drifts and the cold immersed boundary. In the GYSELA magnetic configuration the vertical ∇B and curvature drifts velocities constantly drives the ions, with approximately a vertical motion, towards the bottom of the machine. In the confined plasma region, the ions can reconnect to the top of the machine along the parallel direction as well as $E \times B$ motion within the magnetic surface. The induced Pfirsch-Schlüter like ion current then eventually balances the vertical current and bounds the charge separation. The presence of the immersed boundary, in particular of the poloidally asymmetric limiter, modifies this dynamics: the parallel motion, the ∇B and curvature drifts being proportional to the particle thermal

energy are impeded within the cold limiter. Transiently, these cannot balance the particle influx. This mechanism then governs particle accumulation within the immersed boundary, comparable to the condensation mechanism discussed for the parallel motion.

In the previous Section we have focused the discussion on the parallel motion since it is understood that the poloidal symmetry breaking is a key aspect of Scrape-Off Layer physics. As a consequence, this generates parallel motion and transport that are an essential feature of this boundary layer. However, for a limiter with non-zero poloidal extent, as contemplated in this work and as found in actual experiments, the vertical drifts come into play and one can find scales such that the vertical drifts exhibit a time scale comparable to that of the parallel motion. Let us compare the characteristic time scale, for the vertical drifts $\tau_D = \Delta z/v_D$ where the drift velocity is typically $v_D/v_\perp^{th} \sim \rho_*/A$, $\rho_* = \rho_i/a$ namely the ion Larmor radius normalized by the plasma radius a and A is the aspect ratio $A = R_0/a$. The distance Δz is determined by a balance with parallel transport $\tau_D \sim t_\parallel$, with $t_\parallel = l_\parallel/v_\parallel^{th}$. The largest scale Δz is therefore associated to the longest parallel scale, hence $L_\parallel = \pi q R$, and therefore: $\Delta z \sim v_D \tau_\parallel$ and $\tau_\parallel = L_\parallel/v_\parallel^{th}$. Combining the various expressions one then obtains: $\Delta z/a = \pi q \rho_* v_\perp^{th}/v_\parallel^{th}$. Assuming $v_\perp^{th} \sim v_\parallel^{th}$, one then recovers the typical scale of neoclassical transport, which is in fact comparable to the actual scaling retained for the SOL width. For $\rho_* \sim 1/250$ and $q\pi \sim 10$, one then obtains $\Delta z/a \sim 0.04$. A ratio $v_\perp^{th}/v_\parallel^{th} \sim 4$, brings this scale to the typical clearance between the limiter front face and the wall, $\Delta z/a \sim 0.15$. This indicates that a class of particles can experience a drift displacement within the limiter that can be comparable to the radial extent of the limiter, this being independent of the temperature of the cold spot.

The wall region being rather narrow, particle trajectories reaching the wall interface will keep drifting vertically and escape the numerical domain. An alternative has been considered to switch-off this particle loss channel by turning-off the drift terms within the penalized region. In the GYSELA code this is done artificially with a mask function that switches off the drift terms. Alternatively, one can increase the magnitude of the magnetic field at the interface between regions governed by different mask functions. In the latter case, the variation of the magnitude of B will drive a specific response in the curvature and ∇B drifts. These are not computed when penalizing directly the drift convection. It can be shown that the latter procedure violates the phase space conservation, normally embedded in the gyro-kinetic framework. This approximation then governs particle imbalance, which in turn generates large electric fields. Two different solutions have been tested. In the initial one, all the standard drifts have been switched off in both the limiter and Wall regions. An interface barrier then appears at the limiter forefront. Since this region is off particularly interest for the physics, it is far more appropriate to only penalize the wall region, then accepting particle generation at this interface and a barrier isolating the wall from the SOL region. This alternative solution is that presently retained. A better solution would require implementing the variation of the magnetic field amplitude, compute the corresponding drift terms, and then recover the complete gyrokinetic framework with penalized B-variation in the wall region. Last but not least, one can consider particle losses, with kinetic electrons, and then balance quasineutral particle losses by appropriate particle source terms. This is long term effort that requires understanding the particle loss mechanism and their importance in the plasma transport properties. This issue can partly be addressed with the presenting GYSELA versions.

Chapter 5

Global plasma polarization and confinement

5.1 Qualitative discussion of plasma polarization

The electric field generation is most readily understood as the result of charge separation identified in the Maxwell Gauss equation leading to the standard Poisson equation in the electrostatic asymptotic limit. Little volumetric charge imbalance then drives intense electric fields, of the order of MV / m, and the characteristic scale is the Debye length. as will be discussed for the sheath boundary layer. Polarization is the generation on an electric field in a neutral media. Charge imbalance then appears as a surface effect and is coupled to boundary effects. The resulting electric field is then significantly smaller, for Tokamak plasmas is in the kV/m range.

In the present work, the electric field is determined using the quasi-neutrality equation, hence considering charge balance. Polarization sets in because of finite Larmor radius effects. For the electrons, the Larmor radius and the Debye scale are comparable and polarization is not relevant. Conversely, the ion Larmor radius governs a significant distance between the current loop sustained by the ion Larmor rotation and the mean charge position, the gyro-center. In the presence of an electric field, orthogonal to the magnetic field, the particle tends to be slowed down in the low potential side of the Larmor rotation. The charge center is then slightly displaced with respect to the gyro-center, driving a net polarization of the plasma. Consequently, the global electric potential that develops is sustained by polarization but must be driven by an effective charge difference at the plasma boundary. A polarization of the plasma is induced by a net charge density on the flux surface.

The overall build-up of the electrostatic potential structure is thus typically a global polarization of the plasma that sets in due to charge losses, which are governed by a complex combination of particle trajectory effects and transport. We address the global plasma polarization in two stages. We first concentrate on the core plasma, where the electric potential evolution is driven by ion confinement. We then constrain the SOL electric potential in terms of electron confinement. At the separatrix, the plasma must bridge two opposite behaviors. This leads to the specific development of an interface region.

Let us first consider the flux-surface averaged electric potential. As already discussed, the quasi-neutrality equation takes the form a modified Poisson equation, which when

flux-averaged leads to:

$$-\boldsymbol{\nabla}\cdot\left(\left\langle\frac{n_{eq}m}{eB^2}\boldsymbol{\nabla}_\perp\phi\right\rangle_{FS}\right)=\langle n_{GC_i}-n_{e_0}\rangle_{FS} \tag{5.1}$$

The quasi-neutral charge balance, when averaged on a flux surface , Equation 5.1, enforces that the charge due to the ion polarization must be balanced by the charge stemming from a mismatch between the ion gyro-center and electron particle densities. Conversely, when a mismatch between the ion gyro-center and electron charge, appears, governed by the evolution by the gyrokinetic evolution equation of the ion gyro-center distribution function, this enforces an average radial electric field, $\langle\phi\rangle_{FS}$ exhibits a radial profile. This formulation calls for two remarks. First, the polarization term one the right hand side is the leading order term of an expansion in the small parameter ρ_*, in fact an order two term as underlined by the $1/B^2$ dependence, it takes very little mismatch of the densities on the right hand side, to generate significant radial flux surface averaged electric fields. Second, the electron behavior does not play any role in this equation. The latter consequence stems from the particular form given to the electron adiabatic response. Indeed, while the latter appears as a consistent asymptotic limit when considering electron parallel momentum balance, it is clearly more demanding in terms of electron transport when extended to the whole magnetic surface. The implication of the latter assumption is that the electron yield a null contribution to Equation 5.1. It can then be seen that any correction of order larger than ρ_*^2 of the adiabatic electron response will modify the charge balance, Equation 5.1, and tend to reduce the flux surface averaged electric field.

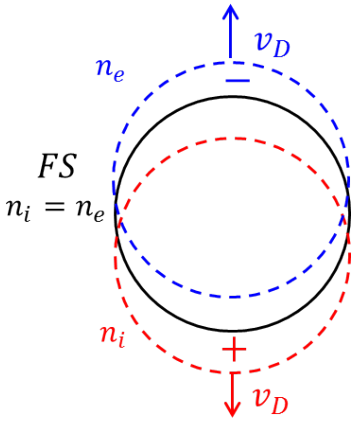

Figure 5.1: Illustration of the polarization of the flux surfaces by the vertical drift v_D

Let us now consider the transport mechanisms that can lead to a difference between the ion gyro-center and electron densities, right hand side of Equation 5.1. In toroidal devices, a drive for large scale currents on flux surfaces are the vertical drifts. On Figure 5.1, a schematic view of this mechanism is shown. Taking into account curvature and ∇B effects, the ion and electron densities tend to drift vertically in opposite directions. This seed for charge separation then drives a polarization of the ions. Equilibrium magnetic configurations allow for closing the electric current loop along the helical magnetic field lines. In such a framework, any form of plasma resistivity inhibits the parallel current and thus enforces a larger response in terms of ion transport. Collisional resistivity in the parallel direction thus governs neoclassical transport. A localized cold spot on a magnetic

surface, as chosen to model the limiter, will most likely drive ion cross-field transport and a change in the radial electric field profile.

In the GYSELA simulations, $\langle\phi\rangle_{FS}$, which is by construction poloidally and toroidally symmetric, is a global structure that develops non-linearly in the course of the system evolution. Its radial profile is directly related to the formation of zonal flows via the $E\times B$ poloidal velocity $\langle v_\theta\rangle_{FS} \propto \partial_r\langle\phi\rangle_{FS}$. The zonal flows are known to reduce turbulent transport by shearing radially elongated structures [6]. When shear becomes large, the consequent quenching turbulent transport is understood as a possible route to the formation of transport barriers. Key contributions to the zonal flows dynamics are retained in the following evolution equation.

$$\partial_t\langle v_\theta\rangle_{FS} \propto \nabla_r\Pi_{r,\theta} \tag{5.2}$$

where the Reynolds stress tensor is defined as $\Pi_{r,\theta} \equiv \langle\tilde{v}_r\tilde{v}_\theta\rangle$. This term is therefore a non-linear contribution of turbulent fluctuations to the zonal flow evolution and it can be shown that it is the only possible source for the zonal flows.

In this chapter we focus on the behavior of the global plasma electric potential averaging out the turbulent fluctuations. We first analyze the self-generated electric potential in the core and relate it to the ion confinement as observed in the data base of simulation used to investigate the confinement time. Next, we address the Scrape-Off Layer radial electric field, and how it is enforced in GYSELA by a penalization of the Poisson equation. We indicate in what respect these changes are consistent with the parallel boundary conditions governed by plasma wall interaction. We then analyze the interplay of core and SOL regions in GYSELA simulations and how this interface generates an $E\times B$ shear layer.

5.2 Core plasma polarization

The plasma polarization in the confined region is mainly determined by the ions dynamics. We recall the radial force balance equation, for which we can express the radial electric field as

$$E_r = \frac{\nabla_r p}{qn} - v_\theta B_\varphi + v_\varphi B_\theta \tag{5.3}$$

In a fully turbulent regime, the three terms on the right hand side can be of the same order of magnitude and are driven by non-linear effects, the poloidal velocity v_θ being generated via $E\times B$ interactions and the toroidal velocity v_φ also generated by the turbulent stress tensor [54], the pressure gradient ∇p modified by turbulence. One can assume that the radial profile of the plasma polarization can be expressed as the sum of two terms, the first is a global smooth profile generated mainly by the vertical drift dynamics and the second corresponds to small oscillations generated by turbulence, primarily the zonal flows. An evaluation of v_θ can be achieved in the neoclassical regime: the poloidal velocity predicted from the neoclassical theory is proportional to the ion temperature gradient, the toroidal velocity is assumed small in the absence of torque injection. The radial electric field is then mostly governed by the ion temperature gradient, and the typical electric potential profile opposite to the ion temperature, hence generating an electric potential well.

The radial shape of the electric potential $\langle\phi\rangle_{FS}$ in the core must fulfill two constraints. Considering cylindrical symmetry it must exhibit a zero radial derivative in the center

$r = 0$. At the outer boundary, the machine wall is grounded. In GYSELA simulations the radial outer boundary condition imposed on the electric potential is set at $\phi = 0$ (choosing any other constant would only shift all the values of the potential and have no implication). Given these considerations, a first approximation for the radial radial shape of the plasma electric potential obtained in GYSELA simulations can be identified as a parabolic function symmetric with respect to $r = 0$ with positive curvature.

In the following two paragraphs we analyze the radial shape of the average electric potential self generated in the core plasma on the basis of GYSELA simulations. We use the steady state simulations which have been collected to build the confinement time scaling law (Chapter 3). In these simulations, a poloidally symmetric boundary condition has been considered and the turbulence is well developed over the whole poloidal section.

5.2.1 Relation to ion thermal energy confinement

The average electric potential in the core plasma is therefore expected to be a potential well which confines the ions. In that respect the electric potential can be read as a global signature of the ion confinement performance.

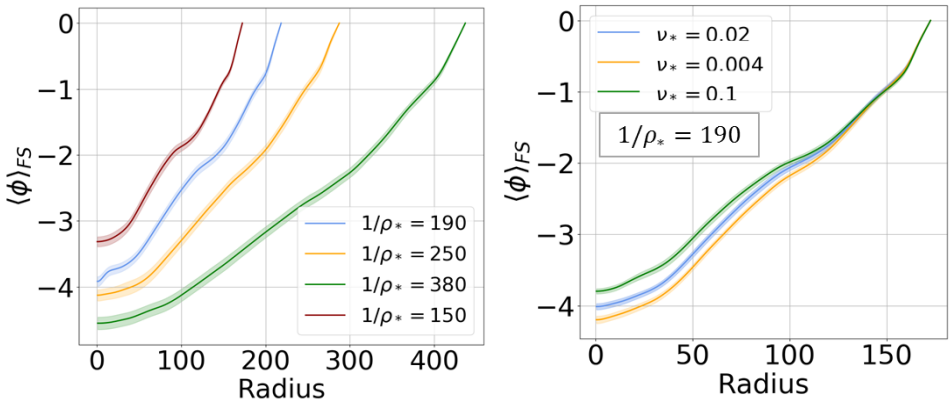

Figure 5.2: Radial profile of $\langle\phi\rangle_{FS}$ averaged in time versus the normalized radius *Right* ρ_* scan, *left* ν_* scan at aspect ratio $A = 6$ and $\rho_* = 150$.

In the simulation data base dedicated to analyzing confinement the source is constrained to maintain all profiles in quasi steady state. Assuming a strong correlation between the potential and ion temperature, one would thus expect the same electric potential profiles when plotted in normalized radius $\rho = r/a$. As can be seen on Figure 5.2 this is not the case. We can then consider a correlation between the flux surface average electric potential and the energy confinement time, and in particular its dependence on the dimensionless control parameters ρ_* and ν_*. We recall the dependence of the energy confinement time on these parameters found in the GYSELA scaling: $\Omega_i \tau_E \propto \rho_*^{-2.7} \nu_*^{-0.14}$. The energy confinement time increases with the plasma size and decreases with the collisionality. In figure 5.2 are drawn the flux surface average potential curves for the plasma size, left hand side, and collisionality scans, right hand side. The time average in solid line within the standard deviation of time fluctuations in opaque colors. Regarding collisionality, the polarization well exhibits a weaker dependence on ν_*, the exponent being typically -0.03, with a similar trend as for the energy confinement time, but very little actual effect, a slight deepening of the well, while the radial electric field at the edge

r_{max} remains constant throughout the scan. Regarding the ρ_* dependence, the potential well becomes deeper with the plasma size. A rather poor scaling can be computed, $< \phi(r = 0) > \propto \rho_*^{-0.3}$. Compared to the ion temperature profile, a striking feature is the overall agreement regarding the shape and depth, $-T_i(r = 0) = -3$, but also the departure with a dependence of $< \phi(r = 0) >$ on ρ_*, although weak compared to that of τ_E as well as a less triangular shape together regions of larger second derivative, hence with higher shear. Little effect of the aspect ratio is been observed in the data base.

5.2.2 A minimal data-driven approach describes the electric potential profile

Given its global character, the radial shape of the electric potential could be used as an additional test to verify the simulation results. At first, one should determine which is the expected shape for the potential in function of the simulation parameters. This study can be addressed using the database of GYSELA steady state simulations. As a first step in this direction we analyze the correlation between the two extremes of the potential curve. We develop a simple parametric algorithm that systematically interprets the $\langle\phi\rangle_{FS}$ radial shape as a combination of parabolic functions by a standard best fitting process. The method that is followed uses the simulation information to set $\phi(r = 0)$ and $E_r(r = r_{max})$ and then determines a fit of the profiles based on a the combination of two parabolas. The parabolic shape in the vicinity of $r = 0$ is generic. Adding a second parabolic dependence for the edge region must be seen as a fitting procedure with a minimum free parameter set.

$$fit(r) = \begin{cases} \alpha_0 r^2 + \langle\phi\rangle_{FS_{r=0}} & \text{for } r \leq r_1 \\ \alpha_2 (r - r_{max})^2 - E_{r_{max}}(r - r_{max}) & \text{for } r > r_1 \end{cases}$$

The parameters colored in blue are fixed: $\langle\phi\rangle_{FS_{r=0}}$ the minimum of the radial polarization at $r = 0$ and $E_{r_{max}}$ the radial derivative of the polarization, the electric field, at the boundary $r = r_{max}$. The other three red parameters, α_0 the curvature in $r = 0$, α_2 the curvature in $r = r_{max}$ and the position of the transition between the two parabolas r_1, are determined by minimizing the error $|\int(\langle\phi\rangle_{FS} - fit)dr|$. An example of the fitting curve is shown in figure 5.3

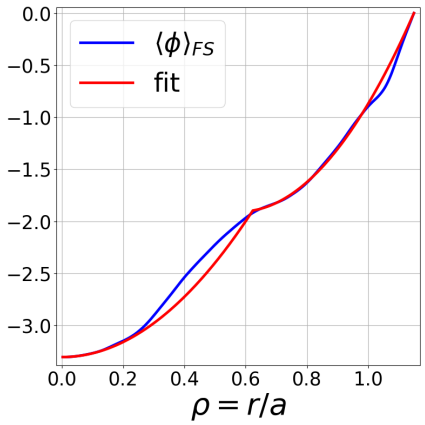

Figure 5.3: Example of the fitting procedure: in blue the instantaneous GYSELA radial polarization and in red the fitting with two parabolas.

The fitting procedure is repeated at each time diagnostics of GYSELA data, resulting in the time evolution of the coefficients α_0, α_2, r_1. The three coefficients are found to oscillate in time at the GAM frequency. For the majority of the simulations in the database we find the three coefficients to be correlated as shown in figure 5.4. The relation between the curvature coefficients in the center α_0 and at the edge α_2 indicates that the higher the curvature at the boundary, the smaller the curvature in the edge and vice versa. Also, for an increasing curvature at either one or the other edge points, the intersection point r_1 moves towards one of the two extremity respectively, indicating that for an increasing curvature the optimal fitting function is represented by only one parabola. The points out of the trend correspond to rare situations in which the chosen fitting function is a too poor model to interpret the $\langle\phi\rangle_{FS}$ shape. Despite this model is extremely reduced, it seems to suggest the existence of a first property of the self-generated electric potential: the higher the electric field at the edge, the flatter is the radial shape of the average potential in the center.

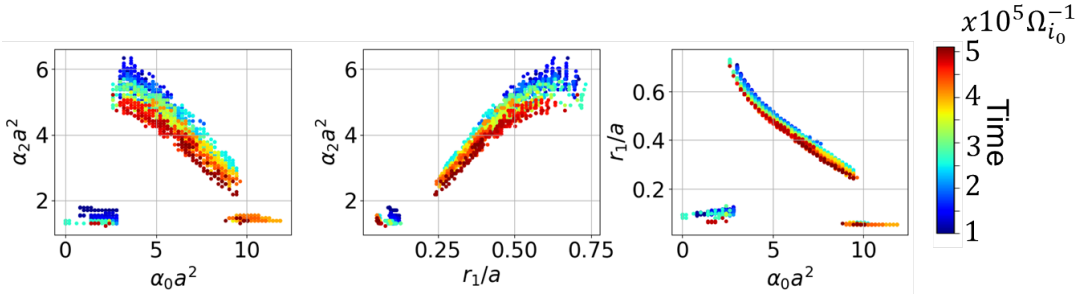

Figure 5.4: In colors the time evolution of the tree fitting coefficients α_0, α_2 and r_1. The three coefficients are plotted one versus the other to underline the correlations between them.

5.3 Interface of core and SOL electric field generation

The penalization we introduce to determine the Scrape-Off Layer electric potential is based on the parallel dynamics of electrons, including the sheath boundary layer at the contact point with the limiter. This governs a reversal of the radial electric field in the vicinity of the separatrix, and, in the GYSELA simulations, a localized $E \times B$ shear layer. The simulations with penalized limiter tend to generate a transport barrier at the core-SOL interface. Such barriers govern long transients so that most simulations have not reached steady state in the SOL region.

5.3.1 Parallel electron dynamics in the SOL

In the SOL region of fusion machines the magnetic field lines close inside the solid matter. The net parallel density flux to the wall is not negligible and is maximum at the wall interface. A sheath layer of the order of a few Debye lengths, in which quasi-neutrality does not hold is generated. The sheath layer develops a large electric field to accelerate the ions out and confine the electrons in. The sheath boundary layer naturally develops to match the electron and ion transport, generating conditions without minimum electric

current outflow from the plasma. Within the sheath layer, the ion density is higher than the electron density and a positive electric field builds up so that electrons remain confined in the plasma.

The GYSELA mesh size, as in many codes, is much larger than the Debye length, hence the code cannot properly resolve the sheath physics. To circumvent this shortfall, we determine the key properties of the sheath in transport regulation. In the penalized limiter region, we implement specific conditions that provide a reasonable approximation to the analytical results with two species.

The potential drop in the sheath

We describe here the conditions that we want to recover with the penalized limiter without modeling the sheath physics. First let us consider the limiter properties.

When considering the physics of plasma-wall interaction one must keep in mind that the wall is a very high density region compared to the plasma such that all ions reaching the wall experience prompt recombination. Furthermore, the wall with its electron density remains neutral despite the plasma influx. It behave as a reservoir with respect to heat, particle and charge. This reservoir is perfectly grounded so that its potential remains at zero (or whatever constant value). In case of biasing, namely the fact that not all wall elements are at the same potential, we further assume that the generator is ideal and maintains the potential constant. Taking such properties into consideration implies that in terms of the plasma evolution, the wall is a cold region such that all the plasma heat is transferred to the solid without modifying the wall temperature, that it will absorb whatever charge flux and remain at constant potential, that the plasma density promptly drops to zero close to the wall surface. To recover the latter property would require to include particle sources in the code to balance the particle loss at the wall, and allow for particle transport, thus model the electron species. The present penalization implemented in GYSELA aims at global simulations with available computing resources, therefore with the trade-off of adiabatic electrons. The condition on plasma density cannot be fulfilled. One then evolves an artificial plasma within the limiter with constraint to conserve particles. The heat absorption is fulfilled by maintaining this plasma at constant thermal energy, the latter being the smallest in the whole domain volume. Finally, one maintains the potential in the limiter volume at a fixed value.

Let us now recover the sheath conditions that must be recovered. The sheath layer is described based on the following list of properties [55].

- Electrons are modeled as adiabatic and at constant thermal energy, which is reasonable when addressing the physics on the ion time scale and on parallel distances small compared to the collision mean free path.

- The ion flux Γ_i is taken constant across the sheath which implies that the ionization process is negligible in the sheath when compared to the total particle source that sustains this particle flux, $|\delta\Gamma_i| \ll |\Gamma_i^s|$ where $|\delta\Gamma_i|$ is the change of particle flux in the sheath layer and $|\Gamma_i^s|$ is the total particle flux that builds-up up to the sheath entrance.

- We assume the net parallel current $j_\parallel$ to be small compared to the maximum current that the ions can sustain $j_{sat} = e\Gamma_i^s = en_i^s c_s$ where n_i^s is the ion density at the sheath entrance and c_s is the sound velocity at the sheath entrance, $|j_\parallel| \ll j_{sat}$.

Given the above properties one can write:

$$\begin{aligned} j_{\parallel}^{W}/e &= \Gamma_i^W - \Gamma_e^W \\ \Gamma_i^W &= \Gamma_i^s + \delta\Gamma_i \approx \Gamma_i^s \end{aligned} \tag{5.4}$$

Combining these two expressions to the smallness of the current into the wall, one then has:

$$\Gamma_i^s \Big| 1 - \frac{\Gamma_e^W}{\Gamma_i^s} \Big| \ll \Gamma_i^s \tag{5.5}$$

where the superscripts s and W stand respectively for conditions at the sheath entrance and at the wall. Equation 5.5 thus yields $\Gamma_i^s = n_i^s c_s \approx \Gamma_e^W$. The electron flux at the wall should be computed in the kinetic framework, however, it can be approximated by $\Gamma_e^W = n_e^W v_{the}^W$ where n_e^W is the electron density at the wall and v_{the}^W is the electron thermal velocity at the wall. As stipulated above, the thermal energy is not expected to vary in the sheath so that $v_{the}^W \approx v_{the}^s$. Furthermore, assuming adiabatic electrons one can relate the electron density at the wall to the electron density at the sheath entrance:

$$n_i^s c_s \approx n_e^W v_{the}^W = n_e^s \; e^{e(\phi^W - \phi^s)/T_e} \; v_{the}^s \tag{5.6a}$$

$$\frac{e(\phi^s - \phi^W)}{T_e} = -\mathrm{Log}\Big(\frac{n_i^s}{n_e^s}\Big) - \mathrm{Log}\Big(\frac{c_s}{v_{the}^s}\Big) \tag{5.6b}$$

As last step we then use the definition of the sheath entrance as where quasi-neutrality holds (see Appendix F), hence $n_i^s = n_e^s = n^s$, so that:

$$\phi^s = \phi^W + \tfrac{1}{2}\frac{T_e}{e} \; \mathrm{Log}\left(\frac{m_i T_e}{m_e(T_i + T_e)}\right) = \frac{T_e}{e} \; \Lambda \tag{5.7}$$

Given Equation 5.7, one thus expects a potential drop from the sheath entrance to the wall proportional to the electron temperature and to the factor Λ. Whenever $T_i/Te \ll m_i/m_e$, $\Lambda = \frac{1}{2}\mathrm{Log}(m_i/m_e)$ is approximately constant, for deuterium $\Lambda \sim 4.1$ and $\Lambda \sim 3.8$ for hydrogen.

Penalized quasi-neutrality equation

In the SOL, magnetic field lines close inside the solid matter and the calculation of the average potential on a flux surface appearing inside the quasi-neutrality equation looses its physical meaning. On the other hand, the average value of the potential along the field line in the SOL is determined by the sheath physics (equation 5.7). This effect is added to GYSELA in the limiter configuration by penalizing the quasi-neutrality equation. In fact, the quasi-neutrality equation is penalized twice: the first penalization drives the flux surface averaged potential to behave as the electron temperature profile inside the SOL region, the second ensures a null potential inside the wall and limiter regions, hence we consider the latters as electrically grounded.

The masks in figure 4.1 are used at the same time to penalize the quasi-neutrality equation. In the poloidally uniform region defined by the mask $M^{SOL}(r)$ the flux surface average potential is replaced by the value $\Lambda(T_e - T_e(r_{max}))$. The reference value $T_e(r_{max})$ is introduced to ensure the boundary condition $\phi(r_{max}) = 0$ at the radial outer boundary.

This procedure corresponds to ensuring the value $T_e(r_{max})$ as a cold electron temperature within the limiter and wall regions. This value is chosen as the minimum of the electron temperature profile. To avoid steep gradients close to the wall, it is advisable to set a flat electron temperature profile for $r > r_{wall}$, that is in the wall region. Within the second 2D mask M^{LIM} in (r, θ), the same used for the penalization of the gyrokinetic equation, the further term $-M^{LIM}(r,\theta)\Lambda(T_e - T_e(r_{max}))$ is added to remove the flux surface average potential from the wall and limiter regions. The quasi-neutrality equation solved in this case is:

$$-\nabla\frac{n_{eq}m}{eB^2}\nabla_\perp\phi + \frac{1}{Z_0^2 T_e(r)}\Big[\phi - (1 - M^{SOL}(r))\langle\phi\rangle_{FS} - \big(M^{SOL}(r) - M^{LIM}(r,\theta)\big)\Lambda\big(T_e - T_e(r_{max})\big)\Big] = \rho \quad (5.8)$$

5.3.2 Self-generation of $E \times B$ shear at separatrix

The introduction of the parallel electron dynamics in the SOL as described in section 5.3.1 determines the flux surface average potential in the SOL region. Conversely the electric potential in the confined region is free to evolve. The resulting radial profile of the flux surface averaged potential changes slope when crossing the closed-open field line interface: in the core indeed the build up of the flux surface average potential is dominated by the ion physics as described in section 5.2 resulting in a positive slope. In the SOL the flux surface average potential follows the electron temperature profile, of negative slope. An example of the radial shape of the electric potential averaged on the flux surface is shown in figure 5.5. The curve is extracted from a reference simulation with the penalized

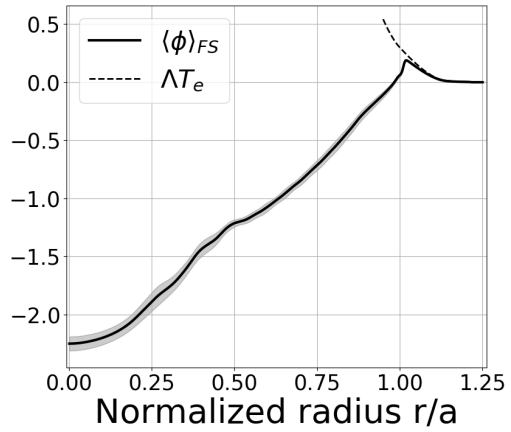

Figure 5.5: Radial profile of the flux surface averaged electric potential when coupling the core and SOL regions. In solid line the mean value on a time interval of $10^5\Omega_i^{-1}$ subsequent to the initial reorganization phase. In shadow the standard deviation of the fluctuations. In dashed line the target value ΛT_e in the SOL.

limiter boundary (Chapter 4) and the penalized quasi-neutrality equation 5.8. Details of the simulation are presented in the following chapters 6 and 7. A similar behavior of the electric potential is found when scanning both physical and numerical parameters. The

reversed slope of $\langle\phi\rangle_{FS}$ when crossing the separatrix appears as a robust result of the coupling between the core and a reduced SOL dynamics.

The electric field reversal in the vicinity of the separatrix is reported in the experiments both in low (L-mode) and high confinement (H-mode) discharges, in limiter as well as divertor configurations [56, 57, 58]. An enhanced negative electric field is observed close to separatrix in the confined region for H-mode plasmas. One can consider that the poloidal asymmetries of the electric potential, often due to turbulence, are small compared to the global radial shape. Hence one can compute the radial electric field as the radial derivative of the flux surface averaged potential. An example of the reversed radial electric field found in the GYSELA simulations is shown in figure 5.6. The corrugations in the core profile are generated by the turbulent fluctuations.

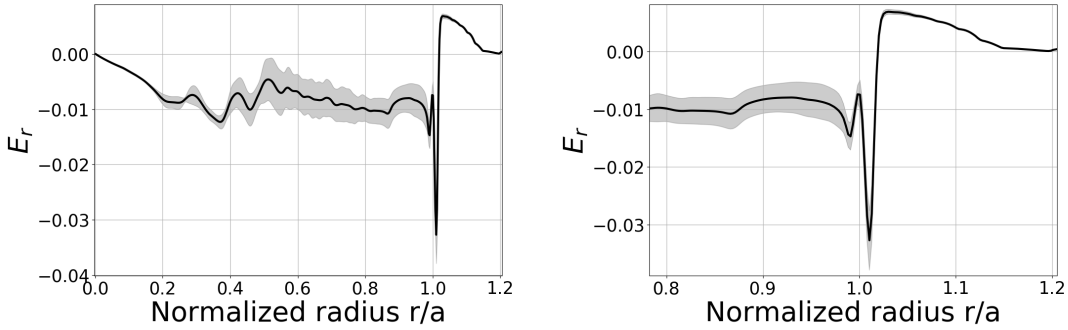

Figure 5.6: *left*− GYSELA radial electric field resulting from the coupling of core and SOL dynamics. In solid line the mean value on a time interval of $10^5\Omega_i^{-1}$ subsequent to the initial reorganization phase. In shadow the standard deviation of the fluctuations. *right*− Zoom around the separatrix.

As a consequence of the reversed electric field, the $E\times B$ shear is enhanced at separatrix (Figure 5.7), about one order of magnitude higher than in the core. The build-up of this strong shear layer at separatrix is rather fast: it appears since the first iterations $t \sim 10^3\Omega_i^{-1}$. After an initial reorganization phase on time scales smaller than $t \sim 10^4\Omega_i^{-1}$, the magnitude of the shear layer appears to fluctuate around a mean value, which is increasing on much longer time scales $\sim 10^5\Omega_i^{-1}$. The standard deviation of the fluctuations is reduced at separatrix with respect to the core. The enhanced shear layer at separatrix results in an enhanced shear of the $E \times B$ poloidal drift velocity. This effect contributes to generate a transport barrier as described in next chapter, section 6.1.2.

Summary and discussion

This work points out two main conclusion.: On the one hand, the mean value of the electric potential in the core can be related to plasma confinement and is found to exhibit a qualitatively similar dependence on the control parameter as the energy confinement time. However, the dependence is significantly smaller. On the other hand, the interplay with the Scrape-Off Layer electric potential creates a strong shear layer, which contributes to generate a transport barrier at the separatrix. These results still need to be confirmed by (i) simulations with kinetic electrons, which can modify the polarization level in the core, (ii) achieving steady state simulations with the SOL. These are difficult to reach because

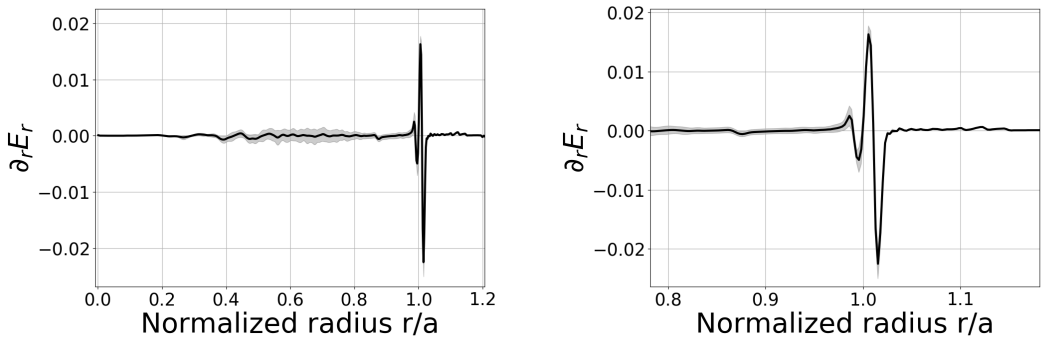

Figure 5.7: *left*− $E \times B$ shear resulting from the coupling of core and SOL dynamics. In solid line the mean value on a time interval of $10^5 \Omega_i^{-1}$ subsequent to the initial reorganization phase. In shadow the standard deviation of the fluctuations. *right*− Zoom around the separatrix.

the transport barrier at the separatrix slows the evolution of the SOL conditions. To analyze the data base of GYSELA simulations, we have taken advantage of data analysis techniques: one could perform systematically such studies in order to seek for hidden correlations between quantities such as the radial electric field, the turbulent fluctuations, the pressure gradient and the internal energy. Finally, we have found that the core-SOL interface, with two different mechanisms governing the electric field, generates an interface transport barrier [59].

Chapter 6

Initial transient with penalized gyrokinetic SOL

This chapter is focused on the description of the global effects of the limiter boundary layers on plasma transport properties. We present the particular transient initial dynamics of the SOL fluid quantities (density and temperature) generated by a combination of effects introduced with the penalized limiter boundary condition. Next we analyze the impact of the new boundary on guiding center transport in the GYSELA simulations.

6.1 SOL initial transient

The initial conditions of the code with immersed limiter boundary generate initial transients in the SOL region, which results in the reorganization of the SOL gyro-center density and temperature on intermediate time scales between the characteristic time of turbulent fluctuations and the energy confinement time. Describing the transient dynamics and its generation mechanisms is the focus of this section.

6.1.1 Initialization and effects introduced with the SOL boundary condition

GYSELA simulations are initialized with a distribution function f_0 which is a Maxwellian, usually at zero mean velocity. The density and temperature distributions are defined by a radial profile and are poloidally and toroidally symmetric. Within the limiter and first wall boundary, the temperature is fixed at the wall temperature T_W, which is also the lowest value of the temperature radial profile anywhere in the plasma volume since initialization. In the region corresponding to the experimental open field lines $r/a > 1$, the density is initialized as constant along the field lines. Conversely the temperature, yet constant in the SOL plasma, shows a parallel gradient when the field line enters the penalized region in the limiter. We remind that the presence of the solid matter in GYSELA is modeled by enforcing a poloidally localized cold plasma: both the field lines and the plasma itself are still defined within the penalized limiter and first wall regions, although the dynamics there is not considered in the present discussion. A small perturbation of typical relative amplitude $10^{-5} f_0$, is added to the initial distribution as the sum of an arbitrary number of poloidal and toroidal modes. Within the penalized regions, the perturbation is set equal to 0. The SOL boundary condition is completed by adding the radial electric field

penalization, which is designed to account for the parallel dynamics of electrons in the plasma-wall interactions. The limiter and wall regions are electrically grounded. The quasi-neutrality is given by Equation 5.8. Finally, in order to limit the particle transport within the limiter and wall regions, the transverse drifts velocities v_D and v_E have been multiplied by the mask $(1 - M^{LIM})$. However, in order to avoid introducing specific conditions close to the separatrix, this assumption was relaxed in a more recent stage; the curvature, ∇B and $E \times B$ drift are then only switched-off in the wall region.

The setting of the SOL boundary here described generates an initial phase of redistribution of density and temperature in the SOL. The transient dynamics is governed by the combination of several effects, driven mainly by the conditions imposed in the limiter, and adds up to the background initial reorganization of the distribution function dominated by the GAM activity (see Section 2). Some of these effects have been already presented in details in the previous chapters, all are summarized hereafter. *(i)* As described in chapter 4, the initialization of a cold and poloidally asymmetric spot in the plasma induces the propagation of a cold front in the parallel direction which cools down the SOL at limiter temperature. *(ii)* Regarding particle transport, the limiter acts as a particle attractor both in the parallel and transverse directions. Hence right after the initialization, the SOL density begins to migrate towards the limiter. We note that the condensation mechanism in the transverse direction can be reduced by placing the limiter at the top of the machine, that is at the poloidal position $\theta = \pi/2$. In this latter case the vertical drift velocity would point opposite to the limiter (with GYSELA conventions for the magnetic field) and does not sum up to the parallel condensation in the limiter. *(iii)* When the parallel electron dynamics is introduced in the SOL, an enhanced $E \times B$ shear layer is triggered close to separatrix (see Section 5.3). Also, the positive radial electric field in the SOL drives a $E \times B$ negative drift, hence clockwise in the poloidal cuts. *(iv)* The potential difference between the SOL and the grounded limiter develops an electric field normal to the limiter surface: the latter coupled to the mainly toroidal magnetic field results in a $E \times B$ drift velocity tangent to the limiter surface, which contributes to moving the particles accumulated at the limiter surface due to the effect (ii). This effect is proper to the simulation set up, via the implementation of the transition layer, and is not associated to the sheath layer physics although the latter would drive a qualitatively comparable effect. *(v)* Finally the suppression of the vertical drifts velocity in the penalized region corresponds effectively to a localized increase in the magnetic field strength, which would generate a secondary drift velocity parallel to the plasma-boundary interface (see Section 4.3.2). However this term is not taken into account in the present model.

In the following we present the initial transient evolution in the SOL referring to a GYSELA simulation which has been run close to experimental conditions of the Tore Supra shot #45511. This simulation will be used in the next chapter to show the effect of the limiter boundary on turbulence development. Although the quantitative analysis of the initial dynamics changes with each plasma configuration, the qualitative features of the transient presented here are characteristic of the GYSELA simulations with that limiter boundary configuration. The considered simulation is run with a set of initial profiles interpolated from the experimental data, shown in figure 6.1. A single ion species (Deuterium) is evolved kinetically with the hypothesis of adiabatic electrons. The plasma size is $\rho_* = 1/316$, aspect ratio $A = 3.2$ as in Tore Supra, collisionality $\nu_* = 0.24$. The mesh size corresponds to $\left(N_r, N_\theta, N_\varphi, N_{v_\parallel}, N_\mu\right) = (512, 1024, 64, 128, 32)$ extended on a quarter of torus $0 < \varphi < \pi/2$, $-7 < v_\parallel < 7$, $0 < \mu < 20$. The radial direction is

extended between $0 < r/a < 1.25$. The distance between the separatrix and the first wall is between $1 < r/a < 1.2$, the limiter is poloidally located at $\theta = 3\pi/2$ with a flat surface geometry as in figure 4.2. The normalized wall temperature is set to be $T_W/T_{r/a=0.5} = 0.20$, corresponding to the lowest value of the ion temperature profile. The drift velocities v_D and v_E are killed within the limiter and first wall mask. The source term consists in a poloidally symmetric hyperbolic tangent in the radial direction, with transition to zero at $r/a = 0.3$, slope 0.1 and amplitude 0.0085. The collision term is the state of the art linearized multi-species operator developed and tested in [25].

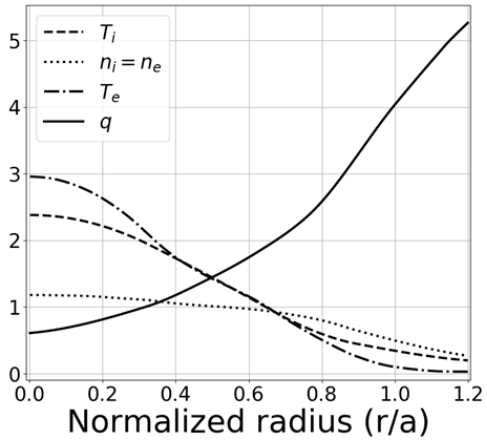

Figure 6.1: GYSELA profiles set interpolated from Tore Supra experimental measurements.

6.1.2 The onset of a weak pedestal

Two of the effects described before are found to affect the temperature distribution in the SOL. From one side the enhanced parallel transport in the SOL drives the propagation of a cold front from the limiter sides, which cools down the SOL. On the other hand the enhanced $E \times B$ shear at the separatrix results in a localized sheared poloidal velocity. The evolution of the temperature as a radial profile averaged on the flux surfaces is shown in figure 6.2, left. In the core $r/a < 0.95$, the temperature profile is constant, sign that in this region the simulation is run close to steady state conditions as described in Section 3.2.1. The temperature gradient steepens at separatrix, between $0.95 < r/a < 1.01$ from early times $t = 2 \cdot 10^4 \Omega_i^{-1}$, forming a small pedestal. The pedestal is present throughout the simulation and is found to slightly increase on time scales comparable to the entire simulation length ($10^5 \Omega_i^{-1}$).

The pedestal region is located in the neighborhood of the self-generated $E \times B$ shear layer in the vicinity of the separatrix. We observe an increase in the temperature gradient averaged on the flux surface, shown in figure 6.2, right. The temperature gradient between $0.95 < \rho < 1.01$ increases by a factor three with respect to the initial condition on a time interval of $10^4 \Omega_i^{-1}$.

The transport barrier at separatrix

The small pedestal in the temperature gradient is sign of the presence of a transport barrier. If we consider an effective diffusive radial transport the total heat flux Q is

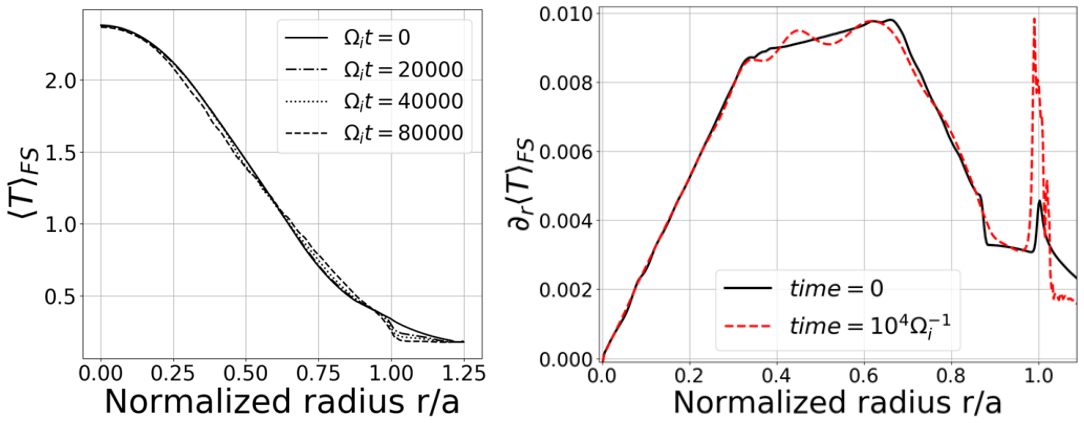

Figure 6.2: *left*− Flux surface averaged temperature profile versus radius at different instant of time: initial $\Omega_i t = 0$ (solid line), $\Omega_i t = 20000$ (dash-dotted line), $\Omega_i t = 40000$ (dotted line), $\Omega_i t = 80000$ (dashed line). *right*− Radial derivative of the flux surface averaged temperature at initial time (black solid line) and at $t = 10^4 \Omega_i^{-1}$ (red dashed line).

related to the radial temperature gradient ∇T by an effective thermal diffusivity κ_{eff} as $Q = -\kappa_{eff} \nabla T$. At constant flux required for steady-state condition, a local increase of the temperature gradient means a locally reduced effective diffusivity. The increased temperature gradient is the signature of a transport barrier. If a transport barrier forms at the very edge of the plasma domain, close to the separatrix, the increased thermal insulation at the plasma edge leads to the possibility to reach a higher core temperature with the same heating power and therefore to improved performance. In experiments [10] a transition from low confinement regime (L-mode) to high confinement regime (H-mode) is observed as a bifurcation phenomenon with a threshold on the external heating power. A complete understanding of the mechanism leading to this transition is still missing.

A non-linear drive for the generation of an increased temperature gradient is found in the radial electric field, as can be readily seen by the radial force balance equation 5.3. We test the influence of the SOL radial electric field on the formation of the barrier. We compare two simulations, one with the proper SOL polarization $\langle \phi \rangle_{FS} = \Lambda T_e$ and in the other we artificially set $\langle \phi \rangle_{FS} = 0$ so to have null SOL radial electric field. The simulations are run on the same parameters as in Section 6.1.1. On Figure 6.3 are shown the time trace of the radial temperature gradient averaged in the region close to separatrix $0.95 < r/a < 1.01$ for the two cases. The two curves follow a similar evolution: the average temperature gradient is always increasing in time, although at lower rate for $t > 3 \cdot 10^4 \Omega_i^{-1}$. This indicates that the stationary state is not yet reached in the pedestal region. The temperature gradient is lower in the case $\langle \phi \rangle_{FS} = 0$, which can be related to the fact that for a lower SOL electric field the resulting $E \times B$ shear is lower. Despite this difference, the resulting temperature profiles of the two cases are quite comparable. The maximum difference between the two profiles in the pedestal is comparable with the maximum difference in the confined region, where the profiles are corrugated by the turbulent fluctuations. The temperature gradient steepening at the separatrix appears as a spontaneous evolution of the system when coupling core and SOL dynamics, and more generally when different properties diving the electric potential generate an interface [59].

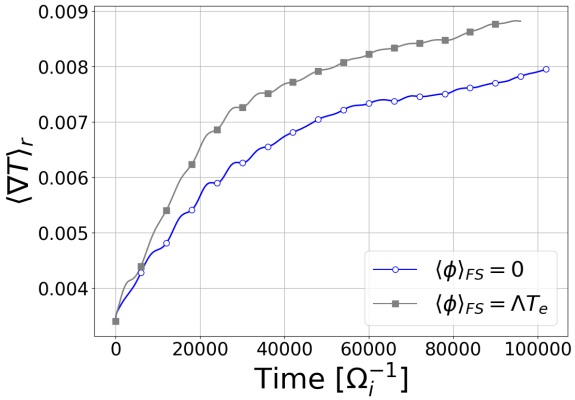

Figure 6.3: Time evolution of the opposite of the temperature gradient averaged in the pedestal region $0.95 < r/a < 1.01$ when the flux surface average potential in the SOL is artificially forced to 0 (empty circles) or to ΛT_e (full squares).

6.1.3 Initial dynamics of the density

We describe the dynamics of the SOL density transient. The simulation starts with a poloidally symmetric density distribution defined by the initial radial profile. Since the limiter acts as a particle attractor and the drift velocities are killed within the limiter mask, the density starts migrating towards the limiter and only penetrates the limiter region via parallel transport. An initial accumulation of particles at the plasma-limiter interface is observed. Considering the GYSELA convention for the magnetic field (Section 2.3.2), the $E \times B$ velocity tangent to the limiter surface is directed horizontally towards the high field side. Consequently, the density accumulated at the limiter surface drifts to the high field side and an in-out density asymmetry is created close to the limiter. From there, the negative poloidal $E \times B$ flows in the SOL redistribute the particle accumulation poloidally in the high field side SOL. An example of the resulting density distribution on the poloidal section is shown in figure 6.4. A clear poloidal asymmetry of the density is observed in the SOL, an over-dense region is found in the third quadrant of the poloidal section. At time $t = 12000\Omega_i^{-1}$ the density is increased up to 60% of the initial value between $1.02 < r/a < 1.15$ for poloidal positions close to the limiter on the high field side region (figure 6.5). The maximum accumulation of the density happens within the transition region where the mask function varies from 0 to 1 in the high field side (figure 6.5 right). The initial transient described here happens on intermediary time scales of the order of $10^4\Omega_i^{-1}$, larger than both the correlation time of turbulence ($< 10^3\Omega_i^{-1}$) and the parallel connection time but shorter than the energy confinement time ($\sim 10^6\Omega_i^{-1}$).

The subsequent evolution of the SOL density is found to be affected by a constant particle loss. This aspect of the simulations with limiter boundary will be analyzed in detail in next section E.1. Also, while the core region develops during the simulation a fully turbulent regime, reaching the statistical steady state on long times, the SOL remains stable for almost the whole simulation duration, that is $10^5\Omega_i^{-1}$, approximately one tenth of the energy confinement time. The fact that the SOL is initialized out of equilibrium indeed delays the achievement of a statistical steady state. A comprehensive study of the 2D SOL equilibrium in the poloidal plane for the GYSELA limiter configuration is being addressed.

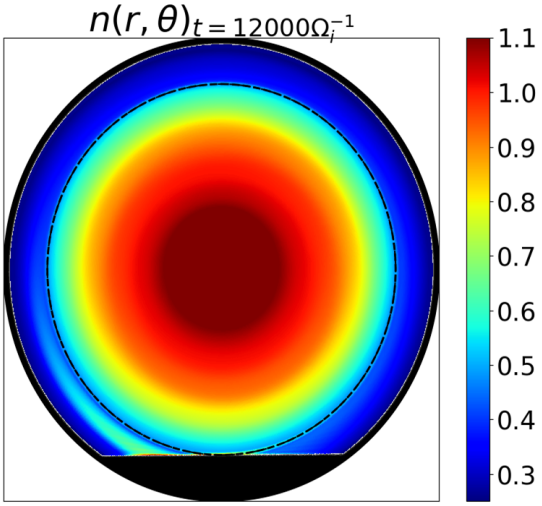

Figure 6.4: Poloidal snapshot of the plasma density at time $\Omega_i t = 12000$ and for an arbitrary toroidal position. In black is the mask $M^{LIM}(r,\theta)$

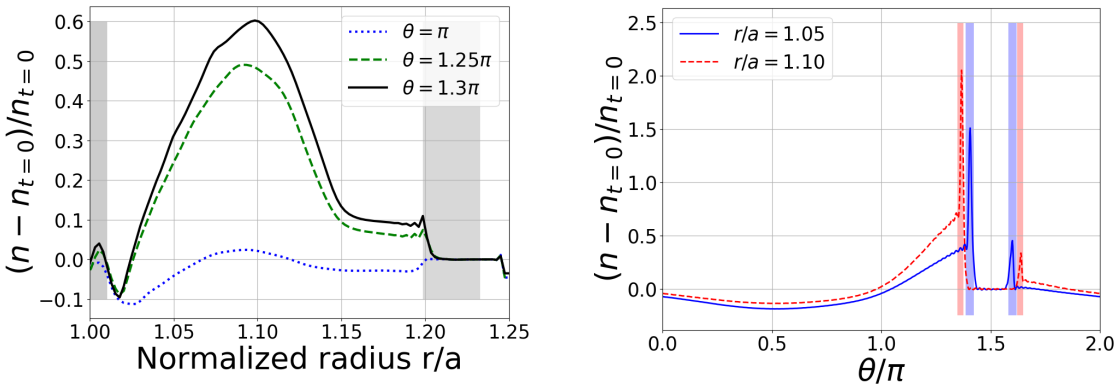

Figure 6.5: Relative difference $\big(n-n(t=0)\big)/n(t=0)$ of the plasma density at time $\Omega_i t = 12000$ with respect to the initial one versus the radius (*left*) for different poloidal position in the SOL and versus θ at two radial cut. In shadow is the mask transition $0 \to 1$

Summary

The new SOL boundary conditions implemented in GYSELA are shown to generate an initial transient which results in a poloidally asymmetric SOL density distribution and the formation of a small pedestal in the temperature profile located at the confined-open field lines interface. The transient takes place on a time scales much longer than the turbulence correlation time, while much smaller than the energy confinement time. A comprehensive study of the SOL equilibrium state in GYSELA simulations is still to be addressed in order to initialize the simulations close to steady state in both confined and open field line regions. This step is required to investigate the interplay between core-edge and SOL turbulence.

Chapter 7

Ion Temperature Gradient and Kelvin-Helmholtz instabilities in GYSELA simulations with Scrape-Off Layer

This chapter is dedicated to describing the effects of the limiter boundary condition on the turbulence in GYSELA simulations. A first analysis is performed in the axisymmetric framework where a Kelvin-Helmholtz like instability is observed, governed by the sheared $E \times B$ velocity layer at the separatrix (section 7.1). Next we present the results of a fully turbulent GYSELA simulation with limiter boundary, where fluctuations are found in the edge region where the initial profiles appear to be subcritical when considering a simulation case with the poloidally symmetric boundary layer (section 7.2).

7.1 Kelvin-Helmholtz instability at separatrix

The Kelvin-Helmholtz (KH) instability is typically an instability generated by a sheared fluid velocity field. It is ubiquitous in neutral fluid turbulence. It can be observed in nature with structures that are reminiscent of the linear stages of the instability, for example as a particular shaping of the clouds in presence of stratified winds (figure 7.1). The mechanism driving the instability can also be extended to the interface between two fluids at different velocities flowing parallel one to the other along the motion direction. This case usually

Figure 7.1: Kelvin-Helmholtz eddies observed in the clouds.

allows for simple visualization of the instability. At the interface between the two fluids a sharp variation, transverse to the motion, then generates ripples of the two-fluid interface. Fluid particles at higher velocity move inside a slower background fluid - and vice-versa - and they are twisted, forming turbulent vortices. This phenomenon usually competes with damping mechanisms, such as viscosity or surface tension at the interface, which then drives an instability threshold in terms of the shear amplitude.

In the core of Tokamak plasmas, the KH-like instability has been already identified as a mechanism of both source and damping of the zonal flows[6, 60, 61]: regarding the first the instability can arise between the streamers, which are radially elongated isopotential cells corresponding to the Ion Temperature Gradient linear modes. When the instability arise, it breaks the radial structures in the transverse direction with respect to their elongation and can form a poloidally and toroidally symmetric flow, the zonal flow. Once the zonal flows are formed, a KH-like instability can form between the poloidally and toroidally symmetric layers. This mechanism breaks the symmetry of the zonal flows and creates turbulent eddies. A KH-like instability can also be triggered by parallel velocity shear. A net difference in the parallel flow velocity is found between the confined region and the SOL, where the plasma is accelerated up to the sonic regime due to the presence of the limiter or divertor plates [62]. The parallel velocity gradient (PVG) instability has been investigated theoretically [63, 64] and observed in the experiments [65]. It has also been recovered in 3D fluid numerical simulations [66]. A recent work identifies the parallel velocity gradient instability as a possible mechanism to drive subcritical turbulence with respect to the ITG threshold [67].

In this section we focus on the KH-like instability generated by sheared poloidal flows at the interface between confined and open field lines regions. These flows are driven by the $E \times B$ drift velocity. The flows are sheared in the radial direction since the electric field changes sign when crossing the separatrix, as shown in section 5.3.1. In this case, the KH may appear as a primary instability for the system. We show that an enhanced $E \times B$ shear at the closed-open field line interface can generate small scales turbulent eddies in the poloidal plane. This phenomenon seems to appear above a threshold in $E \times B$ shear. However, in the present GYSELA simulations, the fluctuations that might be related to the Kelvin-Helmholtz instability appear during a transient with continuously evolving shear layer. This makes any quantitative comparison to the Kelvin-Helmholtz models quite challenging.

7.1.1 A reduced model for Kelvin-Helmholtz instability

We investigate here the linear stability of the plasma driven by a velocity modulation using the TOKAM2D reduced model [68]. In a generic fashion, this system couples a transported field, either the density, the temperature of the pressure, and the vorticity field, in the flux tube approximation where variation in the direction parallel to the magnetic field are ignored. A slab 2D geometry in x, radial, and y, poloidal directions is considered. The driving velocity shear is introduced in the model as a sinusoidal function of the electric potential. This particular framework is also referred to in the literature as the modulational instability. We present the linear analysis of the simplest system, where the interchange term is set equal to zero, as well as any source or dissipation term. The evolution of the system is driven by the background electric potential Φ_0 with wave vector $\mathbf{K} = (K_x, K_y)$. The effect of the latter is therefore isolated from the interchange

turbulence drive. Also, since no damping mechanism is considered, the system would result always unstable. The continuity and the vorticity equations read:

$$\partial_t n + \big[\phi, n\big] = 0 \tag{7.1a}$$

$$\partial_t W + \big[\phi, W\big] = 0 \tag{7.1b}$$

where n is the transported field, say the density given the chosen notation, ϕ the electric potential and $W = \nabla^2\phi$ is the vorticity. The Poisson bracket in 2D slab geometry is defined by $\big[f, g\big] = \partial_x f \partial_y g - \partial_x g \partial_y f$. We linearize the system by expanding at first order in the perturbations $|\widetilde{n}|, |\widetilde{\phi}| \ll 1$, considering the order zero density profile as a constant gradient $n_0 = x\partial_x \bar{n} = x/L_n$ and the background potential $\Phi_0 = \hat{\Phi}_K e^{i(K_x x + K_y y)} + cc$. We now assume the system to respond to the background excitation with two different mode numbers $\mathbf{k}_1$ and $\mathbf{k}_2$ satisfying the three wave coupling constraint $\mathbf{k}_1 = \mathbf{K} + \mathbf{k}_2$. The perturbations $\widetilde{n}, \widetilde{\phi}$ will be expressed by the sum of the two modes as: $\widetilde{f_j} = \hat{f}_{k_j} e^{i(\gamma t + k_{jx} x + k_{jy} y)} + cc$ where j stands either for 1 or 2 and f for the perturbed density or potential, t is the temporal coordinate. The linearized system reads:

$$\partial_t \widetilde{n} + \big[\Phi_0, \widetilde{n}\big] - \partial_y \widetilde{\phi}/L_n = 0 \tag{7.2a}$$

$$\partial_t \widetilde{W} + \big[\Phi_0, \widetilde{W}\big] + \big[\widetilde{\phi}, \nabla^2 \Phi_0\big] = 0 \tag{7.2b}$$

Since the coupling between the transported field and the vorticity equation has been set at zero, the density field only tracks the transport governed by the instability. Furthermore, in the absence of dissipation mechanisms, the waves associated to this independent system are bound to be marginal. From this system we can extract a linear set of equations for the amplitude in Fourier space of the modes $\hat{n}_1$,$\hat{n}_2$, $\hat{\phi}_1$ and $\hat{\phi}_2$. When considering the symmetry of the vorticity equation, one finds that the growth rate γ will only depend on the relative direction of the perturbation wave vectors with respect to wave vector $\boldsymbol{K}$ of the drive, and the latter can take any direction in the x, y plane. One can also redefine $\mathbf{k}_1$ and $\mathbf{k}_2$ as

$$\mathbf{k}_1 = \alpha_1 \mathbf{K} + \kappa$$
$$\mathbf{k}_2 = \alpha_2 \mathbf{K} + \kappa$$

with $\mathbf{K} \cdot \kappa = 0$ and $\alpha_1 - \alpha_2 = 1$. We write the dispersion relation for the growth rate as

$$\big(\gamma^2 + X^2 |K^2 \hat{\Phi}_0|^2\big)\left(\gamma^2 + X^2 \left(\frac{(1 - \alpha_2^2 - X^2)}{(\alpha_1^2 + X^2)} \frac{(1 - \alpha_1^2 - X^2)}{\alpha_2^2 + X^2}\right) |K^2 \hat{\Phi}_0|^2\right) = 0 \tag{7.3}$$

with $X = \kappa/K$. Let $K^2 \hat{\Phi}_0 = V'$ be the absolute value of the amplitude of the velocity shear due to the potential field Φ_0, one finds a compact formulation of the 4 solutions of the dispersion relation:

$$\begin{aligned} \gamma &= \pm\, i |X| V' \\ \gamma &= \pm\, i |X| V' \left(\frac{(1 - \alpha_2^2 - X^2)}{(\alpha_1^2 + X^2)} \frac{(1 - \alpha_1^2 - X^2)}{\alpha_2^2 + X^2}\right)^{1/2} \end{aligned} \tag{7.4}$$

The two former roots lead to marginally stable modes with Doppler frequency $\pm X V' = \kappa K |\hat{\Phi}_0|$. One of the modes associated to the two latter roots can drive an instability provided:

$$X^4 - (a + b) X^2 + ab < 0 \tag{7.5}$$

with $a = 1 - \alpha_2^2$, $b = 1 - \alpha_1^2$. This second order equation in X^2 always has two roots $X_1^2 = b$ and $X_2^2 = a$ and the instability occurs when at least one of these roots is positive. Given the relation between α_1 and α_2 one can set $\alpha_1 = \alpha + \frac{1}{2}$ and $\alpha_2 = \alpha - \frac{1}{2}$. The instability condition is found for $-\frac{3}{2} < \alpha < \frac{3}{2}$ and therefore

$$\begin{aligned} -2 < \alpha_1 < 1 \qquad or \\ -1 < \alpha_2 < 2 \end{aligned} \tag{7.6}$$

We note from the definition of the coefficients a and b that the largest possible root is $X = 1$ and a necessary condition for the instability is $X < 1$, hence $\kappa < K$. The unstable mode would develop on spatial scales comparable to the shear layer width or larger.

The reduced model presented here gives a first and analytically tractable description of the K-H instability as a primary instability for the plasma system. By tuning a background potential of different shape, one could apply the model to several phenomena, such as the K-H instability between the linear streamers or between the zonal flows. In our case, one could improve the calculation by adding a dissipation term, corresponding to the parallel resistivity of the plasma. This would introduce an instability threshold on the growth rate, which depends on the amplitude of the velocity shear V'. However, the comparison of the model with the global system of GYSELA numerical simulations remains still challenging. The main difficulty is that in GYSELA simulations one cannot identify a constant drive for the H-K instability: the poloidal velocity shear at separatrix is indeed self-generated, therefore can be poloidally asymmetric and evolves in time.

7.1.2 Axisymmetric instability

We investigate the problem of the stability of a $E \times B$ shear layer at separatrix with GYSELA numerical simulations. The SOL boundary condition is added, as described in chapter 6. A shear of the poloidal velocity at the interface between confined and open field lines region is driven by the self consistent development of a reversed radial electric field. For the simulations presented in this section, the possibility of an interference of the sheared velocity field with the interchange turbulence has been eliminated by filtering out all the non-axisymmetric modes $n \neq 0$, where n is the toroidal mode number. Only the axisymmetric mode $n = 0$ is evolved, all the parallel terms being still active in the simulations. In this set up, one would expect neoclassical transport to govern the evolution of the system. The radial electric field, and therefore the shear, is determined by the evolution of the plasma as described in Chapter 5 and can be read as enforced by the radial force balance 5.3. In the core region we can consider the neoclassical regime for which $E_r \sim -\nabla_r p/en_e$ and therefore the radial electric field behave as the second derivative of the pressure gradient. In the SOL, the averaged electric potential is at lowest order slaved to the electron temperature profile due the electron parallel dynamics $E_r = -\Lambda \partial_r T_e/e$, with $\Lambda \approx 0.5\mathrm{Log}\big(m_i/m_e\big)$ and T_e the electron temperature.

We present the results of two GYSELA simulations with different choice of initial profiles. The first case corresponds to the set of profiles used in the database used to investigate the ion thermal energy confinement (Chapter 3, figure 3.2), which we identify as *"marginal"* since the profiles are close to the ITG threshold $\nabla_r log(T)/\nabla_r log(n) \sim 2$ over the whole radius. The second set of profiles is interpolated from the experimental data of the Tore Supra shot $TS45511$. We refer to this case as *"experimental"*. The two profiles sets are shown in figure 7.2 We evolve deuterium ion species only with adiabatic

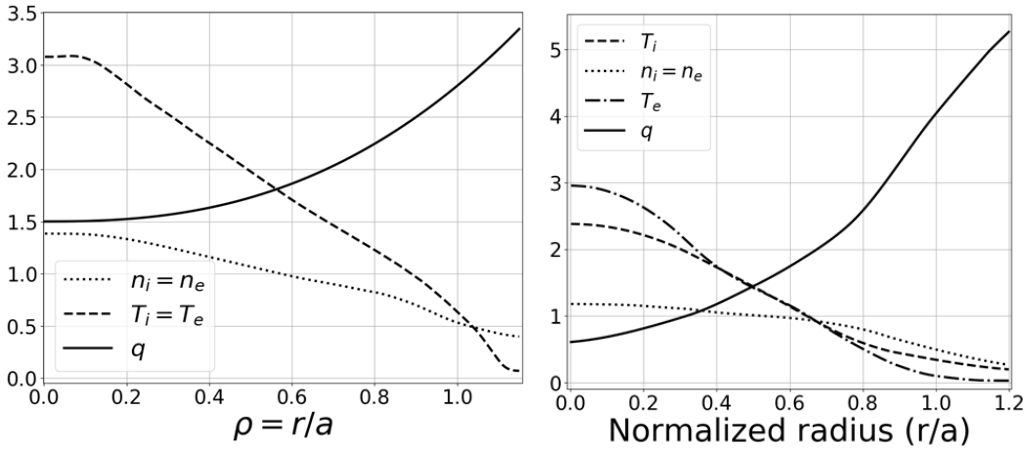

Figure 7.2: *Left*− Marginal and *right*− experimental profiles sets.

	N_r	N_θ	N_φ	$N_{v_\parallel}$	N_μ	L_φ
Marginal	512	1024	32	128	32	$\pi/2$
Experimental	512	1024	32	256	64	$\pi/4$

Table 7.1: Definition of the mesh size in radial, poloidal, toroidal, parallel velocity and magnetic moment coordinates. In the last column the length of the toroidal coordinate.

electrons. The plasma control parameters are $1/\rho_* = 150$, the aspect ratio $A = 6$, the collisionality $\nu_* = 0.02$ with zero source term. The latter has been considered since for this set of simulations, the integration time is too short to lead to significant core evolution. The collision operator, which drive the neoclassical transport, is chosen as the linearized operator of [25]. The mesh size for the two simulations is given in table 7.1. The radial range is $0 < r/a < 1.2$. The SOL extends in $1 < r/a < 1.15$, and the first wall region is set by $r/a > 1.15$. The limiter surface is flat, the geometry of the boundary is the same shown in figure 4.2. The limiter and wall temperature is set as $T_W/T_0 = 0.18$ in the marginal case and $T_W/T_0 = 0.20$ in the experimental case. These values correspond to the lowest value of the initial temperature profile, at $r/a = 1.2$.

The combined effect of different initial profiles and the initial transient in the SOL, which quickly generates a transport barrier, results in different $E \times B$ shear level at separatrix and in the SOL (figure 7.3, left). In the core plasma $\rho < 0.9$ the shear amplitude levels-off between 10^{-4} and 10^{-3} in both simulations. In the vicinity of the separatrix $0.95 < r/a < 1.04$ the shear amplitude increases by two to three orders of magnitude for the experimental and marginal cases respectively. In the SOL $r/a > 1.05$, the shear level is of the order of 10^{-2} in the marginal case and 10^{-3} in the experimental case.

The poloidal velocity for the two simulations is shown on figure 7.3 right hand side. In both cases the poloidal velocity changes sign when crossing the separatrix at $r/a = 1$, following the reversed radial electric field. In the marginal case, the poloidal velocity is one order of magnitude higher close to the separatrix $0.9 < r/a < 1.1$ with respect to both the core region $r/a < 0.9$ and to the experimental case across the radius. Given the axisymmetry of the system, the enhanced poloidal velocity shear at separatrix should be the only physical drive for a possible instability, which would develop in the poloidal plane.

Fluctuations indeed appear clearly for the marginal case at the inner side of the sepa-

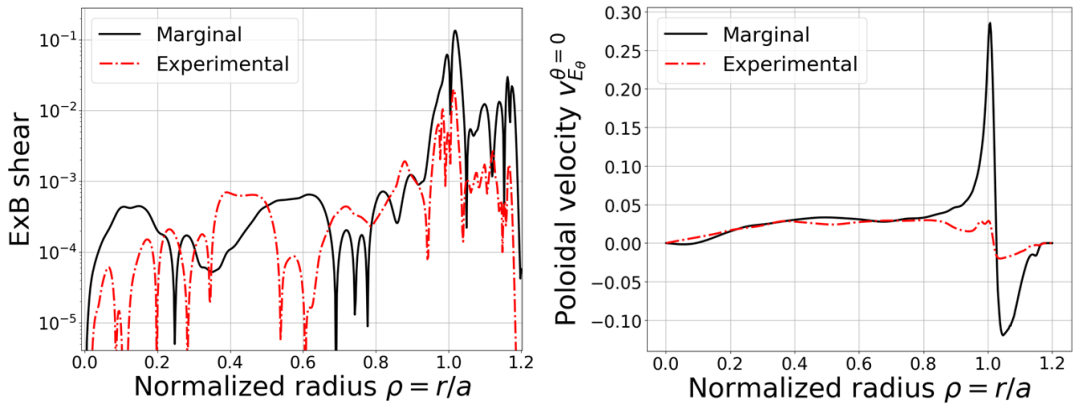

Figure 7.3: *left* − Time average between $4 \cdot 10^3 < \Omega_i t < 8 \cdot 10^3$ of the $E \times B$ shear, i.e. $\partial_r^2 \langle \phi \rangle_{FS}$, for the marginal (solid black line) and experimental (dash-dotted red line) cases in logarithmic scale.*right* − Poloidal velocity vs the radial position averaged on the same time window at the outer midplane $\theta = 0$ for the two cases.

ratrix, where the poloidal velocity shear is largest. On Figure 7.4 is shown a snapshot of the potential fluctuations $\phi - \langle \phi \rangle_{FS}$ for the marginal case in the fourth quadrant of the poloidal section at time $4 \cdot 10^3 \Omega_i^{-1}$. The development of small scale structures is visible close to the separatrix. The core region is still dominated by the global GAM activity, which characterizes the initial reorganization of the distribution function as described in section 2.3.1.

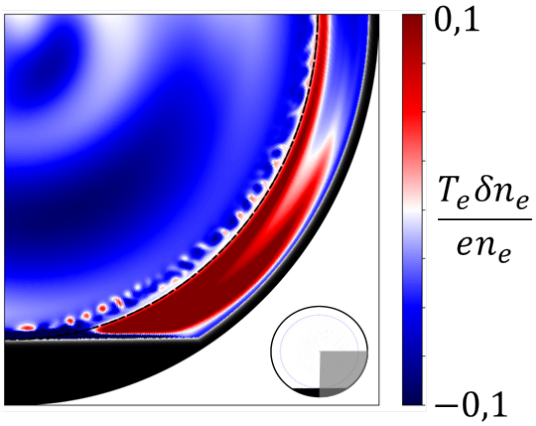

Figure 7.4: Snapshot of the potential fluctuations $\phi - \langle \phi \rangle_{FS}$ at time $t = 4 \cdot 10^3 \Omega_i^{-1}$ in the fourth quadrant of the poloidal section for the marginal case.

Given the axisymmetry of the system, the spectrum of the potential fluctuations can be extracted using a single poloidal plane. However, in the open field lines region, this spectrum is distorted by the presence of the limiter, inside which the electric potential is set to zero. The shape of the limiter is a sum of hyperbolic tangents in the poloidal direction and its Fourier spectrum at $r/a = 1.01$ is close to a sinus cardinal function, as shown on figure 7.5 (blue dotted line). The Kelvin Helmholtz like contribution to the potential fluctuations in the SOL are identified as a departure form this spectrum. The poloidal spectra of the potential fluctuations for the two simulations are shown on figure 7.5 for a core radial position, $r/a = 0.5$ and in the SOL close to separatrix $r/a = 1.01$. In

the core, only the large scale modes $m \lesssim 5$ have significant amplitude. They correspond to the initial reorganization phase with GAMs. In the SOL the spectrum of potential fluctuations departs from the limiter one at high mode number, for $m > 60$ in the marginal case and for $m > 110$ in the experimental case. This range of poloidal modes is comparable to that of the small scales instability eddies identified on Figure 7.4. In the marginal case the SOL spectrum amplitude level-off around 10^{-4} for $m > 75$. There the spectrum amplitude exceeds the respective core one of ~ 10 orders of magnitudes. In such a situation, the instability appears to cascade to the smallest possible mode, which would be indicative on resolution issues. These have indeed been experienced requiring to run higher resolution simulations, such that at the highest mode numbers, $m \geq 200$, the spectrum decreases again with mode number. In the experimental case, the SOL spectrum amplitude is lower than the marginal case from two to four orders of magnitude in the range $m > 75$ and does not saturate on a given amplitude. This difference of behavior can be explained by the lower instability drive, that is the $E \times B$ shear.

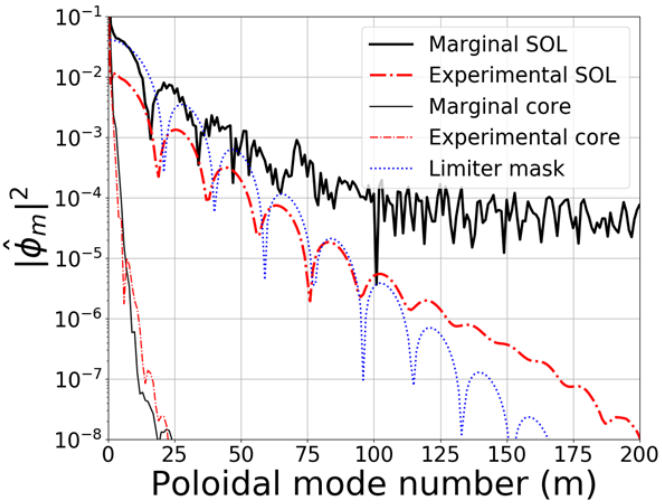

Figure 7.5: Poloidal spectrum of ϕ at time $t = 4 \cdot 10^3 \Omega_i^{-1}$ for the two simulations. The spectra are shown at two radial positions: in the core at $r/a = 0.5$ and in the SOL at $r/a = 1.01$. In blue dotted line is the Fourier spectrum of the limiter mask at $r/a = 1.01$.

We show the time evolution of the SOL Fourier spectrum for the marginal case in figure 7.6. For small modes $m < 60$, the spectrum is dominated by the constant projection of the limiter shape in the Fourier space. The largest modes $150 < m < 200$ are excited for $t > 2.5 \cdot 10^3 \Omega_i - 1$ and propagate in time towards smaller modes. The behavior is characteristic of the Kelvin-Helmholtz instability with very narrow shear layers, such that all wave lengths smaller than the shear layer width are destabilized. Noteworthy, in the trace of the amplitude, Figure 7.6 is both the patterns that appear in the generation of the spectrum, indicating specific mode coupling processes, and the fact that the broad spectra are not steady state feature. Finally, we recall that we have had to increase the poloidal resolution so that the smallest structure is properly resolved.

From the results presented in this section we understand that a Kelvin-Helmholtz-like instability may be generated by an enhanced $E \times B$ shear at separatrix when coupling core and SOL dynamics. The phenomenon is enhanced for increased velocity shear. Given this result, one is led to question the soundness of a SOL models when assuming only

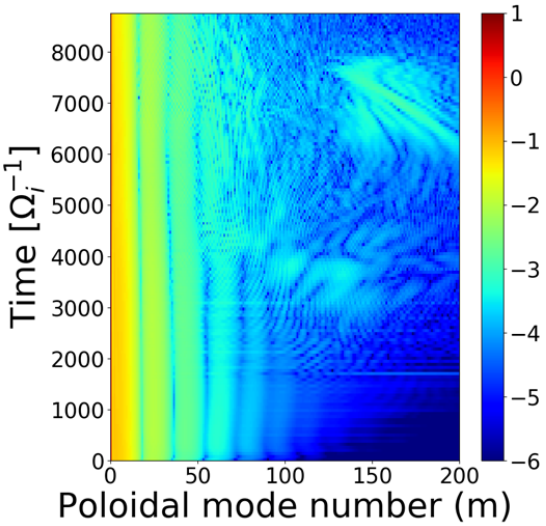

Figure 7.6: Time evolution of the poloidal spectrum of potential fluctuations in the SOL $r/a = 1.01$ for the marginal case.

neoclassical transport [69].

7.2 Edge subcritical turbulence, the crucial role of the SOL boundary layer

There is a long standing evidence from experimental measurements that the fluctuation intensity, measured by the relative density fluctuations $\delta n/n$, increases with radius from the core towards the SOL [70, 71]. However, recovering this result in simulations has proven more challenging[72]. While many results from both local [73, 74] and global [75] gyrokinetic models for various radial position in the deep core have shown agreement with the experimental turbulence and transport levels, a systematic under-prediction of both turbulence intensity and heat flux is found when approaching the edge [76]. The same paper, identifies a possible explication for this mismatch in non-local effects and self-consistent fast beam ions [76]. More recently, works with the GENE code have attributed the underestimation of the edge transport to the stiffness of transport in terms of the ion temperature gradient. The latter have been modified within the uncertainties of experimental measurements to achieve a better agreement on the edge transport levels [77, 78]. This sensitivity is problematic for any kind of extrapolation since projected core temperatures will vary considerably when driving fluxes are changed very little. In the extreme case, simulations would become irrelevant altogether for any projection.

We propose here a different understanding of the problem based on the role of realistic SOL boundary conditions. We show the results of GYSELA simulations with the limiter boundary condition where the presence of the open field line region makes the edge unstable, due to a combined effect of local linear instability and turbulence spreading.

We compare two simulations where only for the radial outer boundary conditions differ. The first version of the boundary is poloidally symmetric. The heat is extracted by a Krook restoring force, which acts in the same way at all poloidal locations[79]. A minimal version of the SOL is modeled by restoring the distribution function towards exponential

density and temperature profiles, the typical shape observed in experiments. However, turbulent transport decreases promptly for $r/a > 1$ and no shear layer appears to develop at the separatrix. The second simulation is the same as described in Section 6.1 with the new SOL-like boundary. The two simulations are run close to the "experimental" set-up discussed above. Except for the boundary, the two simulations have the same control parameters, same initial profiles shown on figure 7.2, adiabatic electrons and single ion species, namely deuterium. The aspect ratio is $A = 3.2$, $\rho_* = 1/316$ and collisionality $\nu_* = 0.24$.

We compute a synthetic diagnostics on the turbulent fluctuations $\delta n/n$ averaging the fluctuations of the electric potential on a poloidal arc of 8° around the outer midplane, according to features of reflectometer measurements on Tore Supra [80]. On figure 7.7 we show the the radial behavior of the experimental measurements for the root mean square of $\delta n/n$ fluctuations together with the synthetic diagnostics for the two simulations. When the poloidally symmetric boundary is considered (gray line), the turbulence intensity decreases when approaching the edge for $r/a > 0.6$. A stable region is found for $r/a > 0.8$, which indicates that the considered set of profiles is subcritical for the ITG instability in that region. The situation is changed for the simulation with limiter boundary (red line). In this case, the turbulence intensity monotonically increases with the radial direction, qualitatively matching the experimental trend.

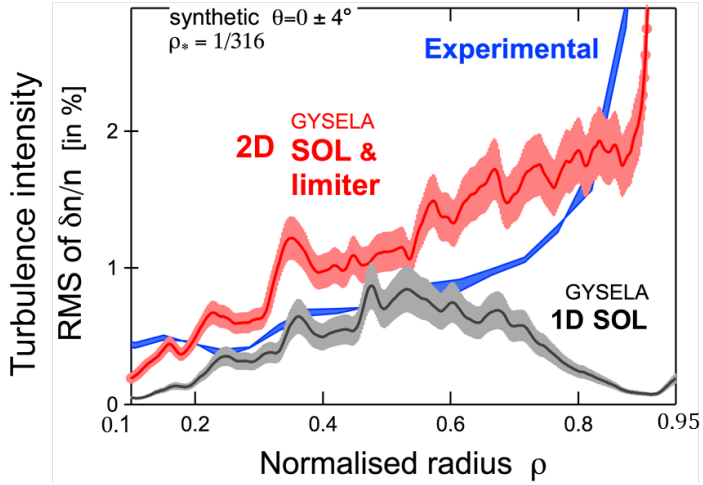

Figure 7.7: Synthetic diagnostic of the turbulent intensity, measured as the root mean square of $\delta n/n$ fluctuations versus the radial direction. The experimental measurements in blue, GYSELA simulation with poloidally symmetric boundary in gray and with limiter boundary in red.

The development of the turbulent patterns leading to the onset of fluctuations in the edge can be the result of the combination of many phenomena in the system. We identify two possible mechanisms that can generate fluctuations: from one side the profiles can become linearly unstable to ITG modes. Otherwise as shown in section 7.1, fluctuations can be generated by a Kelvin-Helmholtz instability of the shear layer close to the separatrix. Once the instability is generated, turbulence can spatially propagate from an unstable towards a linearly stable region. This phenomenon is called turbulence spreading[81]. It is still matter of scientific discussion whether the turbulence spreads mainly outward, from the ITG linearly unstable core [82], or inward [83, 84] from the highly turbulent SOL. Our

result stands in between: indeed when fluctuations start appearing in the edge, around $t = 40000\Omega_i^{-1}$, the SOL region is still in the initial reorganization phase described in Section 6.1 and does not exhibit any turbulent activity. Also, the formation of a transport barrier between the confined and open field lines regions impedes the transport in both radial directions. On the other hand, turbulence spreading from the core does not appear sufficient for turbulence to bridge the core to the separatrix in the simulation with the poloidally symmetric boundary. The change in behavior of the fluctuations level in the edge thus appears to be determined by the boundary layer properties. Further investigation is ongoing to clarify the role of the sheared radial electric field on the turbulent state. However a situation in which turbulence is well extended from the core all across the radial direction up to the SOL region is still to be achieved.

Summary

The SOL-like boundary implemented in GYSELA revealed a possible additional mechanism of turbulent fluctuation generation. The sheared poloidal flows driven by the reversed radial electric field in the vicinity of the separatrix can become unstable such as in the Kelvin-Helmholtz fluid instability. The new boundary condition is found determinant to recover the experimental trend of fluctuations level in the edge. These results suggest that a complete global description of the plasma system should include the interplay between confined and open field line regions.

Chapter 8

Summary and conclusions

This work aims to address the issue of the global non-linear effects of plasma micro-turbulence on confinement performance of Tokamak plasma. GYSELA global and flux-driven gyrokinetic simulations have been used as investigation tool, which allow for comparison between local and global properties of turbulent transport. We have focused in particular on two global aspects: the confinement time scaling of Ion Temperature Gradient turbulence in the confined region and the effect of a reduced SOL physics on the development of turbulence in the confined region.

GYSELA gyrokinetic and flux-driven simulations with poloidally symmetric boundary show that the steady state of ITG turbulence in the plasma core exhibits global similarity properties for which it is reasonable to define a scaling law of the energy confinement time. However the scaling is not reproduced at local spatial and time scales since the local correlation time and length of turbulent fluctuations does not scale the same as the global energy confinement time. The scalability properties seem to break at the mesoscale level. This fact could suggest that phenomena such as avalanches or staircases of mesoscale typical size have an impact on the scaling of turbulent heat transport. The simulations in the scaling are run on the same values of internal energy normalized to the radius. A power law scaling has been recovered over the remaining free dimensionless parameters: the aspect ratio $A = R_0/a$, the ratio major to minor radius of the toroidal plasma, the plasma size as the ion Larmor radius normalized to the minor radius $\rho_* = \rho_i/a$ and the plasma collisionality ν_*. It is found that the parallel connection time scales linearly on the aspect ratio $\tau_\parallel \propto A$. The aspect ratio exponent is found positive and close to 1, which suggests the influence of the parallel motion on this scaling. The exponent related to the plasma size scaling is found in between 2.5 and 3, indicating that the heat transport in the system is more efficient than in a purely diffusive regime, such as the Gyro-Bohm. The plasma size exponent is comparable with the experimental scaling of high confinement modes discharges. The collisionality scaling is found negative and weak, in line with the neoclassical theory predictions. The validity of the choice of a power law as the basis function for the linear regression process is found to be questionable.

The influence of the boundary has been investigated by introducing a reduced version of the Scrape-Off Layer in GYSELA numerical simulations. Two of the main SOL properties have been included in the code in separate steps: at first, poloidal asymmetry is given to the radial outer boundary with a dedicated penalization technique, which mimics the presence of the limiter and the first wall by locally enforcing a cold temperature. The limiter and first wall act as self-consistent heat sink: only the heat that reaches the

boundary is extracted. The poloidal asymmetry of the boundary enhances the parallel heat loss. This property characterizes the Scrape-Off Layer where, unlike in the plasma core, the transport is essentially 2D. The parallel transport in the SOL is verified via the initial propagation of a cold front from the limiter sides. Regarding the particle transport, the initialization of a poloidally uniform distribution function together with the limiter shaped heat sink leads to a reorganization of the SOL density both from the parallel and transverse directions. From the parallel side a phenomenon alike condensation takes place along the field line. From the transverse direction, the accumulation of density is due to the difference between the fast ∇B and curvature drifts from the core and SOL regions and the slow parallel motion inside the immersed boundary.

The second fundamental property of the SOL derives from the parallel electron dynamics in the open field lines region. The parallel jump of the electric potential at the plasma-wall interface proportional to the electron temperature, has been introduced by penalizing the quasi-neutrality equation. Consequently, the limiter and first wall regions are grounded in order to mimic the electric configuration of the SOL. The development of an average potential on the flux surfaces has been studied in both the core region only and coupled to the SOL. In the core, the radial shape of the average potential can be interpreted as the combination of negative and concave parabolic functions. A preliminary and completely data driven analysis shows that the potential well all across the radius is deeper for increased confinement regime, i.e. when decreasing either the normalized Larmor radius ρ_* or the plasma collisionality ν_*. This result suggests that the plasma confinement could be interpreted with the simple picture of a single pendulum: the deeper the potential well, the more difficult is for particles to escape. When coupling the core and SOL regions, the radial slope of the average electric potential is reversed at separatrix and a reversed radial electric field is self-consistently generated in GYSELA simulations. This effect seems sufficient to trigger the formation of a transport barrier at the core-SOL interface. The formation of the barrier appears to be independent on the choice for the SOL radial electric field, suggesting that the sole presence of any prescribed mean value for the radial electric field close to the simulation boundary is sufficient to trigger a transport barrier.

With the new SOL-like boundary condition an initial transient is started in the SOL region due to the combination of effects such as the parallel propagation of a cold front in the SOL, the condensation towards the limiter, the development of a $E \times B$ shear layer at separatrix introduced with the penalization technique. In particular, the condensation effect towards the limiter coupled to the negative $E \times B$ poloidal flows in the SOL result in a poloidally asymmetric distribution of the SOL density. The poloidally localized overdense region polarizes the SOL. Also the initial parallel propagation of a cold front from the limiter edges combined to the formation of a transport barrier close to separatrix cools down the SOL. Poloidal asymmetries on the temperature distribution are much weaker than the one on the density. A steady state turbulent regime for the SOL still needs to be achieved and modification in the poloidal temperature distribution can be introduced by the ballooned structures of the fluctuations. The conservation of particles has been tested in the GYSELA simulations with limiter boundary. Preliminary results indicate a non negligible influence of the collision operator as well as the loss of phase space conservation. Further tests are going to be addressed to clarify the influence of the latter. However, quantifying the impact of this error on the physics modeled is challenging and remains an open issue of this work.

Anyhow, the SOL-like boundary condition gives access to additional phenomena happening in the plasma edge close to the separatrix. We remind here the two outstanding results brought to light by the limiter boundary condition. *(i)* The enhanced poloidal velocity shear layer generated at the interface between the core and SOL regions can give rise to an instability close to separatrix which seems similar in nature to the Kelvin-Helmholtz instability and could contribute as a turbulence generation mechanism in the SOL. This result questions the accuracy of drift based descriptions of the SOL heat transport. *(ii)* The presence of the SOL boundary condition allows for turbulence development in the subcritical edge region so that the experimental behavior of turbulent fluctuations in the radial direction is qualitatively recovered.

The results presented in this work point out two main messages that should be considered in future research:

- given the clear breakdown of the similarity properties at the mesoscale level, global models are more appropriate for confinement predictions of future machines.
- the global models should include the interplay between the three regions of core, edge and SOL to properly treat the boundary effects.

As well, this work reports some fundamental unsolved questions, to be addressed in future works:

What is the physics behind the similarity properties and why they are not reproduced at smaller scales? This issue could be at first addressed by planning a rigorous comparison of large and small scales properties of turbulence between local (quasi-linear, δf, flux-tube, gradient-driven) and global (full-f gyrokinetic) models. As a starting point one could address the differences in the near critical behavior of the system, quantifying the impact of mesoscale phenomena such as the avalanches and staircases on the global confinement. Comparison with experimental data would be mandatory in order to validate the results. For this purpose, the development of accurate synthetic diagnostics is required to compare numerical results to the experimental data.

What is the role of the mean electric potential, or alternatively the radial electric field, on confinement? To answer this question, one could take advantage of the now mature techniques of data analysis and address a data-driven study on the terms constituting the force balance equation on the basis of full-f simulations. In a fully-turbulent regime these terms non-linearly interplay between each other and the physical mechanisms leading the interplay are still to be identified. The enlightening of correlations between the terms of the force balance in the 3D real space and in time could help identifying the causality mechanisms behind their evolution. The work should be supported by theoretical considerations on the possible generation mechanisms at play.

Appendix A

Difference between the flux coordinates and the toroidal coordinates in GYSELA

In this appendix we detail the differences between the two possible system of coordinates in a Tokamak: the flux coordinates $(\chi, \theta^*, \varphi)$ and the toroidal coordinates (r, θ, φ). In the first, the coordinate χ is the label of the flux surfaces and is related to the radial coordinate. The poloidal angle θ_* is defined in such a way that the safety factor q depends only on the coordinate χ. The second is the geometrical system of toroidal coordinates.

The GYSELA magnetic configuration is defined as:

$$\mathbf{B} = B_\theta \mathbf{e}_\theta + B_\varphi \mathbf{e}_\varphi \tag{A.1}$$

where $B_\theta = B_0 r/R\bar{q}$ and $B_\varphi = B_0 R_0/R$. Here B_0, R_0 are the magnetic field on the magnetic axis and the major radius of the torus, R is the distance from the magnetic axis

$$R(r, \theta) = R_0 + r cos(\theta) \tag{A.2}$$

The vectors $\mathbf{e}_\theta = r\nabla\theta, \mathbf{e}_\varphi = R\nabla\varphi$ are the unit vectors on the poloidal and toroidal directions respectively. $\bar{q}$ is a radial function.

The safety factor of the Tokamak magnetic configuration is defined as

$$q(r) = \frac{1}{2\pi}\int_0^{2\pi} \frac{\mathbf{B}\cdot\nabla\varphi}{\mathbf{B}\cdot\nabla\theta} d\theta = \frac{\bar{q}(r)}{2\pi}\int_0^{2\pi} \frac{1}{1+\epsilon cos(\theta)} d\theta \tag{A.3}$$

with $\epsilon = r/R_0$. One can separate the integral in two parts, the first between $0 < \theta < \pi$, the second between $\pi < \theta < 2\pi$.

$$\begin{aligned} I_1 &= \int_0^{\pi} \frac{1}{1+\epsilon cos(\theta)} d\theta \\ I_2 &= \int_{\pi}^{2\pi} \frac{1}{1+\epsilon cos(\theta)} d\theta \end{aligned} \tag{A.4}$$

To resolve the first integral, one can perform the following substitution:

$$t = tan\Big(\frac{\theta}{2}\Big) \qquad cos(\theta) = \frac{1-t^2}{1+t^2} \qquad dt = \Big(\frac{1+t^2}{2}\Big) d\theta \tag{A.5}$$

and use the formula

$$\int \frac{dx}{a^2 + b^2x^2} = \frac{1}{ab} tan^{-1}\Big(\frac{bx}{a}\Big)$$

Then

$$I_1 = 2\int_0^{tan(\theta/2)} \frac{1}{1+\epsilon+(1-\epsilon)t^2} dt = 2\Big[\frac{1}{\sqrt{1-\epsilon^2}} tan^{-1}\Big(\frac{\sqrt{1-\epsilon}}{1+\epsilon}t\Big)\Big]_0^{\infty} = \frac{\pi}{1-\epsilon^2} \tag{A.6}$$

For the second integral I_2 we substitute $u = \theta - \pi$ and we follow the same procedure, resulting in

$$I_2 = 2\int_0^{\pi} \frac{1}{1+\epsilon cos(u)} du = 2\Big[\frac{1}{\sqrt{1-\epsilon^2}} tan^{-1}\Big(\frac{\sqrt{1+\epsilon}}{1-\epsilon}t\Big)\Big]_0^{\infty} = \frac{\pi}{1-\epsilon^2} \tag{A.7}$$

Combining A.6 and A.7 into A.3 we obtain the relation between the safety factor and the radial function $\bar{q}(r)$

$$q(r) = \frac{\bar{q}(r)}{\sqrt{1-\epsilon^2}} \tag{A.8}$$

One can determine the relation between θ and θ^* by writing the equality

$$\frac{d\theta^*}{d\theta} = \frac{\mathbf{B}\cdot\nabla\theta^*}{\mathbf{B}\cdot\nabla\theta} = \frac{1}{q}\frac{\mathbf{B}\cdot\nabla\varphi}{\mathbf{B}\cdot\nabla\theta} = \frac{\bar{q}}{q}\Big(\frac{1}{1+\epsilon cos(\theta)}\Big) = \frac{\sqrt{1+\epsilon^2}}{1+\epsilon cos(\theta)} \tag{A.9}$$

By applying the substitution method A.5 on the integral of equation A.9 one finds the following relations:

$$\begin{aligned} \theta &= 2tan^{-1}\Big(\frac{\sqrt{1-\epsilon}}{\sqrt{1+\epsilon}} tan\Big(\frac{\theta^*}{2}\Big)\Big) \\ \theta^* &= 2tan^{-1}\Big(\frac{\sqrt{1-\epsilon}}{\sqrt{1+\epsilon}} tan\Big(\frac{\theta}{2}\Big)\Big) \end{aligned} \tag{A.10}$$

These relations allow the transformation between the toroidal coordinates and the flux coordinates.

Appendix B

Linear regression method used for the energy confinement time scaling

In this Appendix we show the method we have applied to fit the distribution of points of the energy confinement time in function of the simulation parameters. This method is described in detail in [85], chapter 15.

The problem is to fit a distribution of N points y_i with error σ_i on the measure and coordiante x_i to a straight line function $y(x) = a + bx$. We define the chi-square function

$$\chi^2(a,b) = \sum_{i=1}^{N} \left(\frac{y_i - a - bx_i}{\sigma_i} \right) \tag{B.1}$$

which measures the distance of the points from the merit function $y = a + bx$. The maximum likelihood fit is obtained by minimizing the χ^2 function with respect to the coefficients a and b. We derive the function χ^2 with respect to a and b and we seek for the point in which the derivative vanishes.

$$\begin{aligned} 0 =& \frac{\partial \chi^2}{\partial a} = -2 \sum_{i=1}^{N} \frac{y_i - a - bx_i}{\sigma_i^2} \\ 0 =& \frac{\partial \chi^2}{\partial b} = -2 \sum_{i=1}^{N} \frac{x_i (y_i - a - bx_i)}{\sigma_i^2} \end{aligned} \tag{B.2}$$

By defining the following sums:

$$\begin{gathered} S = \sum_{i=1}^{N} \frac{1}{\sigma_i^2} \qquad S_x = \sum_{i=1}^{N} \frac{x_i}{\sigma_i^2} \qquad S_y = \sum_{i=1}^{N} \frac{y_i}{\sigma_i^2} \\ S_{xx} = \sum_{i=1}^{N} \frac{x_i^2}{\sigma_i^2} \qquad S_{xy} = \sum_{i=1}^{N} \frac{x_i y_i}{\sigma_i^2} \end{gathered} \tag{B.3}$$

the conditions B.2 can be rewritten as

$$\begin{aligned} aS + bS_x =& S_y \\ aS_x + bS_{xx} =& S_{xy} \end{aligned} \tag{B.4}$$

This is a linear system in the unknown a, b. By inverting the system one gets the following expressions:

$$\begin{aligned} a =& \frac{S_{xx}S_y - S_x S_{xy}}{SS_{xx} - (S_x)^2} \\ b =& \frac{SS_{xy} - S_x S_y}{SS_{xx} - (S_x)^2} \end{aligned} \tag{B.5}$$

We compute the statistical error $\sigma_{a,b}$ on the coefficients a and b by using the following relation

$$\sigma_g^2 = \sum_{i=1}^{N} \sigma_i^2 \Big(\frac{\partial g}{\partial y_i}\Big)^2 \tag{B.6}$$

This relation derives from consideration on the error propagation, but its physical meaning is not straightforward. Note that to compute the error on the coefficients, an analytical expression of the coefficients in function of the ordinates y_i is needed. The derivative of the coefficients a and b with respect to y_i reads:

$$\begin{aligned} \frac{\partial a}{\partial y_i} =& \frac{S_{xx} - S_x x_i}{\sigma_i^2 (SS_{xx} - (S_x)^2)} \\ \frac{\partial b}{\partial y_i} =& \frac{Sx_i - S_x}{\sigma_i^2 (SS_{xx} - (S_x)^2)} \end{aligned} \tag{B.7}$$

so that summing over the points we get the standard deviation on the coefficients a, b

$$\begin{aligned} \sigma_a^2 =& \frac{S_{xx}}{SS_{xx} - (S_x)^2} \\ \sigma_b^2 =& \frac{S}{SS_{xx} - (S_x)^2} \end{aligned} \tag{B.8}$$

Multiparameter scaling

One can consider a fitting depending on more than one parameter, that is more than one x coordinate. In this case, one can rewrite the merit function as

$$y = a + \bar{\mathbf{b}} \cdot \bar{\mathbf{x}} \tag{B.9}$$

where $\bar{\mathbf{x}}$ is the vector of the dependence parameters and $\bar{\mathbf{b}}$ is the vector of the respective coefficients. The values of the coefficients a and $\bar{\mathbf{b}}$ can be extracted following the same procedure as before. However the linear system to solve is of higher rank. In the case of fitting the points with a straight line on more than one dimension one cannot derive an analytical expression of the parameters and therefore one cannot use the expression B.6 to compute the error on the resulting coefficients.

Appendix C

Difference between the application of an infinite penalization and a large Krook restoring force

We detail here the difference in the numerical application of an infinite penalization as described in Section 4.1.2 and a very strong restoring force of the Krook type.

The numerical algorithm of GYSELA [39] includes a time-splitting technique which allows to solve the time advance due to each operator of Vlasov equation separately. Thus the equation for the Krook term corresponds to

$$\partial_t f = -\nu M(r,\theta)(f - ng) \tag{C.1}$$

To numerically handle $\nu \to \infty$ one possible choice is to apply a standard Krook term with a very large ν. However for increasing ν the shape of the coefficient $\tilde{\nu}(x) = \nu M(x)$ is close to a step function, which can lead to numerical instabilities. In this case, one should first define the maximum gradient numerically acceptable for the function $\tilde{\nu}(x)$ and next, given the restoring force strength ν, recover a modified mask function $\tilde{M}(x) = \tilde{\nu}(x)/\nu$ to use in the restoring force term. Instead, the following alternative approach can be pursued: at each time step Δt, inside the limiter and wall region, the distribution function is fully replaced by its target value g as

$$f(t + \Delta t) = (1 - M(x))f(t) + M(x)g \tag{C.2}$$

This formula differs from the application of a standard Krook term with very large but finite ν only in the transition region, where $0 < M(x) < 1$. We show the proof Hereafter. The equation for the Krook term solved by GYSELA corresponds to

$$\partial_t f = -\nu M(f - g) \tag{C.3}$$

Where we substitute $\nu M(x) = \tilde{\nu}(x)$, allowing a spatial dependence of the restoring force strength which does not depend directly on the mask function. The analytical solution of this equation over a time step of amplitude Δt, corresponding to the time step of one iteration, is

$$f(t + \Delta t) = f(t)e^{-\tilde{\nu}(x)\Delta t} + g(1 - e^{-\tilde{\nu}(x)\Delta t}) \tag{C.4}$$

After k iterations the solution becomes

$$f(t + k\Delta t) = f(t)e^{-\tilde{\nu}(x)k\Delta t} + g(1 - e^{-\tilde{\nu}(x)k\Delta t}) \tag{C.5}$$

On the other hand, when applying an infinite penalization as in equation C.2, the spatial dependence of the restoring force is given by the mask $M(x)$ only. After k iterations

$$f(t + k\Delta t) = (1 - M(x))^k f(t) + (1 - (1 - M(x))^k)g. \tag{C.6}$$

The results C.5 and C.6 are equivalent if

$$-\tilde{\nu}(x)\Delta t = log(1 - M(x)) \tag{C.7}$$

The right hand side of Equation C.7 does not depend on time step Δt or restoring force strength ν, as opposed to the left hand side. Thus in the case of infinite penalization as in equation C.2 the effective strength of the restoring force is $\tilde{\nu}(x) = log(1 - M(x))/\Delta t$ and depends on the time step Δt. Substituting $\tilde{\nu}(x) = \nu\tilde{M}(r, \theta)$ in the relation C.7 we distinguish three different cases: (i) the case $M(x) = 0$ corresponds to $\nu = 0$ and the restoring force is not active in both the formulations; (ii) in the case $M(x) = 1$ the relation C.7 exactly gives the limit $\nu \to \infty$; (iii) the case $0 < M(x) < 1$, and so $0 < \tilde{\nu}(x) < \nu$, is restricted to a narrow region $\sim 5\rho_i$ and corresponds to the only difference between the two methods. Hence, the formulation C.2 can be preferred to the application of a very strong Krook term when one would enforce the limit $\nu \to \infty$, taking into account that the effective restoring force strength depends on the time step only in the narrow transition region.

Appendix D

Time evolution of the density, flux and energy in the $1-D, 1-V$ penalized model

In order to provide a better understanding of the cold spot effect on the evolution of the system, we derive in the following an analytical expression for the time evolution of the moments of the distribution function inside the plasma region, where only the advection term is active, responsible for the propagation of the two fronts v_+ and v_- described in Section 4.2.1. The model does not take into account the evolution of the distribution function within the limiter region. The main interest is in the understanding of the density and temperature behavior when the heat sink drives transport in the parallel direction. In the initial phase, in fact, a fast particle flux towards the limiter empties the SOL. The decreasing of the temperature is not linear, as a result of the front propagation in the phase space.

The moments M_k of order k of the distribution function can thus be computed as the sum of three integrals in velocity space, namely:

$$M_k = \int_{-\infty}^{v_-} n_C f_C(v) v^k dv + \int_{v_-}^{v_+} n_H f_H(v) v^k dv + \int_{v_+}^{\infty} n_C f_C(v) v^k dv \tag{D.1}$$

The first integral accounts for the cold distribution function transported by the front v_-, hence it spans from $-\infty$ to v_- in velocity space; the second integral accounts for the initial hot distribution function, thus between v_- and v_+ in velocity space; the last integral accounts for the cold distribution function transported by the front v_+ and it is calculated from v_+ to $+\infty$ in velocity space.

Considering an infinite restoring force $\nu \to \infty$, thus a step mask function, one can neglect the periodic propagation of the front in velocity space. The analytical solutions for the density, particle flux and energy are therefore:

$$n(x,t) = n_C + \frac{n_H}{2} erf\left(\frac{v}{\sqrt{2T_H}}\right)\Bigg|_{v_-}^{v_+} - \frac{n_C}{2} erf\left(\frac{v}{\sqrt{2T_C}}\right)\Bigg|_{v_-}^{v_+} \tag{D.2}$$

$$\Gamma(x,t) = n_C \sqrt{\frac{T_C}{2\pi}} e^{\frac{-v^2}{\sqrt{2T_C}}}\Bigg|_{v_-}^{v_+} - n_H \sqrt{\frac{T_H}{2\pi}} e^{\frac{-v^2}{\sqrt{2T_H}}}\Bigg|_{v_-}^{v_+} \tag{D.3}$$

$$\mathcal{E}(x,t) = T_C + \left[\frac{T_H}{2} erf\left(\frac{v}{\sqrt{2T_H}}\right) - \sqrt{\frac{T_H}{2\pi}} v e^{-\frac{v^2}{2T_H}}\right]_{v_-}^{v_+} - \left[\frac{T_C}{2} erf\left(\frac{v}{\sqrt{2T_C}}\right) - \sqrt{\frac{T_C}{2\pi}} v e^{-\frac{v^2}{2T_C}}\right]_{v_-}^{v_+} \quad \text{(D.4)}$$

The expressions D.2, D.3, D.4 are valid only within the plasma region since we have considered only the advection term. These results exactly fulfill both the charge balance (Equation 4.6a) and the momentum balance (Equation 4.6b). Inside the limiter region the restoring force drives the distribution function to the actual density value $n(x,t)$ and both density and particle flux can evolve, as derived in the following on the basis of Equations D.2 and D.3. On the other hand, the energy density is fixed inside the limiter to the cold value $\mathcal{E}_C$, since we are considering an infinite penalization.

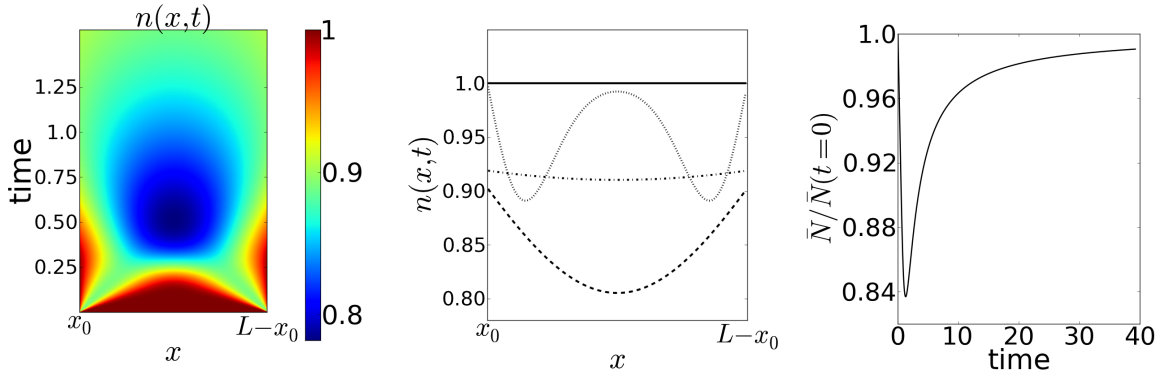

Figure D.1: *Left*: Spatial and time evolution of the analytical density in equation (D.2). *Centre*: Cut at time $t = 0$ (solid line), $t = 0.3$ (dotted), $t = 1.5$ (dashed), $t = 4$ (dash-dotted line). *Right*: Relative variation of the number of particles $\bar{N}(t)/\bar{N}(t=0) = \int_{x_0}^{L-x0} n(x,t)dx / \int_{x_0}^{L-x0} n(x,0)dx$ inside the plasma region.

Figure D.1 shows the analytical expression for the density in time and space, within the plasma region $x_0 < x < L - x_0$. An initial transient leads to a lowering of the density profile. At asymptotic time the error functions of Equation (D.2) are all flattened to zero and the density profile is constant and equal to the initial cold value n_C. The total number of particles inside the plasma region, which is the integral of $n(x,t)$ in the interval $[x_0, L-x_0]$ is shown in figure D.1-right: it decreases at the beginning of the transient and then tends asymptotically to the initial value. Given Equation (4.6a), the total number of particles $N = \int n dx$ in the system is conserved $\partial_t N = 0$. Hence, during the transient, the density increases inside the penalized region. This phenomenon is interpreted as condensation: the density tends to accumulate inside the cold region. When a constant density is initialized in the domain $n_C = n_H$, indeed, an initial pressure gradient is created in the system due to $T_C < T_H$. In steady state conditions the momentum balance equation within the plasma region reads $\nabla \Pi = 0$ so that during this initial transient the system adapts to reduce the pressure gradient.

The behavior of the particle flux mirrors the density: at the early beginning particles are moving towards the limiter to then redistribute much more slowly to the center. The reorganization of the density profile is indeed subject to two different time scales: the fast condensation inside the limiter is governed by the hot thermal velocity $v_{th_H} = \sqrt{T_H}$ of the

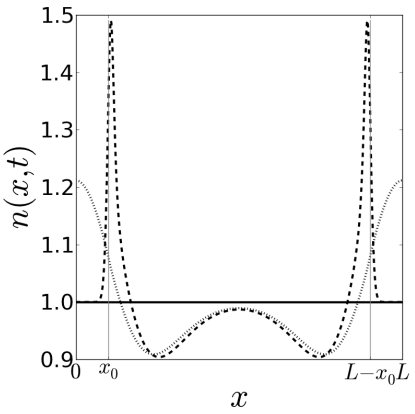

Figure D.2: Initial density profile (solid line). Density accumulation transient in the case of strong restoring force $\nu = 1000$ (dashed line) and weak restoring force $\nu = 0.5$ (dotted line).

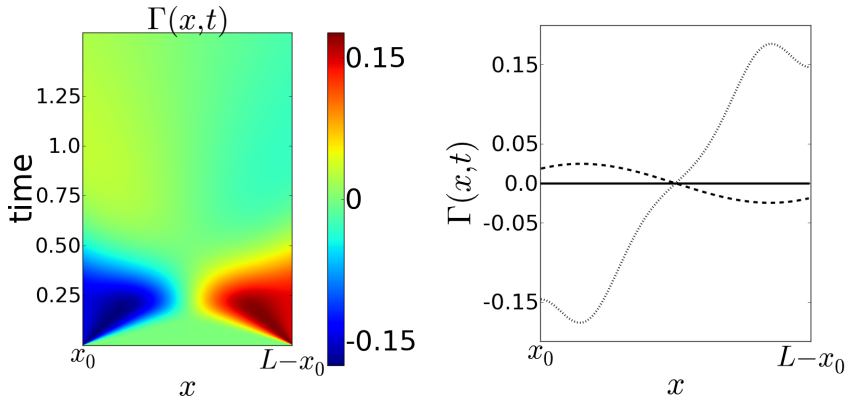

Figure D.3: *Left*: Spatial and time evolution of the analytical particle flux in equation (D.3). *Right*: Cut at time $t = 0.3$ (dotted), $t = 1.5$ (dashed).

plasma region. Conversely in the limiter, the temperature is cold so that the following redistribution of the density from the limiter towards the plasma region is governed by the cold thermal velocity $v_{th_C} = \sqrt{T_C} < v_{th_H}$. The effect of the restoring force within the limiter region is not taken into account in the analytical model. When Equation (4.5) is solved numerically, one can study the effect of the restoring force on the global density profile (figure D.2). The restoring force resists to the propagation of a higher density inside the limiter. When the restoring force is strong, indeed, accumulation of density is observed only at limiter sides, where $M(x) < 1$ weakens the restoring effect.

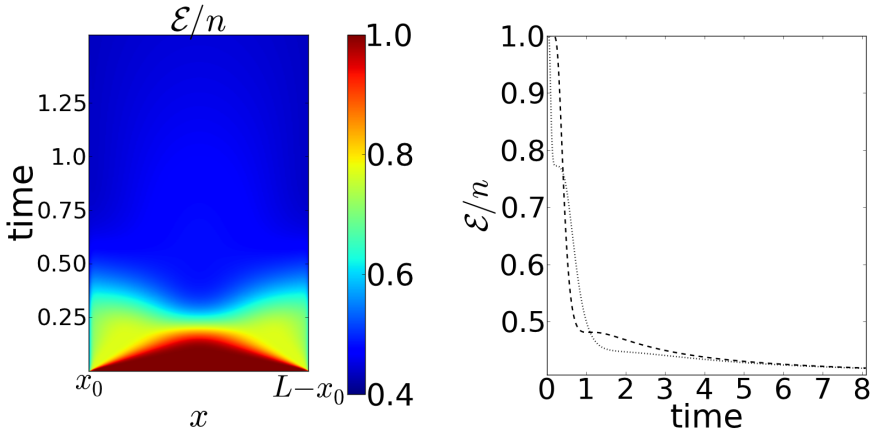

Figure D.4: *Left*: Spatial and time evolution of the temperature, computed as $\mathcal{E}(x,t)/n(x,t)$. *Right*: Cut at $x = 0.2$ (dotted line) and midbox $x = 1$ (dashed line).

The lowering of the temperature is not linear, as shown in figure D.4. This happens as a result of kinetic propagation of the cold front: the bulk of the distribution function is cooled down on much longer time scales than the tail. At first temperature decreases from both sides of the limiter towards an intermediate state. It corresponds to the situation when the tail of the distribution function in velocity space has already stepped to the cold value. Next the system is cooled at the limiter temperature starting from the region farthest from the limiter. This last process is governed by the slower time scales of the bulk velocities.

Appendix E

Charge balance equation in GYSELA

E.1 Particle conservation test

When the hot plasma comes in contact with the cold solid matter, charged particles recombine in neutrals and the plasma state is lost. The solid matter therefore acts as a sink for charged particles. Although the loss of particles is a natural and most important transport phenomenon in the SOL, this physics is not addressed in the current work with adiabatic electrons. Indeed when fixing the electron density, the quasi-neutrality equation imposes that the ion density must be conserved. As already introduced in the previous chapters, a mismatch between the number of ions and electrons on the flux surfaces would polarize the plasma, introducing a spurious electric field in the system which makes difficult the interpretation of the results. Since there is not any particle source in the model, a particle sink must not be admitted, and vice-versa.

We identify some of the causes that could lead to loss of particle conservation in GYSELA simulations:

- inaccuracy of the numerical computation of the integral of the distribution function giving the density due to a lack of resolution in velocity space. This effect could be increased if the local temperature decreases, for example in the SOL.

- Lack of resolution in the poloidal plane to correctly resolve the transition $0 \rightarrow 1$ of the penalization mask. This region is critical during the initial SOL transient, given the fact that particles tend to accumulate at the plasma-limiter interface.

- Breakdown of the phase space conservation within the mask transition $0 \rightarrow 1$ due to the artificial suppression of the drift velocities within the penalized region. The divergence of the drifts velocities locally increases, leading to an error on the formulation of the conservative form of the gyrokinetic equation.

- Inaccuracy of the particle conservation due to the formulation of the collision term, which can loose its validity in high collisionality regime[25], therefore when approaching the separatrix. This becomes especially important when applying the collision term on a sparse time step (with accordingly increased collisionality), i.e. a multiple of the main time step of the advection algorithm, in order to save computational resources. Here, tests are done with the collision operator being called every eight numerical time steps; in each of these steps, collisionality is thus eight times the nominal one

- Breakdown of the gyro-average procedure when the Larmor orbit hits the simulation boundary.

In general, the particle conservation cannot be perfectly satisfied in numerical simulations. It has already been tested that an acceptable velocity mesh size to resolve the velocity integrals, even at low temperature as $0.1T_{r/a=0.5}$ corresponds to $N_{v_\parallel} = 128$ and $N_\mu = 64$. On the same mesh size the collision operator has been shown to conserve the particles up to $7 \cdot 10^{-7}$ relative error on the entire plasma volume [25]. This test is performed over approximatively one collision time and without considering the particle trajectories. The attribution of a physical meaning to such a number and in general the quantitative evaluation of the impact of any loss of particle conservation on the physics modeled is still an open issue for such global numerical simulations.

We measure the volumetric error on the particle conservation for GYSELA simulations when including the limiter boundary. At first approximation, one can write the error on particle conservation by integrating the gyrokinetic Vlasov equation in velocity space. The error takes the following form

$$\varepsilon = \partial_t n_{GC} + \nabla \cdot \mathbf{\Gamma}_{GC} \tag{E.1}$$

hence it can be measured as the time variation of the density summed to the spatial divergence of the particle flux. To compute the particle balance from the GYSELA results, the quantities in equation E.1 are referred to the gyro-centers. The gyro-center flux can be written as the sum of four components

$$\mathbf{\Gamma}_{GC} = \mathbf{\Gamma}_{v_E} + \mathbf{\Gamma}_{v_D} + \mathbf{\Gamma}_{v_\parallel} + \mathbf{\Gamma}_J \tag{E.2}$$

where

$$\mathbf{\Gamma}_{v_D} = \int \mathbf{v}_D f_{GC} d\bar{v} \tag{E.3a}$$

$$\mathbf{\Gamma}_{v_E} = \int \mathbf{v}_E f_{GC} d\bar{v} \tag{E.3b}$$

$$\mathbf{\Gamma}_{v_\parallel} = \int v_\parallel f_{GC} d\bar{v} \tag{E.3c}$$

$$\mathbf{\Gamma}_J = P_\parallel \frac{m_a}{q_a B^2} \boldsymbol{\nabla} \times \boldsymbol{B} \tag{E.3d}$$

$$P_\parallel = \int \left(v_\parallel - u(r,\theta,\varphi)\right)^2 f_{GC} d\bar{v} \tag{E.3e}$$

$$n(r,\theta,\varphi) = \int f_{GC} d\bar{v} \tag{E.3f}$$

$$u(r,\theta,\varphi) = \frac{1}{n(r,\theta,\varphi)} \int v_\parallel f_{GC} d\bar{v} \tag{E.3g}$$

where $d\bar{v}$ is the volume element in velocity space, namely $d\bar{v} = 2\pi B^*_\parallel m_i dv_\parallel d\mu$. The estimation of the order of magnitude of these terms is still an ongoing work.

We note that in the GYSELA model the right hand side of the gyrokinetic equation corresponds to the sum of the collision term $\mathcal{C}$, the heat source S_{heat} and the heat sink, namely the penalized Krook term. Also, when artificially suppressing the perpendicular drift velocities within the penalized region, the divergence of the drift flows is locally not null. The error ε should not be compared to zero but to the quantity

$$\begin{aligned}\varepsilon = &\int \mathcal{C} d\bar{v} + \int S_{heat} d\bar{v} \\ &+ \int (-\nu) M^{LIM}(r,\theta)\big(f - f_{target}\big) d\bar{v} \\ &+ \int \frac{1}{B^*_\parallel} f_{GC} \nabla \cdot \Big[M^{LIM}(r,\theta)\big(\mathbf{v}_E + \mathbf{v}_D\big)\Big] d\bar{v}\end{aligned} \tag{E.4}$$

The last two terms are introduced with the limiter boundary.

The error ε is averaged on the total volume of the plasma and is integrated on a time interval between $3 \cdot 10^4 \Omega_i^{-1}$ and $4 \cdot 10^4 \Omega_i^{-1}$. It is found that the volumetric average of the error considering the total volume of the plasma for the simulations with limiter boundary is of the order of $3 \cdot 10^{-7}$, comparable to the accuracy of the collision operator. We investigate the influence of the numerical resolution on the value of the volume averaged error. The test is performed on a reference simulation with reduced $1/\rho_* = 150$ for two main reasons:*(i)* on the same number of grid points the resolution on the poloidal plane is improved for a smaller poloidal section, *(ii)* since the radial transport is bigger in a smaller machine, we put ourselves in an unfavorable situation to quantify what is certainly an upper limit for the conservation error. The reference mesh size corresponds to $(N_r, N_\theta, N_\varphi, N_{v_\parallel}, N_\mu) = (256, 512, 64, 128, 64)$, the toroidal length is reduced to $L_\varphi = \pi/4$ with periodic boundary conditions. The time step of each iteration is $dt = 30\Omega_i^{-1}$, the diagnostics on the gyro-center density and the fluxes are saved every $60\Omega_i^{-1}$. We double one by one the number of points of each direction of the grid except ν. On a separate case we decrease the time step to $dt = 20\Omega_i^{-1}$, the saving time for the diagnostics is maintained the same. We also investigate the effect of the collision term by *(i)* reducing the collisionality by a factor of 100 or *(ii)* reducing the time step in which the collision operator is applied by a factor of 8, that is applying the collision operator each iteration. The resulting total error for all the simulations is summarized in table E.1. The average error on the total volume is found always negative, corresponding to a particle loss. Surprisingly the mean error on the total plasma volume increases of about 10% when either the spatial or the velocity resolution is doubled. Reducing the time step does not seem to affect the value of the error. The error is reduced of about 25% when decreasing the collisionality to $\nu_* = 0.0024$ while no significant effect is found when the collision operator is applied the collision operator every iteration.

To better locate the particle loss, we compute the error ε on different regions of the poloidal plane, indicated in figure E.1. We compute the percentage of the total error made in each region i as

$$\bar{\varepsilon} = \frac{|\langle \varepsilon_i \rangle|}{\sum_i |\langle \varepsilon_i \rangle|} \tag{E.5}$$

where the notation $\langle \cdot \rangle$ stands for the volume average and time integration operation. The separatrix region is responsible for $30\% - 50\%$ of the error made, followed by the wall interface region $20\% - 30\%$ and the limiter interface $10\% - 30\%$. Inside the limiter 1% to 5% of the total error made corresponds to particle loss. The volume averaged error $\langle \epsilon_i \rangle$ increases of about one to two orders of magnitude in the mask transition regions (limiter interface and wall interface) with respect to the total volume and to the other regions. This fact can be related to the loss of phase space conservation within the mask transition region. The most of the error seems to be made within the separatrix region. A further check should be addressed in order to fully confirm the results obtained with the limiter boundary. One should run two simulations more: the first is to check the influence of the loss of phase space conservation by allowing the transverse drifts in the limiter region while suppressing them only inside the poloidally symmetric wall region; the second is to check the influence of the quasi-neutrality penalization by removing the penalization from the Vlasov equation.

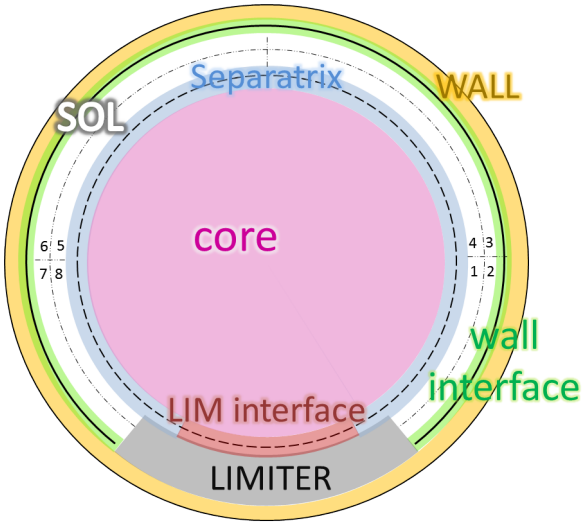

Figure E.1: Sketch of the different regions in the poloidal section considered to compute the error on the gyro-centers conservation. The core region extends between $r = 0$ and r_{sep}, where r_{sep} is the last radial position for which the limiter mask $M^{LIM}(r, \theta = 3/2\pi) = 0$. The separatrix and limiter interface regions extend radially over the transition $0 \to 1$ of $M^{LIM}(r, \theta = 3\pi/2)$. The limiter interface region extends poloidally between $1.475 < \theta/\pi < 1.525$ and corresponds to the tiny connection area between the last closed flux surface and the limiter. The limiter region extends radially between the first point satisfying $M^{LIM}(r, \theta = 3\pi/2) = 1$ to the last point satisfying $M^{LIM}(r, \theta = 0) = 1$ and poloidally between $1.3 < \theta/\pi < 1.7$; This region includes the whole limiter region, most of the transition region at the plasma-limiter interface as well as the plasma region closest to the limiter. The wall interface region is the poloidal sector of the transition $0 < M^{LIM}(r, \theta = 0) < 1$ which is not included in the limiter region, in the same way the SOL region, which radially extends between the separatrix region and the wall interface region. The wall region is the poloidally symmetric layer where $M^{LIM}(r, \theta = 0) = 1$.

N_r	N_θ	N_φ	$N_{v_\parallel}$	dt	ν_*		**core**	**Sep**	**LIMi**	**SOL**	**LIM**	**WALLi**	**WALL**	**TOT**
Percentage of the total volume:							62.5 %	2.62 %	0.18 %	21.95 %	6.15 %	3.05 %	3.48 %	100 %
256	512	64	128	30	0.24	$\langle\varepsilon\rangle$	-1.61e-07	2.10e-05	-2.17e-05	6.01e-08	-2.07e-06	-1.09e-05	-4.90e-08	-3.07e-07
						$\bar{\varepsilon}$	0.28 %	37.53 %	38.79 %	0.10 %	3.69 %	19.48 %	0.08 %	100 %
512	512	64	128	30	0.24	$\langle\varepsilon\rangle$	-1.67e-07	1.99e-05	8.43e-06	-2.57e-07	-1.84e-06	-1.08e-05	-1.69e-07	-3.56e-07
						$\bar{\varepsilon}$	0.40 %	47.8 %	20.2 %	0.61 %	4.42 %	26.0 %	0.40 %	100 %
512	1024	64	128	30	0.24	$\langle\varepsilon\rangle$	-1.42e-07	1.83e-05	-1.27e-05	-3.30e-07	-1.77e-06	-1.08e-05	-1.70e-07	-3.72e-07
						$\bar{\varepsilon}$	0.32 %	41.26 %	28.77 %	0.74 %	3.99 %	24.51 %	0.38 %	100 %
512	512	128	128	30	0.24	$\langle\varepsilon\rangle$	-1.66e-07	1.98e-05	6.84e-06	-2.62e-07	-1.80e-06	-1.08e-05	-1.69e-07	-3.58e-07
						$\bar{\varepsilon}$	0.41 %	49.65 %	17.11 %	0.65 %	4.51 %	27.22 %	0.42 %	100 %
512	512	64	256	30	0.24	$\langle\varepsilon\rangle$	-1.66e-07	1.98e-05	9.65e-06	-2.69e-07	-1.76e-06	-1.08e-05	-1.69e-07	-3.54e-07
						$\bar{\varepsilon}$	0.38 %	46.45 %	22.56 %	0.63 %	4.11 %	25.44 %	0.39 %	100 %
512	512	64	128	20	0.24	$\langle\varepsilon\rangle$	-1.82e-07	1.98e-05	1.07e-05	-1.35e-07	-2.11e-06	-1.09e-05	-1.75e-07	-3.59e-07
						$\bar{\varepsilon}$	0.41%	44.92 %	24.42 %	0.30 %	4.79 %	24.73 %	0.39 %	100 %
512	512	64	128	30	0.0024	$\langle\varepsilon\rangle$	-1.28e-07	1.53e-05	1.72e-05	1.03e-06	-4.54e-06	-1.07e-05	-1.72e-07	-2.15e-07
						$\bar{\varepsilon}$	0.26 %	31.24 %	35.0 %	2.10 %	9.21 %	21.81 %	0.34 %	100%
512	512	64	128	30	0.24 all iter	$\langle\varepsilon\rangle$	-1.95e-07	2.06e-05	4.77e-06	-1.89e-07	-1.93e-06	-1.09e-05	-1.69e-07	-3.55e-07
						$\bar{\varepsilon}$	0.50 %	53.13 %	12.28 %	0.48 %	4.97 %	28.17 %	0.43 %	100 %

Table E.1: Summary table showing the volume average of the error on particle conservation for the scan on numerical parameters. The error is integrated in over a time interval between $3 \cdot 10^4 \Omega_i^{-1}$ and $4 \cdot 10^4 \Omega_i^{-1}$. The errors are defined as follows:

$$\langle \varepsilon_i \rangle = 1/V_i \int \big(\partial_t n_{GC} + \nabla \cdot \mathbf{\Gamma}\big) dt dV_i$$

where V_i is the volume of each region i and

$$\bar{\varepsilon} = \frac{\varepsilon_i}{\sum_i |\varepsilon_i|}$$

Appendix F

Adiabatic electron density in the SOL

The Poisson equation written in the form of quasineutrality equation can be written $n_i - n_{i0} = n_e - n_{e0}$ where $n_{i0} = n_{e0}$ are the initial ion and electron densities. We concentrate here on the expression for the electrons:

$$n_e = n_{e0} e^{e(\phi-\phi_0)/T_e} \approx n_{e0}\Big(1 + \frac{e(\phi-\phi_0)}{T_e}\Big) \tag{F.1}$$

where ϕ_0 is the electric potential of the plasma when $n_e = n_{e0}$. The electron density fluctuation δn_e is therefore:

$$\delta n_e = n_e - n_{e0} = n_{e0}\ \frac{e(\phi-\phi_0)}{T_e} \tag{F.2}$$

One then uses the constraint on the flux surface averages $< n_e >_{FS} = n_{e0}$ and therefore $< \delta n_e >_{FS} = 0$ which then yields $\phi_0 =< \phi >_{FS}$. In the Scrape-Off Layer one considers the same relation, namely:

$$\delta n_e = n_e - n_{e0} = n_{e0}\ \frac{e(\phi-\phi_0)}{T_e} \tag{F.3}$$

However, since the flux average surface does not hold, one requires that $\delta n_e = 0$ at the sheath entrance which then yields $\phi_0 = \phi_s = T_e\Lambda/e$. An alternative and equivalent approach is to consider the field line (fl) average:

$$\langle \delta n_e \rangle_{fl} = n_{e0}\ \frac{e(\langle\phi\rangle_{fl} - \phi_0)}{T_e} \tag{F.4}$$

then assuming that: $\langle \delta n_e \rangle_{fl} = 0$, one must have $\langle\phi\rangle_{fl} = \phi_0$. Finally, when assuming that $\phi \approx e\Lambda/T_e$, in other words that the sheath potential difference exceeds significantly any electric potential along the field line, one has:

$$\frac{e\phi_0}{T_e} = \Lambda \tag{F.5}$$

Therefore, in the SOL one can consider the approximation:

$$\delta n_e = n_{e0}\ \frac{e}{T_e}\ \Big(\phi - \frac{T_e\Lambda}{e}\Big) \tag{F.6}$$

Bibliography

[1] on Confin Transport I P E G, on Confin Database I P E G and Editors I P B 1999 *Nuclear Fusion* **39** 2175–2249 URL https://doi.org/10.1088%2F0029-5515%2F39%2F12%2F302

[2] Hinton F L and Hazeltine R D 1976 *Rev. Mod. Phys.* **48**(2) 239–308 URL https://link.aps.org/doi/10.1103/RevModPhys.48.239

[3] Wagner F and Stroth U 1993 *Plasma Physics and Controlled Fusion* **35** 1321–1371 URL https://doi.org/10.1088%2F0741-3335%2F35%2F10%2F002

[4] Bak P, Tang C and Wiesenfeld K 1988 *Phys. Rev. A* **38**(1) 364–374 URL https://link.aps.org/doi/10.1103/PhysRevA.38.364

[5] Turcotte D L 1999 *Reports on Progress in Physics* **62** 1377–1429 URL https://doi.org/10.1088%2F0034-4885%2F62%2F10%2F201

[6] Diamond P H, Itoh S I, Itoh K and Hahm T S 2005 *Plasma Physics and Controlled Fusion* **47** R35 URL http://stacks.iop.org/0741-3335/47/i=5/a=R01

[7] Ghendrih P, Ciraolo G, Larmande Y, Sarazin Y, Tamain P, Beyer P, Chiavassa G, Darmet G, Garbet X and Grandgirard V 2009 *Journal of Nuclear Materials - J NUCL MATER* **390** 425–427

[8] Dif-Pradalier G, Hornung G, Ghendrih P, Sarazin Y, Clairet F, Vermare L, Diamond P H, Abiteboul J, Cartier-Michaud T, Ehrlacher C, Estève D, Garbet X, Grandgirard V, Gürcan O D, Hennequin P, Kosuga Y, Latu G, Maget P, Morel P, Norscini C, Sabot R and Storelli A 2015 *Phys. Rev. Lett.* **114**(8) 085004 URL https://link.aps.org/doi/10.1103/PhysRevLett.114.085004

[9] Wolf R C 2002 *Plasma Physics and Controlled Fusion* **45** R1–R91 URL https://doi.org/10.1088%2F0741-3335%2F45%2F1%2F201

[10] Team A 1989 *Nuclear Fusion* **29** 1959 URL http://stacks.iop.org/0029-5515/29/i=11/a=010

[11] Luce T C, Petty C C and Cordey J G 2008 *Plasma Physics and Controlled Fusion* **50** 043001 URL https://doi.org/10.1088%2F0741-3335%2F50%2F4%2F043001

[12] Garbet X, Sarazin Y, Grandgirard V, Dif-Pradalier G, Darmet G, Ghendrih P, Angelino P, Bertrand P, Besse N, Gravier E, Morel P, Sonnendrücker E, Crouseilles N, Dischler J M, Latu G, Violard E, Brunetti M, Brunner S, Lapillonne X, Tran T M, Villard L and Boulet M 2007 *Nuclear Fusion* **47** 1206–1212 URL https://doi.org/10.1088%2F0029-5515%2F47%2F9%2F017

[13] Dif-Pradalier G, Diamond P, Grandgirard V, Sarazin Y, Abiteboul J, Garbet X, Ghendrih P, Strugarek A, Ku S H and Chang C 2010 *Physical review. E, Statistical, nonlinear, and soft matter physics* **82** 025401

[14] Ida K, Shi Z, Sun H, Inagaki S, Kamiya K, Rice J, Tamura N, Diamond P, Dif-Pradalier G, Zou X, Itoh K, Sugita S, Gürcan O, Estrada T, Hidalgo C, Hahm T, Field A, Ding X, Sakamoto Y, Oldenbürger S, Yoshinuma M, Kobayashi T, Jiang M, Hahn S, Jeon Y, Hong S, Kosuga Y, Dong J and Itoh S I 2015 *Nuclear Fusion* **55** 013022 URL https://doi.org/10.1088%2F0029-5515%2F55%2F1%2F013022

[15] Idomura Y, Urano H, Aiba N and Tokuda S 2009 *Nuclear Fusion* **49** 065029 URL http://stacks.iop.org/0029-5515/49/i=6/a=065029

[16] Heikkinen J A, Henriksson S, Janhunen S, Kiviniemi T P and Ogando F 2006 *Contributions to Plasma Physics* **46** 490–495 (*Preprint* https://onlinelibrary.wiley.com/doi/pdf/10.1002/ctpp.200610035) URL https://onlinelibrary.wiley.com/doi/abs/10.1002/ctpp.200610035

[17] Jolliet S, Bottino A, Angelino P, Hatzky R, Tran T, Mcmillan B, Sauter O, Appert K, Idomura Y and Villard L 2007 *Computer Physics Communications* **177** 409 – 425 ISSN 0010-4655 URL http://www.sciencedirect.com/science/article/pii/S0010465507002251

[18] Chang C S, Ku S, Diamond P H, Lin Z, Parker S, Hahm T S and Samatova N 2009 *Physics of Plasmas* **16** 056108 (*Preprint* https://doi.org/10.1063/1.3099329) URL https://doi.org/10.1063/1.3099329

[19] Garbet X, Idomura Y, Villard L and Watanabe T 2010 *Nuclear Fusion* **50** 043002

[20] Frank-Kamenetskii D A 1972 *Plasma: the fourth state of matter* (Springer)

[21] Brizard A J 2004 *Physics of Plasmas* **11** 4429–4438

[22] Rozar, Fabien, Steiner, Christophe, Latu, Guillaume, Mehrenberger, Michel, Grandgirard, Virginie, Bigot, Julien, Cartier-Michaud, Thomas and Roman, Jean 2016 *ESAIM: Proc.* **53** 191–210 URL https://doi.org/10.1051/proc/201653012

[23] Grandgirard V, Sarazin Y, Angelino P, Bottino A, Crouseilles N, Darmet G, Dif-Pradalier G, Garbet X, Ghendrih P, Jolliet S, Latu G, Sonnendrücker E and Villard L 2007 *Plasma Physics and Controlled Fusion* **49** B173–B182 URL https://doi.org/10.1088%2F0741-3335%2F49%2F12b%2Fs16

[24] Abiteboul J 2012 *Turbulent and neoclassical toroidal momentum transport in tokamak plasmas* Ph.D. thesis Aix-Marseille Université

[25] Donnel P and et al 2018 *Submitted to Computer Physics Communications*

[26] Dif-Pradalier G, Grandgirard V, Sarazin Y, Garbet X and Ghendrih P 2009 *Phys. Rev. Lett.* **103**(6) 065002 URL https://link.aps.org/doi/10.1103/PhysRevLett.103.065002

[27] Estève D, Sarazin Y, Garbet X, Grandgirard V, Breton S, Donnel P, Asahi Y, Bourdelle C, Dif-Pradalier G, Ehrlacher C, Emeriau C, Ghendrih P, Gillot C, Latu G and Passeron C 2017 *Nuclear Fusion* URL http://iopscience.iop.org/10.1088/1741-4326/aa6ebb

[28] Lin Z, Hahm T S, Lee W W, Tang W M and Diamond P H 1999 *Phys. Rev. Lett.* **83**(18) 3645–3648 URL https://link.aps.org/doi/10.1103/PhysRevLett.83.3645

[29] Vernay T, Brunner S, Villard L, McMillan B F, Jolliet S, Tran T M and Bottino A 2012 *Physics of Plasmas* **19** 042301 (*Preprint* https://doi.org/10.1063/1.3699189) URL https://doi.org/10.1063/1.3699189

[30] Romanelli F and Zonca F 1993 *Physics of Fluids B: Plasma Physics* **5** 4081–4089 (*Preprint* https://doi.org/10.1063/1.860576) URL https://doi.org/10.1063/1.860576

[31] Jenko F, Dorland W, Kotschenreuther M and Rogers B N 2000 *Physics of Plasmas* **7** 1904–1910 (*Preprint* https://doi.org/10.1063/1.874014) URL https://doi.org/10.1063/1.874014

[32] Sarazin Y, Grandgirard V, Abiteboul J, Allfrey S, Garbet X, Ghendrih P, Latu G, Strugarek A and Dif-Pradalier G 2010 *Nuclear Fusion* **50** 054004 URL https://doi.org/10.1088%2F0029-5515%2F50%2F5%2F054004

[33] Sarazin Y, Grandgirard V, Dif-Pradalier G, Fleurence E, Garbet X, Ghendrih P, Bertrand P, Besse N, Crouseilles N, Sonnendrücker E, Latu G and Violard E 2006 *Plasma Physics and Controlled Fusion* **48** B179–B188 URL https://doi.org/10.1088%2F0741-3335%2F48%2F12b%2Fs17

[34] Idomura Y, Tokuda S and Kishimoto Y 2003 *Nuclear Fusion* **43** 234–243 URL https://doi.org/10.1088%2F0029-5515%2F43%2F4%2F303

[35] Angelino P, Bottino A, Hatzky R, Jolliet S, Sauter O, Tran T M and Villard L 2006 *Physics of Plasmas* **13** 052304 (*Preprint* https://doi.org/10.1063/1.2193947) URL https://doi.org/10.1063/1.2193947

[36] Dif-Pradalier G, Grandgirard V, Sarazin Y, Garbet X and Ghendrih P 2008 *Communications in Nonlinear Science and Numerical Simulation* **13** 65–71

[37] Winsor N, Johnson J L and Dawson J M 1968 *The Physics of Fluids* **11** 2448–2450 (*Preprint* https://aip.scitation.org/doi/pdf/10.1063/1.1691835) URL https://aip.scitation.org/doi/abs/10.1063/1.1691835

[38] Dif-Pradalier G, Grandgirard P, Sarazin P, Garbet P, Ghendrih P and Angelino P 2008 *Physics of Plasmas* **15** 42315 – 42315 URL https://hal-cea.archives-ouvertes.fr/cea-01468363

[39] Grandgirard V and et al 2016 *Computer Physics Communications* **207** 35 – 68 ISSN 0010-4655

[40] Sips A, Schweinzer J, Luce T, Wolfe S, Urano H, Hobirk J, Ide S, Joffrin E, Kessel C, Kim S, Lomas P, Nunes I, Pütterich T, Rimini F, Solomon W, Stober J, Turco F, de Vries P, , , , and and 2018 *Nuclear Fusion* **58** 126010 URL https://doi.org/10.1088%2F1741-4326%2Faade57

[41] Connor J W 1988 *Plasma Physics and Controlled Fusion* **30** 619–650 URL https://doi.org/10.1088%2F0741-3335%2F30%2F6%2F001

[42] Buckingham E 1914 *Phys. Rev.* **4**(4) 345–376 URL https://link.aps.org/doi/10.1103/PhysRev.4.345

[43] Petty C C, Luce T C, McDonald D C, Mandrekas J, Wade M R, Candy J, Cordey J G, Drozdov V, Evans T E, Ferron J R, Groebner R J, Hyatt A W, Jackson G L, La Haye R J, Osborne T H and Waltz R E 2004 *Physics of Plasmas* **11** 2514–2522 (*Preprint* https://doi.org/10.1063/1.1666263) URL https://doi.org/10.1063/1.1666263

[44] Garbet X, Mantica P, Angioni C, Asp E, Baranov Y, Bourdelle C, Budny R, Crisanti F, Cordey G, Garzotti L, Kirneva N, Hogeweij D, Hoang T, Imbeaux F, Joffrin E, Litaudon X, Manini A, McDonald D C, Nordman H, Parail V, Peeters A, Ryter F, Sozzi C, Valovic M, Tala T, Thyagaraja A, Voitsekhovitch I, Weiland J, Weisen H, Zabolotsky A and the JET EFDA Contributors 2004 *Plasma Physics and Controlled Fusion* **46** B557–B574 URL https://doi.org/10.1088%2F0741-3335%2F46%2F12b%2F045

[45] Lin Z, Ethier S, S Hahm T and M Tang W 2002 *Physical review letters* **88** 195004

[46] McMillan B F, Lapillonne X, Brunner S, Villard L, Jolliet S, Bottino A, Görler T and Jenko F 2010 *Phys. Rev. Lett.* **105**(15) 155001 URL https://link.aps.org/doi/10.1103/PhysRevLett.105.155001

[47] Sarazin Y, Grandgirard V, Abiteboul J, Allfrey S, Garbet X, Ghendrih P, Latu G, Strugarek A, Dif-Pradalier G, Diamond P, Ku S, Chang C, McMillan B, Tran T, Villard L, Jolliet S, Bottino A and Angelino P 2011 *Nuclear Fusion* **51** 103023 URL https://doi.org/10.1088%2F0029-5515%2F51%2F10%2F103023

[48] Dorland W, Jenko F, Kotschenreuther M and Rogers B N 2000 *Phys. Rev. Lett.* **85**(26) 5579–5582 URL https://link.aps.org/doi/10.1103/PhysRevLett.85.5579

[49] Mittal R and Iaccarino G 2005 *Annu. Rev. Fluid Mech.* **37** 239–261

[50] Isoardi L and et al 2010 *Journal of Computational Physics* **229** 2220–2235

[51] Serre E and Bufferand e a *Contributions to Plasma Physics* **52** 401–405

[52] Paredes A, Bufferand H and et al 2014 *Journal of Computational Physics* **274** 283–298

[53] Gunn J and et al 2007 *Journal of Nuclear Materials* **363-365** 484 – 490 ISSN 0022-3115 plasma-Surface Interactions-17

[54] Abiteboul J, Ghendrih P, Grandgirard V, Cartier-Michaud T, Dif-Pradalier G, Garbet X, Latu G, Passeron C, Sarazin Y, Strugarek A, Thomine O and Zarzoso D 2013 *Plasma Physics and Controlled Fusion* **55** 074001

[55] Ghendrih P, Bodi K, Bufferand H, Chiavassa G, Ciraolo G, Fedorczak N, Isoardi L, Paredes A, Sarazin Y, Serre E, Schwander F and Tamain P 2011 *Plasma Physics and Controlled Fusion* **53** 054019 URL https://doi.org/10.1088%2F0741-3335%2F53%2F5%2F054019

[56] Schirmer J, Conway G, Zohm H, Suttrop W and the ASDEX Upgrade Team 2006 *Nuclear Fusion* **46** S780–S791 URL https://doi.org/10.1088%2F0029-5515%2F46%2F9%2Fs13

[57] Trier E, Hennequin P, Fenzi C, Gürcan, Sabot R, Maget P, Bucalossi J, Garbet X, Clairet F, Vermare L, Bourdelle C, Guimarães-Filho Z, Falchetto G and Huijsmans G 2009 **33**

[58] Trier E, Hennequin P, Gürcan D, Sabot R, Bucalossi J, Guimarães-Filho Z, Bourdelle C, Clairet F, Falchetto G, Fenzi C, Garbet X, Maget P and and L V 2017 *Nuclear Fusion* **57** 046021 URL https://doi.org/10.1088%2F1741-4326%2Faa59bb

[59] Norscini C 2015 *Self-organized turbulent transport in fusion plasmas* Theses Université d'Aix Marseille URL https://tel.archives-ouvertes.fr/tel-01296283

[60] Rogers B N, Dorland W and Kotschenreuther M 2000 *Phys. Rev. Lett.* **85**(25) 5336–5339 URL https://link.aps.org/doi/10.1103/PhysRevLett.85.5336

[61] Idomura Y, Wakatani M and Tokuda S 2000 *Physics of Plasmas* **7** 3551–3566 (*Preprint* https://doi.org/10.1063/1.1287418) URL https://doi.org/10.1063/1.1287418

[62] Garbet X, Fenzi C, Capes H, Devynck P and Antar G 1999 *Physics of Plasmas* **6** 3955–3965 (*Preprint* https://doi.org/10.1063/1.873659) URL https://doi.org/10.1063/1.873659

[63] D'Angelo N 1965 *The Physics of Fluids* **8** 1748–1750 (*Preprint* https://aip.scitation.org/doi/pdf/10.1063/1.1761496) URL https://aip.scitation.org/doi/abs/10.1063/1.1761496

[64] Catto P J, Rosenbluth M N and Liu C S 1973 *The Physics of Fluids* **16** 1719–1729 (*Preprint* https://aip.scitation.org/doi/pdf/10.1063/1.1694200) URL https://aip.scitation.org/doi/abs/10.1063/1.1694200

[65] Luo Q Z, D'Angelo N and Merlino R L 2001 *Physics of Plasmas* **8** 31–35 (*Preprint* https://doi.org/10.1063/1.1323755) URL https://doi.org/10.1063/1.1323755

[66] Guillard H, Bilanceri M, Colin C, Ghendrih P, Giorgiani G, Nkonga B, Schwander F, Serre E and Tamain P 2014 *Journal of Physics: Conference Series* **561** 012009 URL https://hal.inria.fr/hal-01100365

[67] Newton S L, Cowley S C and Loureiro N F 2010 *Plasma Physics and Controlled Fusion* **52** 125001 URL https://doi.org/10.1088%2F0741-3335%2F52%2F12%2F125001

[68] Sarazin Y and Ghendrih P 1998 *Physics of Plasmas* **5** 4214–4228 (*Preprint* https://doi.org/10.1063/1.873157) URL https://doi.org/10.1063/1.873157

[69] Goldston R 2011 *Nuclear Fusion* **52** 013009 URL https://doi.org/10.1088%2F0029-5515%2F52%2F1%2F013009

[70] Liewer P C 1985 *Nuclear Fusion* **25** 543–621 URL https://doi.org/10.1088%2F0029-5515%2F25%2F5%2F004

[71] Bourdelle C, Gerbaud T, Vermare L, Casati A, Aniel T, Artaud J, Basiuk V, Bucalossi J, Clairet F, Corre Y, Devynck P, Falchetto G, Fenzi C, Garbet X, Guirlet R, Gürcan, Heuraux S, Hennequin P, Hoang G, Imbeaux F, Manenc L, Monier-Garbet P, Moreau P, Sabot R, Ségui J L, Sirinelli A and and D V 2011 *Nuclear Fusion* **51** 063037 URL https://doi.org/10.1088%2F0029-5515%2F51%2F6%2F063037

[72] Holland C, Schmitz L, Rhodes T L, Peebles W A, Hillesheim J C, Wang G, Zeng L, Doyle E J, Smith S P, Prater R, Burrell K H, Candy J, Waltz R E, Kinsey J E, Staebler G M, DeBoo J C, Petty C C, McKee G R, Yan Z and White A E 2011 *Physics of Plasmas* **18** 056113 (*Preprint* https://doi.org/10.1063/1.3574518) URL https://doi.org/10.1063/1.3574518

[73] Candy J and Waltz R 2003 *Journal of Computational Physics* **186** 545 – 581 ISSN 0021-9991 URL http://www.sciencedirect.com/science/article/pii/S0021999103000792

[74] Casati A, Gerbaud T, Hennequin P, Bourdelle C, Candy J, Clairet F, Garbet X, Grandgirard V, Gürcan O D, Heuraux S, Hoang G T, Honoré C, Imbeaux F, Sabot R, Sarazin Y, Vermare L and Waltz R E 2009 *Phys. Rev. Lett.* **102**(16) 165005 URL https://link.aps.org/doi/10.1103/PhysRevLett.102.165005

[75] Candy J and Waltz R E 2003 *Phys. Rev. Lett.* **91**(4) 045001 URL https://link.aps.org/doi/10.1103/PhysRevLett.91.045001

[76] Holland C, Petty C, Schmitz L, Burrell K, McKee G, Rhodes T and Candy J 2012 *Nuclear Fusion* **52** 114007 URL https://doi.org/10.1088%2F0029-5515%2F52%2F11%2F114007

[77] Görler T, White A E, Told D, Jenko F, Holland C and Rhodes T L 2014 *Physics of Plasmas* **21** 122307 (*Preprint* https://doi.org/10.1063/1.4904301) URL https://doi.org/10.1063/1.4904301

[78] Neiser T F, Jenko F, Carter T A, Schmitz L, Told D, Merlo G, Banon Navarro A, Crandall P C, McKee G R and Yan Z 2019 *Physics of Plasmas* **26** 092510 (*Preprint* https://doi.org/10.1063/1.5052047) URL https://doi.org/10.1063/1.5052047

[79] Dif-Pradalier G, Caschera E, Ghendrih P, Asahi Y, Donnel P, Garbet X, Grandgirard V, Latu G, Norscini C and Sarazin Y 2017 *Plasma and Fusion Research* **12** 1203012

[80] Gerbaud T 2008 *Étude de la microturbulence par réflectométrie dans un plasma de fusion sur le tokamak Tore-Supra* Ph.D. thesis Université Henri Poincaré, Nancy-I

[81] Hahm T S, Diamond P H, Lin Z, Itoh K and Itoh S I 2004 *Plasma Physics and Controlled Fusion* **46** A323–A333 URL https://doi.org/10.1088%2F0741-3335%2F46%2F5a%2F036

[82] Mattor N and Diamond P H 1994 *Phys. Rev. Lett.* **72**(4) 486–489

[83] Garbet X, Laurent L, Samain A and Chinardet J 1994 *Nuclear Fusion* **34** 963

[84] Kadomtsev B B 1992 *Plasma Physics and Controlled Fusion* **34** 1931–1938 URL https://doi.org/10.1088%2F0741-3335%2F34%2F13%2F023

[85] Press W H, Flannery B P, Teukolsky S A and Vetterling W T 1988 *Numerical recipes in C: the art of scientific computing* (Cambridge University Press New York, NY, USA)